SISSA **ISAS**

SCUOLA INTERNAZIONALE SUPERIORE DI STUDI AVANZATI
INTERNATIONAL SCHOOL FOR ADVANCED STUDIES

Enlightening dark energy with the CMB three point correlation function

Thesis submitted for the degree of
Doctor Philosophiæ

CANDIDATE:
Fabio Giovi

SUPERVISOR:
Dott. Carlo Baccigalupi

October 2005

Table of Contents

Citations to Previously Published Works

The work presented in this thesis has been partially published in scientific papers.

Published on referred journals:

– *"Cosmic microwave background constraints on dark energy dynamics: analysis beyond the power spectrum"*.
Giovi F., Baccigalupi C. & Perrotta F., Phys. Rev. D **71**, 103009 (2005).

– *"Constraining the dark energy dynamics with the cosmic microwave background bispectrum"*.
Giovi F., Baccigalupi C. & Perrotta F., Phys. Rev. D **68**, 123002 (2003).

Proceedings:

– *"Dark energy and CMB bispectrum"*.
Giovi F. & Baccigalupi C., "Impact of Gravitational Lensing on Cosmology", Mellier Y. & Meylan G. Eds., proceedings of the IAU Symposium N. 225, Lausanne 19-23 july 2004.

– *"Weak lensing, structure formation and dark energy"*.
Giovi F., Baccigalupi C. & Perrotta F., "Where Cosmology and Fundamental Physics meet", Le Brun V., Basa S. & Mazure A. Eds., proceedings of the IV Marseille Cosmology Conference, Marseille 23-26 june 2003.

Acknowledgments

This thesis is the end point of my PhD. I spent 4 years in Trieste with some good and some bad times. I had the opportunity to learn more in the field of cosmology. I met a lot of people and, in some sense, I "regressed" to the time of the school, indeed the SISSA *is* a school...Here I can write something more than the research I've done and I want to fill this small space to thank some people that helped me in this small scientific adventure. First I would like to thank Carlo Baccigalupi that supervised my work during the 4 years at SISSA. He helped me not only from a scientific point of view but he had also the patience to correct my (very bad) english while writing papers and, expecially, this thesis. I had many discussions with Francesca Perrotta. She was able to lay some physical questions I never thought, making my work more complete. A very special thank goes to Pier Stefano Corasaniti: one of the smartest guys in the world of cosmology. I know that he's always ready to help me even if there is a sea or even an ocean to separate us. Our friendship has been cementified during our "canonical" holidays in Rome (Christmas, Easter and in the summer). Inside and outside SISSA I shared a lot of time and a lot of fun with Sara Tinti and Francesca Annibali: their support during the classes of the first year was incommensurable. Whenever I had a problem, not only scientific, their office were always open and they were always ready to help me. For two years I shared the office and the desk with Viviana Acquaviva, with her I had a lot of fun, but also a lot of scientific support. Even though my family was 700 km far, they were always with me. My mother and my father were and are always present to help me, while my sister updated me about all the things that happened in Rome and in my family. A few words and a warm thought to Filippo (without forgetting Isotta). I would like to thank the old friends that never forgot me even if I was far from Rome: Sveva, Chiara and Massimo. Here there is a list of the people that in some way helped me or simply became my new friends: Lorenzo (★) Stella, Roberto Ricci, Ruben Salvaterra, Bruno Giacomazzo, Lucattilio Tenuta, Valentina Riva, Simone Pigolotti, Željka Bošnjak, Claudio (W.) Attaccalite, Michele Casula, Sara Bertocco, Michela Mapelli, Emanuele Ripamonti, Pasquale Panuzzo, Sandro Fogliani and Lucia Ballo.

Finally the greatest help was given to me by Simona. She supported and stood with me during the whole PhD and in writing this thesis. She left Rome to join me in Trieste, and that was not so easy; now we go back in Rome together.

Chapter 1

Introduction

One of the greatest discoveries in modern cosmologies is the apparent *accelerating* cosmic expansion. In terms of "canonical" physics, i.e. in the framework of a general relativistic description of cosmology itself, the latter may be interpreted as the effect of a non-null energy density in the vacuum, the Cosmological Constant. The discrepancy of the observed amount of this new entity with respect to any known scale in particle physics, reaching 120 orders of magnitudes if compared with the Planck scale, led the community to look for different solutions, generalizing the concept of vacuum energy in cosmology to the plethora of models, ideas and speculations forming nowadays the class of dark energy cosmologies. Differently from the Cosmological Constant, almost all of those involve some spacetime dynamics in the substance inducing cosmic acceleration. One of the greatest challenges in the modern *observational* cosmology is to isolate the fingerprint of one of those scenarios, if any, in order to confirm or reject the existence of a Cosmological Constant in our Universe. The study concerns the whole epoch in which the acceleration is active, about half of the life of the Universe in ordinary time; in particular, since the existing data already indicate that the dark energy today is close (10% precision) to a Cosmological Constant, it is important to design tools which are able to probe the dark energy behavior at earlier epochs than the present. This work represents an effort in this direction.

We focus on the gravitational lensing induced by forming cosmological structures on the background light, represented by the anisotropies in the temperature of the Cosmic

Microwave Background (CMB) radiation. The reason is simple and purely geometric, being one of the very basic laws of gravitational lensing: for any given source position, the gravitational lensing deflection is zero if the lens position coincides with the observer or the source itself. The lensing deflection, therefore, keeps some record of the cosmic behavior at intermediate epochs *only*.

The lensing impacts CMB anisotropies in several ways. They are powered by primordial perturbations, now accurately probed by the existing measurements; it is crucial to isolate CMB observables which are unbiased by such primordial power, in order to be most sensitive to the lensing contribution, containing the relevant information for our purposes. One of them is the non-Gaussian distortion induced by lensing deflection on the primordial anisotropies. That may be parameterized in several ways. We choose here its harmonic description, by means of the three-point CMB anisotropy correlation function expressed in the spherical harmonics domain, the so called CMB bispectrum. We shall show that, although challenging in its detection, the CMB bispectrum actually shows promising features in the sensitivity to the cosmic expansion, the dark energy properties in other words, at the onset of acceleration, providing important complementary information with respect to other, "canonical" observables such as the two-point correlation function in terms of the power spectrum of anisotropies.

In order to achieve our goal, we need several pieces of the theoretical framework of modern cosmology. We need the full theory of CMB anisotropies, and of how growing cosmological structures affect those by means of gravitational lensing. We need a solid description of the dark energy, general and not too specific in order to give as much generality to our results as we can. Moreover, even before facing our main problem, we need a general study of the phenomenology of the three-point CMB statistics, from a geometrical and phenomenological point of view, in order to better comprehend our results, and isolate the signal differences induced by the different underlying dark energy models. Finally, with all these means, we may face our problem, quantifying the benefit that the CMB bispectrum knowledge yield on the overall CMB capability to constrain the underlying physical reason for cosmic acceleration. Here below we give a more detailed and technical description of the contents of this thesis.

In Ch. 2 we give a review of the concordance cosmology listing and briefly discussing the most important evidences for cosmic acceleration. We discuss the Cosmological Constant as a candidate for explaining the acceleration showing its main weaknesses and its main theoretical problems. We introduce the dark energy as a generalized form of vacuum energy, solving some of the classical problems affecting the Cosmological Constant. We conclude the chapter focusing on the cosmological weak lensing effect as a tool to study the dark energy.

In Ch. 3, after a little historical digression about the discovery of the CMB radiation and its anisotropies, we review the linear perturbation and CMB anisotropy theory. A phenomenological description of CMB anisotropies and the discussion of the lensing effect on the CMB power spectrum concludes the chapter.

In Ch. 4 we write the basic formalism describing the CMB bispectrum induced by the correlation between lensing and growth of cosmological structures; we also show why the bispectrum can be useful to study the nature of the dark energy dynamics. Then we make a little "computational" digression describing the method we implemented to evaluate the Wigner 3J symbols, a necessary but computationally challenging ingredient to evaluate the bispectrum. Finally we study the geometrical properties of the bispectrum in full generality exploring a three-dimensional multipole space.

Ch. 5 is devoted to the dark energy theory, focusing on models involving a scalar field, the Quintessence. We discuss the background dynamics for exact models adopting a phenomenological approach to the dark energy equation of state, i.e. the ratio between its pressure and energy density, which needs to be negative and close to -1 in order to imprint cosmic acceleration. In the last section of this chapter we show how the present value of the equation of state influences the CMB power spectrum and large scale structure; we conclude the chapter with the current constrains on the dark energy equation of state.

In Ch. 6 we discuss the angular diameter distance degeneracy that affect the CMB power spectrum, which makes hard the study of the dark energy on the basis of that observable. Then we show how the bispectrum breaks this degeneracy, adding information on the dark energy dynamics just where the power spectrum fails. We compute the signal to noise ratio for the bispectrum showing that it is detectable only if we take into account all

the possible geometrical configurations. We make a likelihood analysis on a three parameters space where we vary the dark energy abundance, the present and the asymptotic value of its equation of state. Finally we show how, when and where the bispectrum analysis improves that of the power spectrum only, narrowing the confidence levels in the likelihood analysis and breaking the degeneracies.

In Ch. 7 we briefly discuss the main contaminants and systematics that can pollute the CMB data making the detection of the bispectrum hard. Finally we summarize the work done in this thesis, pointing to new directions to extend what we have done until now, and putting our concluding remarks.

Chapter 2

The current cosmic picture

In the last few years our understanding of the Universe has improved considerably thanks to the progress of several observables such as the supernovae type Ia (SNIa, Riess *et al.* 1998; Perlmutter *et al.* 1999), the Cosmic Microwave Background (CMB) radiation (de Bernardis *et al.* 2000; Spergel *et al.* 2003) and the Large Scale Structure (LSS; Percival *et al.* 2001; Dodelson *et al.* 2002). Those cosmological observations indicate that the Universe is nearly geometrically flat, filled with structures which grew out of a primordial linear spectrum of nearly Gaussian and scale invariant perturbations and that its expansion is accelerated. About 4% of the critical energy density is made of baryons, while the remaining dark part is supposed to interact most weakly with the baryons themselves, since we observe it only through its gravitational effects. The dark component appears to be 30% pressureless, such as in cold dark matter (CDM) scenarios, dominating the gravitational potential perturbations which host visible structures such as galaxies or clusters. The remaining 70% should be in some sort of vacuum energy, with a negative pressure acting as a repulsive gravity, and responsible for a late time cosmic acceleration era. In this chapter we want to review briefly the evidences and the motivations that led the inclusion of this component into the cosmic budget and the challenge that it represents for the whole picture. The chapter is structured as follows: in Sec. 2.1 we review the Friedmann-Robertson-Walker (FRW) cosmology; in Sec. 2.2 we report the observational evidences in favor of the cosmic acceleration; in Sec. 2.3 we discuss the Cosmological Constant and the related problems;

in Sec. 2.4 we introduce the dark energy cosmology; finally in Sec. 2.5 we discuss the most important observables capable to constrain the dark energy dynamics, i.e. confirming or ruling out the Cosmological Constant.

2.1 Standard cosmology

The Einstein field equations rule the general relativistic cosmology; they are

$$G_{\mu\nu} \equiv R_{\mu\nu} - \frac{1}{2} g_{\mu\nu} R = 8\pi G T_{\mu\nu} + g_{\mu\nu}\Lambda \ , \tag{2.1}$$

where $G_{\mu\nu}$ is the Einstein tensor, $R_{\mu\nu}$ is the Ricci tensor, R is the Ricci scalar, G is the gravitational constant $T_{\mu\nu}$ is the stress-energy tensor and Λ is the Cosmological Constant term. We use natural units for the speed of light and the Planck constant. Eq. (2.1) relates the geometry of the spacetime (left hand side) with the energy sources (right hand side); the dynamics of the metric is determined by the stress-energy tensor, including the contribution from non-relativistic matter and radiation; the large scale geometry is described by the FRW metric which, in spherical coordinates (r, θ, ϕ), is

$$ds^2 = -dt^2 + a^2(t) \left[\frac{dr^2}{1 - Kr^2} + r^2 \left(d\theta^2 + \sin^2\theta d\phi^2 \right) \right] \ , \tag{2.2}$$

where $a(t)$ is the scale factor and K can take the values -1, 0 and $+1$ defining an open, flat and closed geometry respectively. Since we assumed spatial homogeneity and isotropy, the form of the stress-energy tensor for the i^{th} perfect fluid component is diagonal and is given by

$$T^{\nu}_{\mu(i)} = \mathrm{diag}\left(-\rho_i, p_i, p_i, p_i\right) \ , \tag{2.3}$$

being ρ_i the energy density and p_i the pressure; both pressure and energy density are generally dynamical quantities. In the following, we indicate such dependence both as a function of time and the scale factor a.

In the FRW metric the Einstein field equations with a perfect relativistic fluid become the Friedmann equations

$$H^2 \equiv \left(\frac{\dot{a}}{a} \right)^2 = \frac{8\pi G}{3} \sum_i \rho_i(a) + \frac{\Lambda}{3} - \frac{K}{a^2} \ , \tag{2.4}$$

$$\frac{\ddot{a}}{a} = -\frac{4\pi G}{3} \sum_i \left[\rho_i(a) + 3p_i(a) \right] + \frac{\Lambda}{3} \ . \tag{2.5}$$

where the overdot means time derivative and H is the Hubble parameter. Defining the critical density $\rho_c = 3H_0^2/(8\pi G) \simeq 1.88h^2 \times 10^{-29}\mathrm{g/cm}^3$ (H_0 is the Hubble's constant, i.e. the value of the Hubble parameter today, while h is its value in units of 100 km/s/Mpc) we can parameterize the density parameters of the i^{th} fluid component, the Cosmological Constant Λ and the curvature as

$$\Omega_i(a) = \frac{\rho_i(a)}{\rho_c} \ , \ \Omega_\Lambda = \frac{\Lambda}{8\pi G\rho_c} \ , \ \Omega_K(a) = -\frac{K}{a^2H^2} \ , \tag{2.6}$$

respectively. Indeed it is sometimes useful to think the Cosmological Constant and the spatial curvature as cosmological components, with $\rho_\Lambda = \Lambda/(8\pi G)$ and $\rho_K(a) = -3K/\left(8\pi G a^2\right)$ respectively; ρ_K is not an energy density but a simple way to keep track of how much energy density is missing or in excess in comparison to a flat universe. If we rewrite the Friedmann equation (2.4) as

$$\Omega_{tot}(a) = \sum_i \Omega_i(a) + \Omega_\Lambda = 1 - \Omega_K(a) \ , \tag{2.7}$$

we see that the spatial curvature is fixed by the total energy content.

The energy conservation in general relativity is expressed by the fact that the stress-energy tensor is divergenceless, i.e. $T^{\mu\nu}_{(i);\nu} = 0$; the latter relation is not satisfied for interacting components. In a FRW metric with perfect fluids, the divergenceless condition yields to the equation for the evolution of the single fluid component:

$$\dot{\rho}_i(t) = -3H[\rho_i(t) + p_i(t)] \ . \tag{2.8}$$

To be solved, this equation needs the introduction of the equation of state linking pressure and energy density. In most cases they are related by

$$p_i = w_i\rho_i \ . \tag{2.9}$$

For each fluid the actual value of w_i is directly related to the physical properties of that particular component. Substituting the general equation of state (2.9) into the energy conservation equation (2.8) we get the time evolution of the energy density

$$\rho_i(a) \propto a^{-3(1+w_i)} \ , \tag{2.10}$$

	w	$\rho(a)$	$a(t)$
Non-relativistic matter (dust)	0	a^{-3}	$t^{2/3}$
Relativistic matter and radiation	1/3	a^{-4}	$t^{1/2}$
Cosmological Constant	-1	constant	e^{Ht}
Curvature	$-1/3$	a^{-2}	t

Table 2.1: Summary of the values of the equation of state of the most important sources of energy density in cosmology, together with the time dependence of the scale factor if they dominate the expansion.

where we assumed that w_i is not varying in time. Assuming a flat space ($K = 0$) we see how the scale factor evolves with time:

$$a(t) \propto \begin{cases} t^{\frac{2}{3(1+w_i)}} & w \neq -1 \\ e^{Ht} & w = -1 \end{cases} . \tag{2.11}$$

In Tab. 2.1 we show the values of the equation of state and the behaviors of energy density and scale factor for the main cosmological components; the latter behavior refers to the case in which the corresponding component dominates the expansion. While the energy densities of radiation and dust decrease with time, the Cosmological Constant energy density remains constant, allowing to dominate the expansion eventually.

The effect of the Cosmological Constant on the expansion rate of the Universe can be seen from Eq. (2.5); the value of the deceleration parameter today, neglecting the radiation, is

$$q_0 \equiv -\frac{1}{H_0^2}\left(\frac{\ddot{a}}{a}\right)_0 = \frac{\Omega_m}{2} - \Omega_\Lambda \ . \tag{2.12}$$

The previous equation tell us that for $\Omega_\Lambda > \Omega_m/2$ the expansion of the Universe is accelerated since $q_0 < 0$.

We stress that the cosmic dynamics at a given epoch, the present for example, is mainly determined by the geometrical quantities H_0 (the Hubble parameter) and q_0 (the deceleration parameter); the former give us a measure of the velocity of the expansion while the latter probes the acceleration of the expansion.

2.2 Evidences for cosmic acceleration

One of the most challenging problems in modern cosmology is to provide an explanation for the recently observed accelerated expansion of the Universe. The first direct evidence for this came from studies using Supernovæ Type Ia (SNIa) as standard candles to measure the distance-redshift relation in the Universe (Riess *et al.* 1998; Perlmutter *et al.* 1999).

The SNIa possess a nearly uniform intrinsic luminosity with an absolute magnitude $M \sim -19.5$ that is typically comparable to the brightness of the entire host galaxy in which they appear. Since they have such high luminosity, they can be detected at high redshift (the most distant SNIa detected is SN1997ff at redshift $z \simeq 1.7$), allowing in principle a good handle on cosmological effects. The fact that all SNIa have similar intrinsic luminosities fits well with our understanding of these events as explosions which occur when a carbon-oxygen white dwarf approaches the Chandrasekhar limit and explodes with a thermonuclear deflagration. The Chandrasekhar limit is approached because the white dwarf is gradually accreting from a companion star; this limit is almost a universal quantity, so the resulting explosions possess similar luminosities (see Hillebrandt & Niemeyer 2000 for reviews). The correlation between the peak luminosity of a SNIa and its decline rate makes it possible to estimate the magnitude, whereas with spectral measures of the host galaxy one can determine its redshift. Dimmer SNIa decline more rapidly after maximum brightness while brighter SNIa decline more slowly; such correlation can be quantified by the drop in magnitude 15 days after the peak luminosity is reached.

A standard candle is used to determine cosmological distances and must satisfy three conditions: it needs to be bright, homogeneous and present everywhere in space. SNIa fulfill all these requirements, possessing a magnitude-redshift relation given by

$$m(z) - M = 5 \log d_{\mathcal{L}}(z) + 25 \ , \tag{2.13}$$

where $m(z)$ is the apparent bolometric magnitude, M is the absolute magnitude and $d_{\mathcal{L}}(z)$ is the luminosity distance in units of Mpc. Furthermore, the luminosity distance depends on the geometry of the space and its energy content, being defined by $d^2_{\mathcal{L}} = \mathcal{L}/(4\pi\mathcal{F})$, where $\mathcal{F}$ is the measured flux and $\mathcal{L}$ is the absolute luminosity of the object. We can express $d_{\mathcal{L}}$

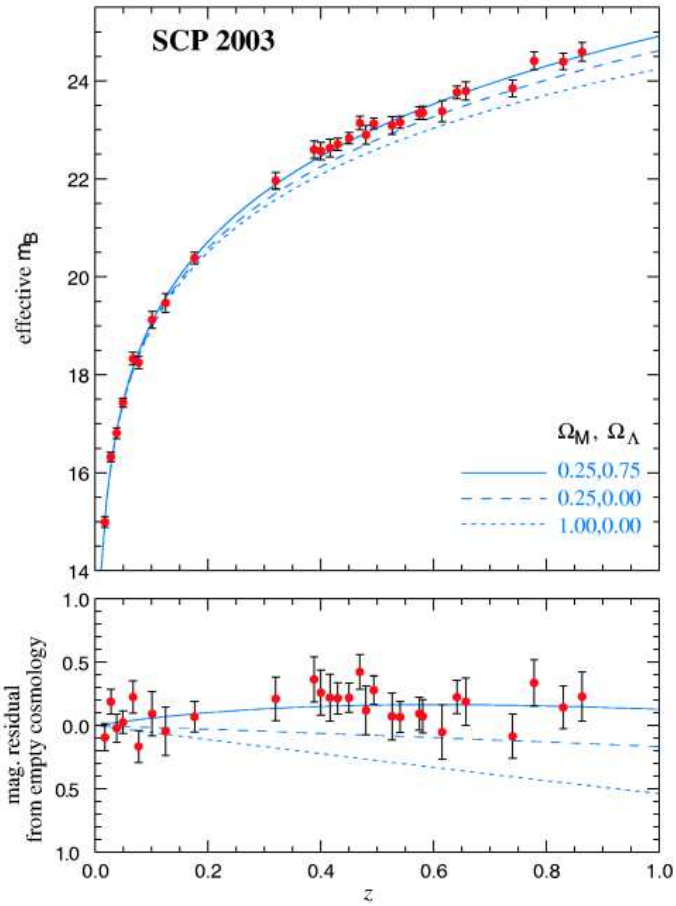

Figure 2.1: Upper panel: Hubble diagram in linear redshift scale. The solid curve represents the best-fit flat universe model, ($\Omega_m = 0.25$, $\Omega_\Lambda = 0.75$). Two other cosmological models are shown for comparison, ($\Omega_m = 0.25$, $\Omega_\Lambda = 0$) and ($\Omega_m = 1$, $\Omega_\Lambda = 0$). Lower panel: Residuals of the averaged data relative to an empty universe. From Knop *et al.* (2003).

as a function of the comoving distance $r(z)$ as

$$d_{\mathcal{L}}(z) = (1+z)r(z) \ , \tag{2.14}$$

where $r(z)$ contains the parameters of the background cosmology being defined in flat space as

$$r(z) = \int_0^z \frac{dz'}{H(z')} \ . \tag{2.15}$$

A large sample of supernovæ at high and low redshift has been observed by two independent groups: the High-Z Supernova Research Team (Riess *et al.* 1998) and the Supernova Cosmology Project (Perlmutter *et al.* 1999). Both groups have found that distant

supernovæ are fainter than expected in a matter dominated universe. In fact the data are much more consistent with a universe dominated by a Cosmological Constant. Obviously the supernova results alone allow a substantial range of possible values of Ω_m and Ω_Λ; however, if we think we know something about one of these parameters from other independent measures, the other will be tightly constrained. In particular, if we take $\Omega_m \sim 0.3$ from clustering of matter (Dodelson *et al.* 2002; Percival *et al.* 2002) and flat cosmology from Cosmic Microwave Background, (Bennett *et al.* 2003; Spergel *et al.* 2003) we get $\Omega_\Lambda \sim 0.7$ providing a direct evidence for a non-zero value of Cosmological Constant. In Fig. 2.1 we show the dimming of the supernovæ as a function of the redshift for different cosmological models.

The presence of possible systematic uncertainties in the SNIa observation has attracted some criticism (see Leibundgut 2001 for reviews). In fact the SNIa might have an evolution over the cosmic time, due to changes in characteristics of the progenitors, making their use as standard candles unreliable; but the spectra of low redshift supernovæ appear similar to those of high redshift and this evidence seems to exclude evolutionary effects in data (Hoeflich, Wheeler & Thielemann 1998; Aldering, Knop & Nugent 2000). Another possible systematics is that the dimming of the supernovæ light is due to the intergalactic dust; against this statement there is the fact that the high redshift supernovæ suffer of little reddening (Riess *et al.* 2000).

In conclusion the dimming of SNIa brought the Cosmological Constant back into the framework of the modern cosmology. In fact the presence of Λ is capable to explain the supernovæ dimming in terms of an accelerating phase of the cosmic expansion.

It is important to notice that joint measures of the CMB anisotropies and large scale structures yielded a strong indication in favor of cosmic acceleration, independently on the SNIa. The abundance of clustered matter is known to be at the 30% level of the critical density by observing the nearby Universe (Dodelson *et al.* 2002; Percival *et al.* 2002); on the other hand, the scale subtended in the sky by the acoustic oscillations in the CMB anisotropy angular power spectrum supports a flat cosmological geometry; the rather definitive confirmation came from the observation of the Wilkinson Microwave Anisotropy Probe, WMAP (see Spergel *et al.* 2003 and reference therein). The position of the first

acoustic peak of the CMB angular power spectrum is sensitive to Ω_{tot} but does not allow to constrain independently Ω_m and Ω_Λ since the relation that links the first acoustic peak location to the total energy density is roughly $l_{peak} \propto \Omega_{tot}^{-1/2}$ (see e.g. Hu & Sugiyama 1995) where l represents the multipole in the angular expansion, as we show in detail in the next chapters. Assuming the so called "Hubble Space Telescope (HST) prior" $h = 0.71 \pm 0.076$ (Freedman *et al.* 2001) on the Hubble constant, already before WMAP several experiments (BOOMERanG, Balloon Observation Of Millimetric Extragalactic Radiation and Geophysics, de Bernardis *et al.* 2000; DASI, Degree Angular Scale Interferometer, Kovac *et al.* 2002; MAXIMA, Millimeter Anisotropy eXperiment IMaging Array, Stompor *et al.* 2001) have put strong constraints on the curvature of the Universe. Restricting the analysis to a flat cosmological model ($\Omega_{tot} = 1$), then these CMB data provided $\Omega_\Lambda = 0.69^{+0.03}_{-0.06}$ for the Cosmological Constant density parameter (Sievers *et al.* 2003). At the same time, the large scale structure data gave tight constraints on Ω_m, as we anticipated. The 2dF Galaxy Redshift Survey (Percival *et al.* 2001) and the Sloan Digital Sky Survey (Dodelson *et al.* 2002) probed scales from 10 to 100 Mpc yielding $\Omega_m h^2 = 0.20 \pm 0.03$ with a baryon fraction of $\Omega_b/\Omega_m = 0.15 \pm 0.07$. When this LSS data were combined with the CMB, such a low value of the matter density gave an indirect evidence for a large value of the Cosmological Constant energy density. A joint analysis of the 2dF and the CMB data allowed to put the constrain at 2σ for the Cosmological Constant to $0.65 \leq \Omega_\Lambda \leq 0.85$ (Efstathiou *et al.* 2002).

The age of the Universe also is consistent with the presence of the Cosmological Constant. The age of a given cosmological model is obtained integrating the Friedmann equation (2.4), and it is easy to see that large values of Ω_Λ make the Universe older. Matter dominated cosmological models are younger than globular clusters, the age of which is estimated to be 11.5 ± 1.5 Gyr (Chaboyer *et al.* 1998); the presence of a Cosmological Constant alleviates this problem. On the other hand the age of the Universe can be increased also lowering the Hubble constant in a purely matter dominated cosmological model, but H_0 assumes a value too low in order to be consistent with HST prior, $h \approx 0.71 \pm 0.07$ (Freedman *et al.* 2001).

A low value of Ω_m around 0.3 is indicated by other different measures such as

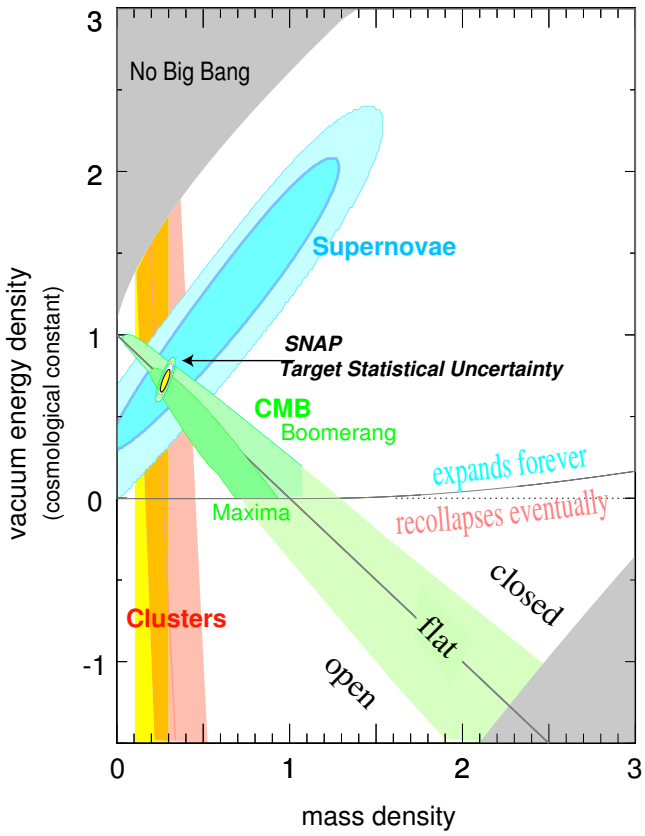

Figure 2.2: The (Ω_m, Ω_Λ) plane with the present data set of cosmological observations (the SNIa, the large scale structure and the CMB anisotropies) as well as the future determinations by SNAP. Notice the orthogonality between clusters data, supernovæ data and CMB data. From Aldering *et al.* 2002.

peculiar velocities of galaxies ($\Omega_m = 0.30 \pm 0.06$, Silberman *et al.* 2001), observed cluster mass-luminosity relation in X-ray compared with prediction from numerical simulations ($\Omega_m < 0.36$ at 1σ, Allen *et al.* 2003), gravitational lens statistics ($\Omega_m = 0.31^{+0.39}_{-0.24}$, Chae *et al.* 2002).

In Fig. 2.2 we show the combination of data from SNIa, CMB and LSS in the (Ω_m, Ω_Λ) plane as well as future experiments such as the SuperNovæ Acceleration Probe (SNAP)[1], a planned satellite to map the high redshift Type Ia supernovæ in order to constrain the cosmic acceleration over the whole relevant redshift interval (Perlmutter 2003

[1] http://snap.lbl.gov/

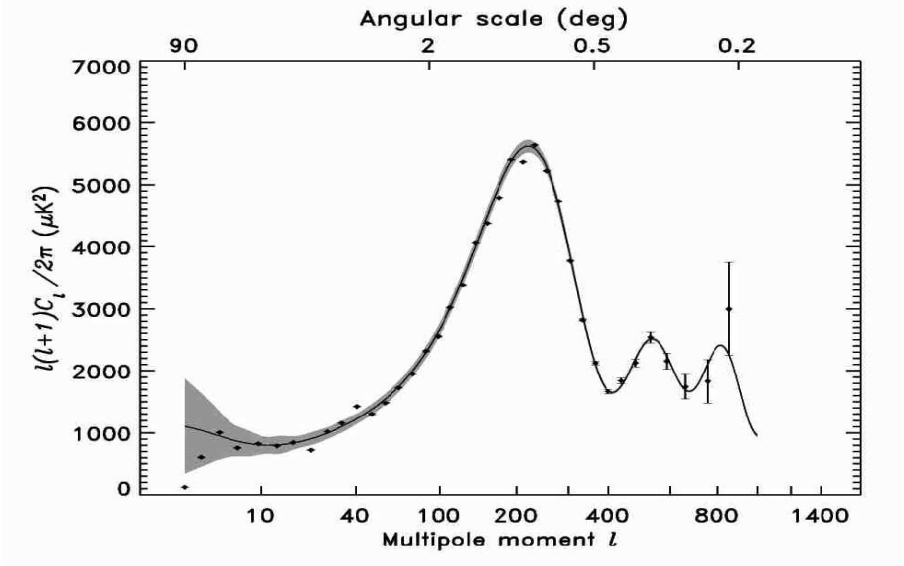

Figure 2.3: The CMB angular power spectrum, $l(l+1)C_l/2\pi$, obtained from the 28 cross-power spectra measured by WMAP satellite. The data are plotted with 1σ error, solid line is the best-fit ΛCDM model from Spergel *et al.* (2003) while the grey band is the 1σ uncertainty due to cosmic variance on the cut sky. From Hinshaw *et al.* (2003).

and references therein). Notice the complementarity between CMB data, supernovæ data and clustering data. The present picture of cosmology is built upon the combination of the full sky measure of CMB anisotropies performed by the WMAP experiment (Hinshaw *et al.* 2003) with ACBAR (Arcminute Cosmology Bolometer Array Receiver, Kuo *et al.* 2004) and CBI (Cosmic Background Imager, Pearson *et al.* 2003) experiments, the 2dF measurements (Percival *et al.* 2001) and the Lyman α forest data (Croft *et al.* 2002; Gnedin & Hamilton 2001). The observed total intensity power spectrum measured the curvature as $\Omega_K = 0.030^{+0.026}_{-0.025}$. For a flat ΛCDM cosmological model the best fit parameters are: Hubble constant $h = 0.72 \pm 0.03$, baryon density $\Omega_b h^2 = 0.0226 \pm 0.0008$ and total matter density $\Omega_m h^2 = 0.133 \pm 0.06$. The constraints concern many other most relevant cosmological observables, we list here two of them. The first structures emitting light are supposed to reionize the cosmic medium: the Thomson scattering optical depth at reionization was measured to be $\tau = 0.117^{+0.057}_{-0.053}$. Moreover, the spectrum of primordial perturbations was tightly constrained, although assuming that no gravitational waves are present, therefore reducing possible degeneration among cosmological parameters (Efstathiou 2002). As we

shall see in detail in the next chapters, the density perturbations are usually parameterized in terms of the exponent of the power spectrum of density perturbations in the Fourier space, $P(k) = \left\langle (\delta\rho/\rho)_{\vec{k}} \right\rangle \propto k^{n_s}$, where the average is taken over all the possible realization of a statistics which is assumed Gaussian; the spectral index was measured as $n_s = 0.96 \pm 0.02$. The total intensity CMB cross power spectrum with the best fit cosmological model is shown in Fig. 2.3 (Hinshaw *et al.* 2003); as we shall see in the next chapter, the C_l coefficients give a measure of the amount of anisotropy on scale given by $\vartheta \simeq 180^o/l$.

2.3 The Cosmological Constant problems

In Sec. 2.1 we wrote some basic equations in standard cosmology, including the Cosmological Constant Λ; here we want to deepen this subject reporting the problems arising when trying to exploit it in order to explain the cosmic acceleration.

The Cosmological Constant was introduced by Einstein in the gravitational field equations to make the Universe static. Since the Universe was found not static at all, Einstein himself rejected the Λ term in 1931. In the following years Λ became relevant in the context of quantum mechanics. In fact, Λ may be interpreted as a measure of the energy density of the vacuum (i.e. the state of the lowest energy) and although we cannot calculate it with any confidence from a quantum-mechanical point of view, this identification allows us to consider the energy scales of the possible contributions.

The identification of Λ with the energy of the vacuum can be shown considering a scalar field ϕ with a potential $V(\phi)$, with the action given by

$$S = \int d^4x\sqrt{-g}\left[\frac{1}{2}g^{\mu\nu}\partial_\mu\phi\partial_\nu\phi - V(\phi)\right] \ , \tag{2.16}$$

where g is the determinant of the metric tensor $g_{\mu\nu}$ and the corresponding stress-energy tensor is

$$T^{\phi}_{\mu\nu} = \partial_\mu\phi\partial_\nu\phi - g_{\mu\nu}\left[\frac{1}{2}\left(\partial^\sigma\phi\partial_\sigma\phi\right) - V(\phi)\right] \ . \tag{2.17}$$

In this theory, if the configuration with the lowest energy density exists, it will be one in which the contribution from kinetic or gradient energy is null; this implies $\partial_\mu\phi = 0$ and $T_{\mu\nu} = -V\left(\phi_0\right)g_{\mu\nu}$, where ϕ_0 minimizes the potential $V(\phi)$. Thus the stress-energy tensor

for the vacuum can be written as

$$T^V_{\mu\nu} = -\rho_V g_{\mu\nu} \ . \tag{2.18}$$

In this example ρ_V is simply given by the value of the potential in its minimum. On the other hand, comparing the above vacuum stress energy tensor with Eq. (2.3), the vacuum can be thought as a perfect fluid with $p_V = -\rho_V$. Finally, the stress-energy tensor of the vacuum contributes to the Einstein field equation just as a Cosmological Constant:

$$\rho_V = \rho_\Lambda = \frac{\Lambda}{8\pi G} \ . \tag{2.19}$$

The zero point energy, associated with quantum fluctuations in the vacuum, add another contribution from a quantistic point of view. We can see a quantum field as a collection of infinite harmonic oscillators (see e.g. Sakurai 1994), and at a quantum level it is well known that the zero point energy of such a system is infinite. The integral of the zero point energy of normal modes (with wavenumber k) of a massive scalar field (with mass m) provides the vacuum energy density and is given by

$$\rho_V = \frac{1}{2}\sum_i \omega_i = \frac{1}{(2\pi)^3}\int_0^\infty 4\pi k^2 dk \frac{\sqrt{k^2+m^2}}{2} \ , \tag{2.20}$$

that diverges as k^4. However any quantum field theory is thought to be valid up to a limiting cut-off scale, which marks the boundary to a more fundamental theory. Imposing k_{max} as cut-off in the previous integral, we obtain

$$\rho_V = \frac{k^4_{max}}{16\pi^2} \ , \tag{2.21}$$

where the mass m is neglected. The most natural choice is to set the cut-off to the Planck scale, the one given by all physical constants combined; thus the vacuum energy density will be $\rho_V^{th} \approx M_P^4 = \left(10^{19}\ \mathrm{GeV}\right)^4$. This theoretical value is very far from the observed one. Once we have a measure of the density parameter $\Omega_V = \mathcal{O}(1)$, we can give an estimate of the energy density of Λ obtaining $\rho_V^{obs} \sim \left(10^{-3}\ \mathrm{eV}\right)^4$. Comparing this "observed" value with the "theoretical" one from the particle physics, we have a discrepancy of about 120 order of magnitude. This is a quick and simplified picture of the Cosmological Constant problem, well known and unsolved in physics in the past century.

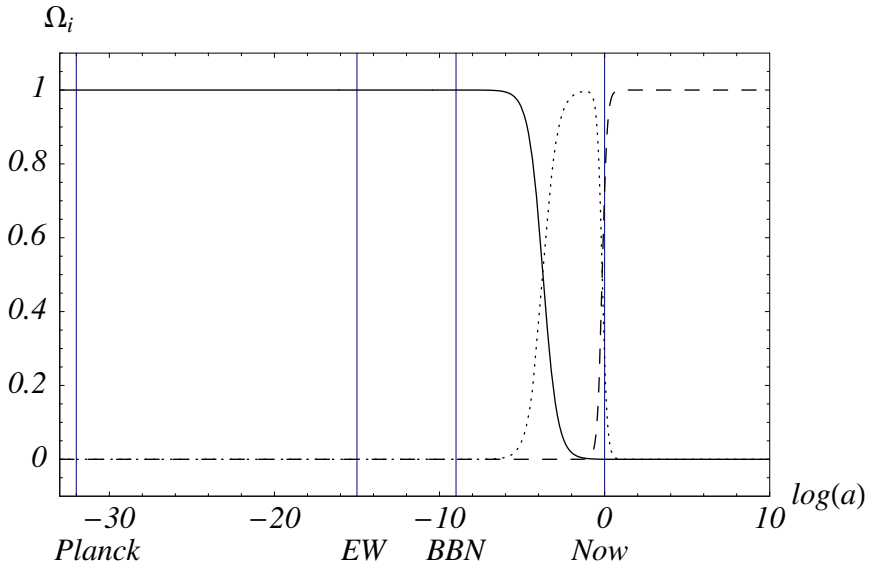

Figure 2.4: Density parameters Ω_i for radiation (solid line), matter (dotted line) and Cosmological Constant (dashed line) as a function of the scale factor a. The present values of the density parameters are 5×10^{-5}, 0.27 and 0.73 for radiation, matter and Cosmological Constant respectively. The vertical lines indicate, from left to right, the Planck era, the electroweak symmetry breaking, the Big Bang nucleosynthesis and the present.

A way to solve this problem is to invoke the Supersymmetry (SUSY, see e.g. Wess & Bagger 1992 and references therein). In the SUSY scenario, for each bosonic particle there exists a supersymmetric fermionic partner and vice-versa, leading to an exact cancellation of both bosonic and fermionic degrees of freedom. Unfortunately, since we do not observe supersymmetric particles, Supersymmetry must be broken at low energy. At the present status of the knowledge, there is no reason why such breaking should keep $\Lambda = 0$. Still, even assuming that SUSY is broken at $M_{SUSY} \sim 10^3$ GeV, which is the scale probed by current detectors, the discrepancy between the "observed" and the "theoretical" value of ρ_V is about 60 orders of magnitude. Hence any cancellation mechanism will still require a severe fine-tuning in order to explain the discrepancy between ρ_V^{th} and ρ_V^{obs}.

As well as the fine-tuning problem, the observed tiny value of Λ presents an additional problem known as the coincidence. The best fit model of our Universe in terms of energy density is of roughly 27 % of matter (baryons and cold dark matter) and 73 % of Cosmological Constant (Spergel *et al.* 2003; Tegmark *et al.* 2004, Sanchez *et al.* 2005);

these two densities are of the same order of magnitude, but their ratio changes rapidly as the Universe expands:

$$\frac{\rho_\Lambda(a)}{\rho_m(a)} = \frac{\Omega_\Lambda(a)}{\Omega_m(a)} = \frac{\Omega_\Lambda}{\Omega_m} a^3 \ . \tag{2.22}$$

As a consequence, matter and radiation dominate over the Cosmological Constant in the past times and vice-versa in the future. There is only a brief epoch of transition from the matter domination to the Cosmological Constant domination in which the densities of the two components are comparable. The coincidence is that we live right in that epoch. The evolution of the density parameters as a function of the scale factor is shown in Fig. 2.4; notice the narrow range, in terms of expansion history, for which matter and Λ abundances are comparable.

The introduction of a Cosmological Constant into the Einstein equations may explain the dimming of the SNIa, the CMB and LSS data. However, due to the theoretical difficulties outlined above, the community has been generalizing the concept of vacuum energy in cosmology. This new component, generally known as the dark energy, represents the attempt to explain the process of cosmic acceleration without invoking a Cosmological Constant.

2.4 The dark energy

The most important difference between the dark energy and the Cosmological Constant is that the dark energy is generally dynamical (see e.g. Padmanabhan 2003 and Peebles & Ratra 2003 for general reviews). A dynamical energy density may be evolving slowly to zero, allowing for a solution (at least classical) to the Cosmological Constant problem since the vacuum energy vanishes exactly at infinite times. Moreover, an evolving dark energy opens the possibility of finding a dynamical solution to the coincidence problem, if the dynamics is capable of triggering a recent takeover by the dark energy independently on the parameters in the theory, or for a wide set of those.

The easiest way to make a dynamical dark energy is to build a model with a decaying Λ imposing $w_{de} > -1$. With this parameterization the Cosmological Constant is replaced by a dark energy modeled as a fluid. The dark energy density $\rho_{de}(t)$ is approximated

as a function of time alone and interacts only with gravity and itself, while its pressure is given by $p_{de}(t) = w_{de}\rho_{de}(t)$; thus the local energy conservation is

$$\dot{\rho}_{de}(t) = -3H\rho_{de}(t)\,(1 + w_{de}) \ . \tag{2.23}$$

If w_{de} is constant in time, the dark energy density scales with the scale factor as

$$\rho_{de}(a) \propto a^{-3(1+w_{de})} \ . \tag{2.24}$$

If $w_{de} < -1/3$ the dark energy contributes positively to Eq. (2.5), while if $w_{de} = -1/3$ the dark energy mimics the effect of the curvature in the Friedmann equations. Finally if $w_{de} < -1$ the dark energy density increases with time.

From basic principles, it may be seen that any dynamical cosmological component must admit also spatial fluctuations. The minimal extension of a Cosmological Constant is represented by a scalar field, evolving slowly enough to yield an almost constant vacuum energy out of its potential and providing cosmic acceleration. Since this new component will be the fifth one in the cosmic energy budget (the other four are baryons, neutrinos, radiation and dark matter), it has been named Quintessence. As we shall see in Ch. 5, where the dark energy will be studied in more detail, it was demonstrated how the dynamics of the Quintessence (under suitable form of the potential energy) can originate attractors in the trajectory space capable to reach the present dark energy density starting from a wide set of initial conditions in the early Universe. These attractors are named tracking solutions and can alleviate the fine-tuning problem described in the previous section (see e.g. Liddle & Lyth 2000 for reviews).

Here we describe some basic principles of the scalar field dynamics, while a more detailed analysis will be done in Ch. 5. Scalar fields arise naturally in grand unified models of very high energy particle physics (see e.g. Binetruy 1999 and references therein). The total action including gravity, radiation, matter and Quintessence is

$$S = \int d^4x\sqrt{-g}\left(-\frac{R}{16\pi G} + L_f + L_\phi\right) \ , \tag{2.25}$$

where L_f is the Lagrangian density of the matter and radiation and L_ϕ is the Lagrangian density of the scalar field. The latter is given by

$$L_\phi = \frac{1}{2}\partial^\mu\phi\partial_\mu\phi - V(\phi) \ , \tag{2.26}$$

where the first term is the kinetic contribution and $V(\phi)$ is the potential that determines the characteristics of the time evolution of the scalar field. The related stress-energy tensor is given by (2.17).

In a flat FRW universe, and for a homogeneous scalar field, we can define the energy density and pressure of the dark energy as

$$\rho_\phi = \frac{1}{2}\dot{\phi}^2 + V(\phi) \ , \tag{2.27}$$

$$p_\phi = \frac{1}{2}\dot{\phi}^2 - V(\phi) \ . \tag{2.28}$$

Since the equation of state of a perfect fluid is given by $w = p/\rho$, the dark energy behaves as a perfect fluid with a time dependent equation of state

$$w_\phi = \frac{p_\phi}{\rho_\phi} = \frac{\frac{1}{2}\dot{\phi}^2 - V(\phi)}{\frac{1}{2}\dot{\phi}^2 + V(\phi)} \ . \tag{2.29}$$

If the scalar field evolves slowly in time verifying the condition $\dot{\phi}^2 \ll V(\phi)$, i.e. the kinetic energy of the field is negligible with respect its potential energy (slow rolling condition), Eq. (2.29) becomes $p_\phi \simeq -\rho_\phi$ and the scalar field approximates the effect of a Cosmological Constant. The evolution of the scalar field is obtained varying the action with respect ϕ and is described by the Klein-Gordon equation

$$\ddot{\phi} + 3H\dot{\phi} + \frac{dV}{d\phi} = 0 \ , \tag{2.30}$$

equivalent to (2.23), in which H is given by the modified Friedmann equation

$$H^2 = \frac{8\pi G}{3}\left[\rho_m(a) + \rho_r(a) + \frac{1}{2}\dot{\phi}^2 + V(\phi)\right] \ , \tag{2.31}$$

taking ϕ into account, where $\rho_m(a)$ and $\rho_r(a)$ are the matter and the radiation background energy densities respectively; in the Klein-Gordon equation, the term proportional to $\dot{\phi}$ acts as a friction term. Both the time evolution of the scalar field and the equation of state of dark energy depend on the shape of the potential. In Ch. 5 we shall discuss some relevant potentials and a phenomenological approach to the time evolution of the equation of state.

2.5 Current and new observables for the dark energy

In this chapter we have shown a brief (and surely incomplete) picture of the Universe as we know it at the beginning of the XXI century. The dimming of SNIa, the position

of the acoustic peaks in the CMB power spectrum and the clustering of matter strongly indicate the presence of a form of energy with negative pressure that contributes to the total energy density roughly for 70 %. The first candidate to explain all these observations is the Cosmological Constant, which carries theoretical problems, going back and forth between general relativity and quantum mechanics in the last century of physics. One of the main goals of the modern cosmology is to understand the nature of the dark energy and the reason for cosmic acceleration.

The combination of CMB observations with the LSS, HST and SNIa data has been used also to constrain the effective dark energy equation of state, assumed to be constant in time, to be $w_{de} < -0.78$ at 2σ confidence level imposing $w_{de} > -1$ prior and $w_{de} = -0.98 \pm 0.12$ at 1σ confidence level dropping the previous prior (Spergel *et al.* 2003). Future observations will improve that constraints, but the real challenge is to gain insight into the dark energy equation of state redshift dependence, in order to discriminate between different models. Since the dark energy starts to dominate the cosmological expansion at about the same epoch when the structures form (the two processes overlap in time), the study of structure formation is crucial for investigating the onset of cosmic acceleration. One of the most promising ways to look at that epoch is to study the weak gravitational lensing deflection induced by forming structures along the line of sight of the background light (see Bartelmann & Schneider 2001 for reviews), as we already anticipated and recall later before concluding this chapter. The shear induced by weak lensing in terms of ellipticity in the shape of background galaxies has been observed by several groups, and the results agree impressively between different telescopes and data reduction techniques (see e.g. Bacon, Refregier & Ellis 2000; Van Waerbeke *et al.* 2000; Wittman *et al.* 2000; Maoli *et al.* 2001; Van Waerbeke *et al.* 2001; Wilson, Kaiser & Luppino 2001); already, several dark energy weak lensing observables have been proposed (see e.g. Bartelmann, Perrotta & Baccigalupi 2002; Hu 2002; Huterer 2002; Bartelmann *et al.* 2003; Bernardeau 2003; Weinberg & Kamionkowski 2003;). New powerful probes to map the weak lensing shear over large sky areas are being designed to operate in the next decade with ground-based and space surveys (see Refregier *et al.* 2004 and references therein). On the CMB side, the weak lensing effect on the total intensity and polarization CMB anisotropies can be predicted

on the general basis of cosmological perturbation theory (see e.g. Hu 2000 and references therein). The effect is generally non-Gaussian, and relevant at the arcminute angular scale; attempts to detect the lensing distortion on the WMAP data produced so far no results (Hirata *et al.* 2004); it is likely that the low noise, arcminute resolution imaging expected by the Planck[2] satellite and future CMB missions will have a crucial importance in weak lensing studies. The subject of the present work is the weak lensing effect on the CMB focusing on the third order statistics and its dependence on the dark energy parameters, in particular the time dependence of the equation of state. If the background CMB light is described by a Gaussian process at last scattering, consistently with the recent CMB observations (Komatsu *et al.* 2003), it yields a zero contribution within cosmic variance to the third order statistics. As we already mentioned, a suitable harmonic approach to the weak lensing effects on the CMB total intensity and polarization has been carried out (Hu 2000), based on general description of the CMB anisotropies (Hu & White 1997).

Before concluding, let us stress once again the reason why the gravitational lensing is crucial in this context; that is simple, and relies upon a very basic property of gravitational lensing (see Bartelmann & Schneider 2001 for reviews): for a give position of the source, the lensing deflection is zero if the lens coincides with the observer or source position. Thus, the lensing is maybe the unique tool which has the built-in property of probing cosmology at redshift greater than one, *independently* on the cosmic acceleration and everything else at the present. This concept will be exploited several times in this work.

[2] http://www.rssd.esa.int/Planck

Chapter 3

CMB physics

Our work is based on the gravitational lensing of the primordial anisotropies in the CMB radiation by growing cosmological structures along the line of sight. In this chapter we provide a most relevant brick of this picture, reviewing the general CMB physics: how cosmological perturbations evolve, and how they become the CMB anisotropies imprinted at decoupling between matter and radiation, their properties in the angular domain. We also describe the other sources of anisotropies, the so called secondary ones arising along the line of sight, as well as the gravitational lensing of primordial CMB anisotropies by forming cosmological structures; the latter issue will be greatly expanded in the next chapter and later, being the subject of the whole work, in connection with the properties of the dark energy. For our purposes, it is enough to restrict our analysis to anisotropies in the thermodynamical CMB blackbody temperature, originated by linear cosmological perturbation, the dominant source of anisotropies at last scattering. We make some historical remarks about the discovery of the Cosmic Microwave Background radiation anisotropies in Sec. 3.1; we write the relevant equations for linear cosmological perturbation theory in Sec. 3.2; the Boltzmann equation is derived in Sec. 3.3; we discuss the main phenomenology of the CMB anisotropy in Sec. 3.4; we analyze the lensing effect on CMB in Sec. 3.5.

3.1 CMB: historical remark

The first idea of a relic cosmological radiation was based on the theory of element synthesis, and worked out by George Gamow in 1949 (Gamow 1949). In the fifties a somewhat detailed theoretical analysis of the present radiation temperature in connection with some early hot era where undertaken by Alpher and Herman (Alpher & Herman 1950). It was only in the mid sixties that the problem of determining the radiation temperature was once again taken up. The argument by Dicke, Peebles, Roll and Wilkinson (Dicke *et al.* 1965) was that the early Universe was hotter than 10^{10} K because of the composition of the primordial plasma, described in terms of the known particles. They suggested that the energy density of the CMB would be such that the temperature is somewhat less than or close to 40 K. An experiment by Roll and Wilkinson was prepared to measure the radiation temperature. In order to detect the relic radiation, a radiometer designed by Dicke in the mid forties was used. But, before Roll and Wilkinson could achieve the detection, they learned that Penzias and Wilson got it.

Penzias and Wilson observed a weak background signal from a horn antenna in the Bell laboratories at Holmdel, New Jersey. For Penzias and Wilson it was a truly serendipitous, well placed and beautifully timed discovery; with a temperature detection of $T \approx 3.5 \pm 1$ K (Penzias & Wilson 1965) resulting from an antenna intended to track the Echo satellite. It was at one frequency only, thus making a very little impact with respect to the expectation of a blackbody spectrum. The impact on cosmology was immense and the public perception of cosmology itself increased dramatically. This observation, published in 1965, along with the work of Dicke, Peebles, Roll and Wilkinson, was to hail the beginning of the modern CMB physics in cosmology. Penzias and Wilson received the Nobel Prize in Physics in 1978.

The closeness to isotropy suggests that the CMB uniformly fills space, meaning that an observer in another galaxy would see almost the same intensity of radiation. The spectrum is close to a blackbody, in fact the best example of a blackbody available in nature. It has a thermal planckian form with temperature of about 2.726 K. This suggests that the radiation has almost completely relaxed to thermodynamic equilibrium. This could not

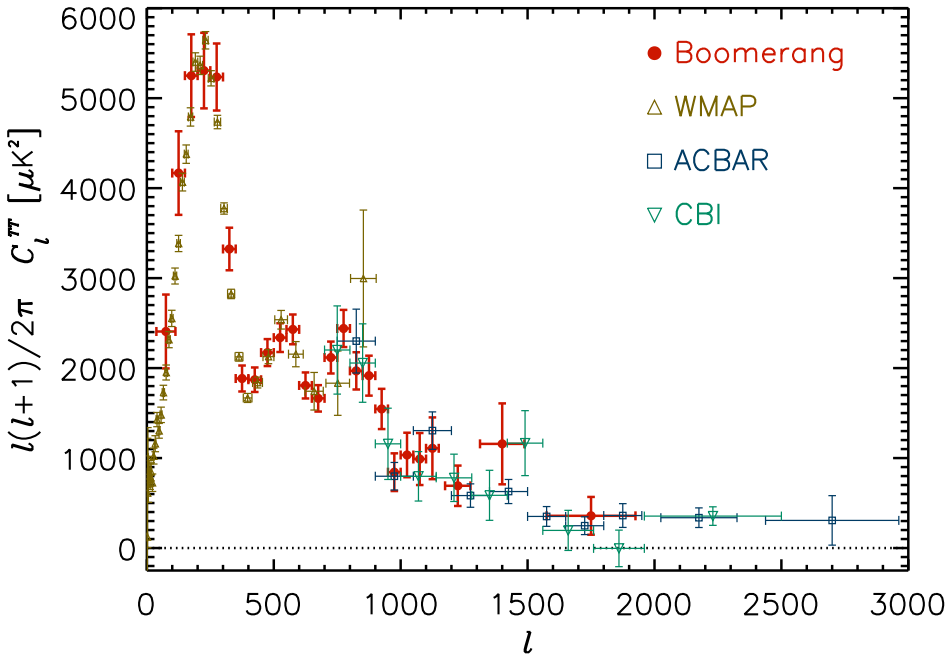

Figure 3.1: A comparison of recently published CMB power spectra, the data shown are from Hinshaw *et al.* (2003) for WMAP, Kuo *et al.* (2004) for ACBAR, Readhead *et al.* (2004) for CBI and Jones *et al.* (2005) for BOOMERanG. The data are derived from measures in a band extending from 20 GHz to 200 GHz. From Jones *et al.* (2005).

have happened recently as the Universe is currently optically thin to radiation. The CMB can move across the present Universe on scale of the Hubble length with little change other than that caused by the expansion. The interpretation is that the CMB is left over from an earlier time when the expanding universe was dense and hot, and the interaction rates between particles were rapid enough to have allowed a relaxation to thermal equilibrium, thus filling space with a sea of blackbody radiation. Furthermore, when the interaction is negligible, cooling is due to the expansion only, preserving the thermal spectrum. When the radiation interacts with the matter, because the heat capacity of the radiation is very much larger than that of the matter, the spectrum will still tend to remain close to a blackbody. A nearly thermal spectrum of blackbody radiation is thus an expected signature of an expanding universe in which the radiation is that left over from a early hot dense era.

There is however structure in the universe, we see galaxies and clusters of galaxies, stars and other interesting objects and phenomena. If the CMB was perfectly isotropic

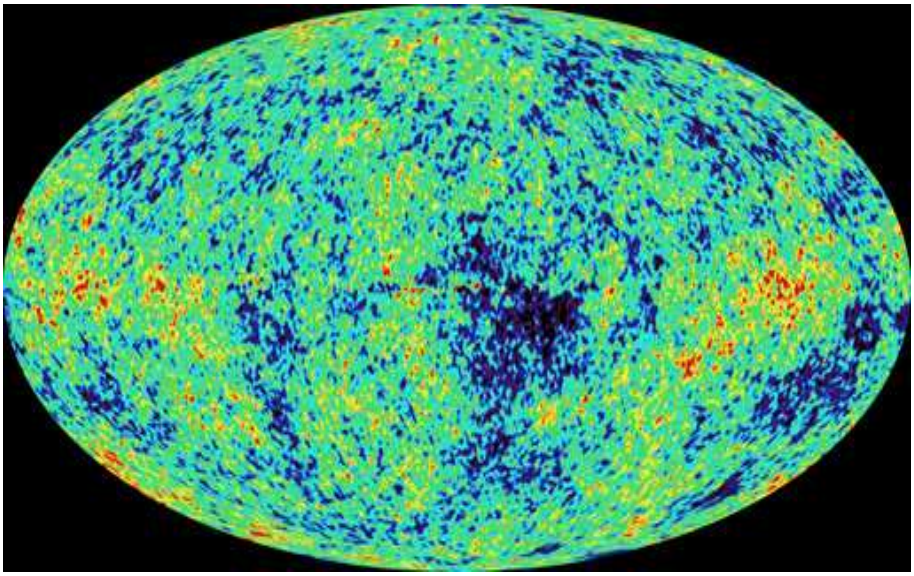

Figure 3.2: Weighted linear combination of the five 1 year WMAP frequency maps (23, 33, 41, 61 and 94 GHz). The weights are computed using criteria which minimize the Galactic foreground contribution to the sky signal. The resulting map provides a low contamination image of the whole sky CMB anisotropy at degree resolution. Red spots are at higher temperature than the average, while blues spots are colder; the amplitude is of the order of 10 μK. From http://lambda.gsfc.nasa.gov website.

one would have expected that there were no deviations from isotropy and homogeneity in the early Universe; where then would the structure come from? In the Big Bang Model, complex structures arise from primordial perturbations, which grow by gravitational instability as a result of the expansion. In the last years several experiments have been developed to detect such anisotropies, the most important are: ACBAR[1] (Goldstein *et al.* 2003); BOOMERanG[2] (de Bernardis *et al.* 2000); CBI[3] (Sievers *et al.* 2003); COBE[4], COsmic Background Explorer (Bennett *et al.* 1994); DASI[5] (Kovac *et al.* 2002); MAXIMA[6], (Stompor *et al.* 2001); WMAP[7] (Bennett *et al.* 2003). In Fig. 3.1 we plot a collection of some of the most recent CMB power spectrum data, the degree of consistency between

[1] http://cosmology.berkeley.edu/group/swlh/acbar/
[2] http://cmb.phys.cwru.edu/boomerang/
[3] http://www.astro.caltech.edu/~tjp/CBI/
[4] http://lambda.gsfc.nasa.gov/product/cobe/
[5] http://astro.uchicago.edu/dasi/
[6] http://cosmology.berkeley.edu/group/cmb/
[7] http://map.gsfc.nasa.gov/

such a diverse set of measurements is remarkable. The COBE satellite that was flown in 1989-1996 made the first detection of the large scale anisotropies (other than the dipole, which is due to our motion with respect to the reference frame where it is zero). Inspired by the COBE results, a series of ground-based and balloon-borne experiments, actually all the experiments mentioned above except WMAP, measured CMB anisotropies on smaller angular scales over the next decade. The primary goal of these experiments was to measure the CMB anisotropies on the degrees scales, or somewhat less, corresponding to distances in causal coupling at the epoch at which the CMB decouples from the rest of the system. As we shall see in detail in the following, on these angular scales acoustic oscillations (acoustic peaks) are expected to occur, originated by photons and baryons bouncing in the gravitational potential wells provided by the dark matter, because of their pressure. The first acoustic peak was measured with increasing sensitivity when the BOOMERanG experiment reported that the highest power fluctuations occur at about one degree scales. Together with other cosmological data, these results implied that the geometry of the Universe is flat, i.e. described essentially by a Minkowski metric with expanding distances (de Bernardis *et al.* 2000). In June 2001, NASA launched a second CMB space mission, WMAP, to make detailed measurements of the anisotropies over the full sky (see Fig. 3.2). As we stressed already in the Ch. 2, the results of this mission, combined with other ones, provide a detailed measurement of the angular power spectrum down to a scale corresponding to a few tens of arcminutes (see Fig. 2.3), tightly constraining various cosmological parameters. The results are broadly consistent with those expected from cosmic inflation (see e.g. the WMAP first-year results: Bennett *et al.* 2003; Hinshaw *et al.* 2003; Komatsu *et al.* 2003; Peiris *et al.* 2003; Spergel *et al.* 2003) and are available in detail at NASA's data center for Cosmic Microwave Background[8].

3.2 Linear cosmological perturbation theory

The CMB anisotropies arise from perturbations in the metric and the stress-energy tensors, introduced in the previous chapter. In this section we classify these perturbations

[8]http://lambda.gsfc.nasa.gov/

and analyze their evolution in the linear regime. In general, the latter means that cosmological equations split in a set describing the homogeneous and isotropic cosmological expansion, having the cosmic time t as the dynamical variable, plus another one describing perturbations, assumed small enough not to interfere with the background and featuring a dependence on the generic spacetime coordinate x:

$$\overline{G}_{\mu\nu}(x) = 8\pi G \overline{T}_{\mu\nu}(x) \equiv \begin{cases} G_{\mu\nu}(t) = 8\pi G T_{\mu\nu}(t) & \text{background} \\ \delta G_{\mu\nu}(x) = 8\pi G \delta T_{\mu\nu}(x) & \text{perturbations} \end{cases} . \tag{3.1}$$

Similarly, concerning conservation equations, one has

$$\overline{T}^{\nu}_{\mu;\nu}(x) = 0 \rightarrow \begin{cases} T^{\nu}_{\mu;\nu}(t) = 0 & \text{background} \\ \delta T^{\nu}_{\mu;\nu}(x) = 0 & \text{perturbations} \end{cases} . \tag{3.2}$$

We shall work out the different ingredients composing the fluctuations above, in the metric as well as the stress energy tensors. Our treatment and notation is based on the original works by Kodama and Sasaki (1984) and Hu and White (1997); see also Mukhanov, Feldmann and Brandenberger (1992) for further details.

3.2.1 Perturbation classification

The metric and the stress-energy perturbations can be classified in terms of their property under spatial rotation into scalar, vector and tensor components (Kodama & Sasaki 1984). It is convenient to expand those in the Fourier space, as in the linear limit the different modes do not mix simply because no products of perturbations appear into the equations. We describe here the eigenfunctions of such expansion. Those of the Laplacian operator are:

$$\begin{aligned} \nabla^2 Q^{(0)} &= -k^2 Q^{(0)} \text{ (scalar)} , \\ \nabla^2 Q^{(1)}_i &= -k^2 Q^{(1)}_i \text{ (vector)} , \\ \nabla^2 Q^{(2)}_{ij} &= -k^2 Q^{(2)}_{ij} \text{ (tensor)} . \end{aligned} \tag{3.3}$$

In a flat ($K = 0$) cosmology, the solutions are

$$
\begin{aligned}
Q^{(0)} &= \exp\left(i\vec{k}\cdot\vec{x}\right) , \\
Q_i^{(1)} &= -\frac{i}{\sqrt{2}}\left(\hat{e}_1 \pm i\hat{e}_2\right)_i \exp\left(i\vec{k}\cdot\vec{x}\right) , \\
Q_{ij}^{(2)} &= -\sqrt{\frac{3}{8}}\left(\hat{e}_1 \pm i\hat{e}_2\right)_i \otimes \left(\hat{e}_1 \pm i\hat{e}_2\right)_j \exp\left(i\vec{k}\cdot\vec{x}\right) ,
\end{aligned}
\tag{3.4}
$$

where $\hat{e}_1$, $\hat{e}_2$ and $\hat{e}_3$ form an orthogonal basis. Notice that scalar perturbations are represented by pure plane waves. From scalar modes we can build the so called scalar-type vector and symmetric tensor quantities simply performing spatial derivatives:

$$
\begin{aligned}
Q_i^{(0)} &= -\frac{1}{k}\nabla_i Q^{(0)} , \\
Q_{ij}^{(0)} &= \left[\frac{1}{k^2}\nabla_i\nabla_j + \frac{1}{3}\delta_{ij}\right] Q^{(0)} ,
\end{aligned}
\tag{3.5}
$$

where δ_{ij} is the Kronecker's Delta. The scalar-type component of vectors is irrotational by construction $\left(\vec{\nabla}\times\vec{Q}^{(0)} = 0\right)$, while $Q_i^{(1)}$ in (3.4) generally describes a rotational field. On the other hand vector perturbations are divergenceless $\left(\nabla^i Q_i^{(1)} = 0\right)$, thus describing a vorticity velocity field. Similarly, by spatial derivatives of vector perturbations we can describe the vector-type component of tensors:

$$
Q_{ij}^{(1)} = -\frac{1}{2k}\left[\nabla_i Q_j^{(1)} + \nabla_j Q_i^{(1)}\right] . \tag{3.6}
$$

As it is evident from Eqs. (3.4) the tensor perturbations must satisfy the transverse-traceless condition $\left(\delta^{ij}Q_{ij}^{(2)} = \nabla^i Q_{ij}^{(2)} = 0\right)$; scalar-type and vector-type component of tensors cannot be built from the modes $Q_{ij}^{(2)}$. Here and in the following we are omitting the k arguments in the Q functions for all cosmological perturbations to slim the formalism.

3.2.2 Metric and stress-energy tensor perturbations

Now we are able to perform the Fourier expansion of cosmological perturbations of any kind, if the solutions of the Laplace operator are (3.4) in flat space. The perturbed metric $g_{\mu\nu}$ can be written in terms of the unperturbed Minkowski metric $\gamma_{\mu\nu} = \mathrm{diag}(-1,1,1,1)$ and the metric fluctuations $h_{\mu\nu}$ as

$$
g_{\mu\nu} = a^2\left(\gamma_{\mu\nu} + h_{\mu\nu}\right) . \tag{3.7}
$$

Linearity is expressed by the condition $h_{\mu\nu} \ll 1$. Due to the linearization, vectors and scalars are affected by a gauge freedom, arising from shifting the coordinate frame with respect to the background. It may be shown that the gauge freedom allows for two independent perturbation quantities for scalars, one for vectors and one for tensors (Kodama & Sasaki 1984). In this work we adopt the conformal Newtonian gauge exhibiting degrees of freedom along the diagonal of the metric tensor:

$$\begin{aligned} h_{00} &= 2\Psi Q^{(0)} \ , \\ h_{ij} &= 2\Phi Q^{(0)} \delta_{ij} \ . \end{aligned} \tag{3.8}$$

For the vectors the contribution is defined as

$$h_{0i} = -V Q_i^{(1)} \ , \tag{3.9}$$

while for the tensors it is

$$h_{ij} = 2H Q_{ij}^{(2)} \ . \tag{3.10}$$

As well as the metric, also the stress-energy perturbations can be broken up into scalar, vector and tensor contributions. The perturbed stress-energy tensor is

$$\overline{T}_\mu^\nu = T_\mu^\nu + \delta T_\mu^\nu \ , \tag{3.11}$$

where T_μ^ν represents the unperturbed one, already defined in Sec. 2.1. The decomposition of the fluctuations into the normal modes is defined as

$$\begin{aligned} \delta T_0^0 &= -\rho \delta Q^{(0)} \ , \\ \delta T_i^0 &= (\rho + p)\, v^{(0)} Q_i^{(0)} \ , \\ \delta T_0^i &= -(\rho + p)\, v^{(0)} Q^{(0)i} \ , \\ \delta T_j^i &= \delta p Q^{(0)} \delta_j^i + p \pi^{(0)} Q_j^{(0)i} \ , \end{aligned} \tag{3.12}$$

for the scalar components,

$$\begin{aligned} \delta T_i^0 &= (\rho + p) \left[v^{(1)} - V \right] Q_i^{(1)} \ , \\ \delta T_0^i &= -(\rho + p)\, v^{(1)} Q^{(1)i} \ , \\ \delta T_j^i &= p \pi^{(1)} Q_j^{(1)i} \ , \end{aligned} \tag{3.13}$$

for the vector components and

$$\delta T^i_j = p\pi^{(2)} Q^{(2)i}_j \ , \tag{3.14}$$

for the tensor components; $\delta = \delta\rho/\rho$ represents the fluid density contrast, v is the peculiar velocity, δp is the isotropic pressure perturbation and π is the anisotropic stress or shear. In the following we consider the scalar perturbations only, dropping the (0) script. Therefore, the perturbed length element can be written as

$$ds^2 = a^2(\eta)\left[-(1-2\Psi)d\eta^2 + (1+2\Phi)dx^i dx_i\right] \ , \tag{3.15}$$

where $d\eta = dt/a$ is the conformal time, x^i is the spatial coordinate and the potential Ψ plays the role of the gravitational potential in the Newtonian limit.

As we stressed already, to express the metric evolution in terms of the matter sources and to evolve the matter and metric perturbations we need to perturb the Einstein equations $G_{\mu\nu} = 8\pi G T_{\mu\nu}$ and the energy-momentum conservation $T^{\mu\nu}_{;\nu} = 0$. Using the expression of the metric (3.15) and the scalar perturbations of the stress-energy tensor, the dynamical equations for the independent metric fluctuations, the so called generalized Poisson equations, are written as

$$k^2\Phi = 4\pi G a^2\left[\rho\delta + \frac{3}{k}\mathcal{H}(\rho+p)v\right] \ , \tag{3.16}$$

$$k^2(\Psi+\Phi) = -8\pi G a^2 p\pi \ , \tag{3.17}$$

where $\mathcal{H} = a^{-1}da/d\eta$. The corresponding matter evolution is given by the perturbation of the energy-momentum conservation $T^{\mu\nu}_{;\nu} = 0$, which gives the evolution equations for density contrast and peculiar velocity, and is written as

$$\frac{d\delta}{d\eta} = -(1+w)\left(kv + 3\frac{d\Phi}{d\eta}\right) - 3\mathcal{H}\delta w \ , \tag{3.18}$$

$$\frac{d}{d\eta}[(1+w)v] = (1+w)\left[k\Psi - \mathcal{H}(1-3w)v\right] + wk\left(\frac{\delta p}{p} - \frac{2}{3}\pi\right) \ , \tag{3.19}$$

where $w = p/\rho$. The first equation represents the energy density conservation while the second one is the momentum density conservation; they remain true for each fluid individually in the absence of momentum exchange. Even though the Universe passes through epochs in which is dominated by a single energy component (such as radiation, matter

or dark energy), there are also transient phases in which more components may dominate and interact; here we want to give the basic criteria generalizing the quantities above in a multi-component system. The pressure and the stress-energy tensor of a multicomponent fluid are the sum of the quantities of each component. The total stress-energy tensor must be conserved, but the divergence of the stress-energy tensor for a single component may be generally non-zero. An example of this occurrence is the photon-baryon system which we treat next. The density contrast, the pressure contrast, the peculiar velocity, the anisotropic stress and the equation of state of the multicomponent fluid are related to those of each component by (Kodama & Sasaki 1984):

$$\begin{aligned}
\delta_{tot} &= \frac{1}{\rho_{tot}} \sum_i \rho_i \delta_i \ , \\
\left(\frac{\delta p}{p}\right)_{tot} &= \frac{1}{p_{tot}} \sum_i p_i \left(\frac{\delta p}{p}\right)_i \ , \\
v_{tot} &= \frac{1}{(\rho_{tot} + p_{tot})} \sum_i (\rho_i + p_i)\, v_i \ , \\
\pi_{tot} &= \frac{1}{p_{tot}} \sum_i p_i \pi_i \ , \\
w_{tot} &= \frac{p_{tot}}{\rho_{tot}} = \frac{\sum_i p_i}{\sum_i \rho_i} \ .
\end{aligned} \tag{3.20}$$

Eqs. (3.16) - (3.19) still hold formally in a multi-component system with the quantities above.

3.3 The Boltzmann equation and the line of sight approach

The Boltzmann equation describes the time evolution of the spatial and the angular distribution of the radiation under gravity and scattering processes. Throughout this work we use dimensionless quantities for the CMB, following Hu and White (1997); $\Theta = \Delta T/T$ is the temperature fluctuation of the CMB anisotropies ($T = 2.726$ K is the average CMB temperature) and it is a function of the conformal time η, the position $\vec{x}$ and the photon propagation direction $\hat{n}$. The Boltzmann equation is written as

$$\frac{d}{d\eta}\Theta\left(\eta, \vec{x}, \hat{n}\right) \equiv \frac{\partial \Theta}{\partial \eta} + n^i \nabla_i \Theta = C(\Theta) + G\left(h_{\mu\nu}\right) \ , \tag{3.21}$$

where $n^i = dx/d\eta$ and we used the fact that in a flat universe the photons propagate in straight lines with $dn^i/d\eta = 0$. The two terms G and C take into account the gravitational redshift and the electromagnetic scattering of photons on electrons, respectively. At decoupling energies, ($T_{dec} \approx 3000$ K), the electromagnetic interaction may be described by Thomson scattering. In the following we specify G and C. The CMB anisotropies possess also fluctuations in polarization that are due to the anisotropic nature of the Thomson scattering. We do not treat those in this work.

The contribution to the temperature fluctuations due to the gravitational redshift can be derived from the Euler-Lagrange equations of motion for a photon (Kodama & Sasaki 1984); it is

$$\frac{1}{q}\frac{dq}{d\eta} = -\mathcal{H} - \frac{1}{2}n^i n^j \frac{dh_{ij}}{d\eta} - n^i \frac{dh_{0i}}{d\eta} - \frac{1}{2}n^i \nabla_i h_{00} \ , \tag{3.22}$$

where $q \equiv -u^\mu q_\mu$ is the energy of the photon, u^μ is the four-velocity of an observer at rest in the background frame, q_μ is the photon four-momentum and $u_\mu u^\mu = 1$. Since the first term in the right hand side of Eq. (3.22) does not affect Θ (it is the cosmological redshift) and the third one is null because in our gauge the perturbed metric is diagonal, the contribution to the Boltzmann equation from gravitational redshift is simply reduced to

$$G\left(h_{\mu\nu}\right) = \frac{1}{2}\left(n^i \nabla_i h_{00} + n^i n^j \frac{dh_{ij}}{d\eta}\right) \ . \tag{3.23}$$

The differential cross section of the Thomson scattering is given by

$$\frac{d\sigma}{d\Omega} = \frac{3\sigma_T}{8\pi}\left|\hat{\epsilon}\cdot\hat{\epsilon}'\right|^2 \ , \tag{3.24}$$

where σ_T is the Thomson scattering cross section, $\hat{\epsilon}$ and $\hat{\epsilon}'$ are the outgoing and the incoming polarization vectors, respectively, in the electron rest frame. The contribution to the temperature fluctuations due to the Thomson scattering is conveniently computed in the electron rest frame. The Thomson scattering matrix is diagonal when expressed in terms of the intensities of radiation parallel and perpendicular to the plane containing both the incident photon and the scattered one. For reasons that shall be clear in the following, it is convenient to work in a frame having the $\hat{e}_3$ axis defined in (3.4) coincident with $\hat{k}$. This frame is called $\hat{k}$-frame, and its use is crucial when dealing with non-Gaussian perturbations (Baccigalupi 1999). To calculate C, one may perform two rotations from the $\hat{k}$-frame to the

scattering one and vice-versa (see Hu & White 1997 and references therein). Moreover, a boost is needed to go from the electron rest frame to the background frame, which yields a Doppler shift in the temperature of the scattered photon given by $\hat{n} \cdot \vec{v}_B$, where $\vec{v}_B$ is the baryon peculiar velocity. Introducing the differential optical depth $d\tau/d\eta = an_e\sigma_T$, that sets the collision rate, where n_e is the density of free electrons and a is the scale factor, after some rotational algebra one finds that the scattering term C is (Ma & Bertschinger 1995; Hu & White 1997)

$$C(\Theta) = -\frac{d\tau}{d\eta}\left(\Theta - \int \frac{d\Omega'}{4\pi}\Theta' + \hat{n}\cdot\vec{v}_B - \frac{1}{10}Y_{2\,0}\int d\Omega' Y'_{2\,0}\Theta'\right) \ , \tag{3.25}$$

where the prime indicates the quantities before the scattering. The integrals are evaluated over all the directions of the incoming photons and $Y_{2\,0}$ are the spherical harmonics with $l = 2$ and $m = 0$.

We are able now to write the explicit form of the Boltzmann equation taking the Fourier transform of Eq. (3.21) and expanding each term in normal modes. Such expansion for the temperature fluctuations may be written as

$$\Theta = \int \frac{d^3k}{(2\pi)^3} e^{i\vec{k}\cdot\vec{x}} \sum_{l=0}^{\infty} (-i)^l \sqrt{\frac{4\pi}{2l+1}} Y_{l\,0}\Theta_l \ . \tag{3.26}$$

The multipole m does not compare into the spherical harmonics expansion (3.26); the reason is that for each wavenumber $\vec{k}$, the angular expansion is made in the $\hat{k}$-frame: it is possible to show that, if only scalar perturbations are present, the $m = 0$ are the only modes excited (Hu & White 1997). The gradient term $n^i\nabla_i$ becomes $i\hat{n}\cdot\vec{k} = ik\sqrt{\frac{4\pi}{3}}Y_{1\,0}$ in the Fourier space and in the $\hat{k}$-frame, and multiplies the intrinsic angular dependence of the temperature distribution in Eq. (3.26); the net effect is that gradients in the distribution produce temperature anisotropies. This behavior involves the Clebsh-Gordan relation and couples the l moments of the distribution to the $l \pm 1$ ones as

$$\sqrt{\frac{4\pi}{3}} Y_{1\,0} Y_{l\,0} = \frac{l}{\sqrt{(2l+1)(2l-1)}} Y_{(l-1)\,0} + \frac{l+1}{\sqrt{(2l+1)(2l+3)}} Y_{(l+1)\,0} \ . \tag{3.27}$$

The Boltzmann equation follows directly from the previous relation, yielding a hierarchy of

coupled differential equations, written as

$$\frac{d\Theta_l}{d\eta} = k\left(\frac{l}{2l-1}\Theta_{l-1} - \frac{l+1}{2l+3}\Theta_{l+1}\right) - \frac{d\tau}{d\eta}\Theta_l + \begin{cases} \frac{d\tau}{d\eta}\Theta_0 - \frac{d\Phi}{d\eta} & (l=0) \\ \frac{d\tau}{d\eta}v_B + k\Psi & (l=1) \\ \frac{1}{10}\frac{d\tau}{d\eta}\left(\Theta_2 - \sqrt{6}E_2\right) & (l=2) \\ 0 & (l>2) \end{cases} , \quad (3.28)$$

where E_2 is the quadrupole of the electric-type polarization of the incoming photons (see Hu & White 1997 for more details). The first term on the right hand side of (3.28) is the free streaming effect transferring power on different scales, while the second one takes into account the main effect of scattering; the last terms account for the gravitational and residual scattering effects. Eqs. (3.28) form a coupled system of differential equations that can be solved with the evolution of the metric sources. The lowest order equations, for $l = 0$ and $l = 1$, reproduce the conservation and continuity equations for a blackbody radiation. Indeed, specifying Eq. (3.18) for the photons and comparing that with the $l = 0$ and $l = 1$ equations of (3.28), one has $\delta_\gamma = 4\Theta_0$ and $v_\gamma = \Theta_1$. Defining the baryon to photon ratio as $R = 3\rho_B/4\rho_\gamma$, the energy momentum conservation equations for the baryons become

$$\frac{d\delta_B}{d\eta} = -kv_B - 3\frac{d\Phi}{d\eta} , \quad (3.29)$$

$$\frac{dv_B}{d\eta} = -\mathcal{H}v_B + k\Psi + \frac{1}{R}\frac{d\tau}{d\eta}(\Theta_1 - v_B) , \quad (3.30)$$

where the last term in the momentum conservation gives us the form of the coupling between photons and baryons.

Defining the optical depth between η and η_0, being η_0 the conformal time at the present, as $\tau(\eta) = \int_\eta^{\eta_0} \frac{d\tau}{d\eta}(\eta')d\eta'$, the solution to the Boltzmann equation (3.28) can be formally written as an integral along the photon past light cone

$$\frac{\Theta_l(k,\eta_0)}{2l+1} = \int_0^{\eta_0} d\eta e^{-\tau} \cdot \\ \cdot \left\{ \left[\frac{d\tau}{d\eta}(\Theta_0 + \Psi) + \frac{d\Psi}{d\eta} - \frac{d\Phi}{d\eta}\right] j_l^0(x) + v_B\frac{d\tau}{d\eta}j_l^1(x) + \frac{\Theta_2 - \sqrt{6}E_2}{10}\frac{d\tau}{d\eta}j_l^2(x) \right\} , \quad (3.31)$$

with $x = k(\eta_0 - \eta)$; the combination $\frac{d\tau}{d\eta}e^{-\tau}$ is the visibility function expressing the probability that a photon is last scattered between η and $\eta + d\eta$, and is sharply peaked at the last

scattering epoch, $z \approx 1100 \pm 100$ in typical cosmologies. The previous equation is simply the projection of the various plane wave sources (i.e. the last terms of Eq. (3.28)) on the sky today with

$$\begin{aligned} j_l^0(x) &= j_l(x) \ , \\ j_l^1(x) &= \frac{d}{dx} j_l(x) \ , \\ j_l^2(x) &= \frac{1}{2}\left[3\frac{d^2}{dx^2} j_l(x) + j_l(x)\right] \ . \end{aligned} \tag{3.32}$$

In the term $\frac{d\tau}{d\eta} e^{\tau}(\Theta_0 + \Psi)$ of Eq. (3.31) we can recognize the intrinsic anisotropy and the gravitational potential contributions from the last scattering surface that acts as an effective temperature and gives us the Sachs-Wolfe effect at last scattering. The term $e^{\tau}\left(\frac{d\Psi}{d\eta} - \frac{d\Phi}{d\eta}\right)$ is the so called integrated Sachs-Wolfe effect after last scattering, as we discuss later. $v_B \frac{d\tau}{d\eta}$ is the the Doppler term and the last term arises from the anisotropic Thomson scattering. The main advantage of Eq. (3.31) is that it decomposes the anisotropy into a source term, which does not depend on the multipole moment, and a geometrical term, including the j_l and their derivatives, which does not depend on the particular cosmological model. The latter only needs to be computed once and can be stored for subsequent calculations, while the source term is the same for all multipoles and only depends on a small number of contributors (gravitational potentials, baryon velocity and photon moments up to $l = 2$, Seljak & Zaldarriaga 1996). By specifying the source term as a function of time, one can compute the corresponding spectrum of anisotropies; however, formally in Eq. (3.31) the first moments appear on both sides of equations. To solve for these moments one uses the equations in their differential form (3.28); once the moments that enter into the source function are computed, one can solve for the higher ones by performing the integration in (3.31).

Finally, let us define the CMB angular power spectrum, mapping the anisotropy power on different angular scales. The CMB anisotropy power spectrum is defined in terms of the coefficients a_{lm} of the harmonic expansion of the temperature $\Theta = \sum_{lm} a_{lm} Y_{lm}$, in a generic frame fixed for all wavevectors, averaged all the m values:

$$C_l = \frac{1}{2l+1} \sum_{m=-l}^{l} |a_{lm}|^2 \ . \tag{3.33}$$

In terms of the Fourier expansion, using Eq. (3.26) it may be seen that the power spectrum today gets

$$C_l = \frac{2}{\pi} \int \frac{dk}{k} \frac{k^3 |\Theta_l(k, \eta_0)|^2}{(2l+1)^2} \ . \tag{3.34}$$

This completes the set of equations which can be exploited to numerically evolve CMB anisotropies along with cosmological perturbations. We now turn to study their phenomenology.

3.4 CMB anisotropy phenomenology

Before recombination the differential optical depth is very large and the scattering between photons and baryons is very rapid and efficient. This regime is called the tight coupling and is active at scales such that $k/(d\tau/d\eta) \ll 1$: photons and baryons behave as a single fluid and their velocities are the same at the 0^{th} order in $k/(d\tau/d\eta)$. Under this assumption, we can combine the equations (3.28) for $l = 0$ and $l = 1$ with the Euler equation for the baryons in the tight coupling limit, obtaining the second order equation

$$\frac{d^2\Theta_0}{d\eta^2} + \frac{1}{1+R}\frac{dR}{d\eta}\frac{d\Theta_0}{d\eta} + k^2 c_s^2 \Theta_0 = -\frac{d^2\Phi}{d\eta^2} - \frac{1}{1+R}\frac{dR}{d\eta}\frac{d\Phi}{d\eta} - \frac{k^2}{3}\Psi \ , \tag{3.35}$$

where $c_s = [3(1+R)]^{-1/2}$ is the photon-baryon sound speed (Doroshkevich, Zel'dovich & Sunyaev 1978) and the right hand side is a forcing function due to cosmological perturbations. The sound speed defines formally another horizon in the particular problem at hand, besides the Hubble horizon H^{-1}. However, in typical cosmological models the baryon abundance is subdominant at last scattering, so that R does not introduce a significant correction to the sound speed; therefore at any time $c_s \simeq \eta/\sqrt{3}$; moreover, it is easy to see that for a power law evolution of the scale factor with time, like in matter or radiation dominated eras, the Hubble horizon is proportional to the time itself. Therefore, sound and Hubble horizons represent physically the same quantity in typical cosmologies, and we keep mentioning generically horizon below indicating both of them. In the tight coupling limit Eq. (3.35) has three main contributions to the evolution of Θ_0, which we treat in detail in Section 3.4.1:

- $k^2 c_s^2 \Theta_0$ is the photon pressure, supporting the oscillations of the photon-baryon plasma and is relevant on sub-horizon scales;
- $-\frac{d^2\Phi}{d\eta^2} - \frac{1}{1+R}\frac{dR}{d\eta}\frac{d\Phi}{d\eta}$ yields the constancy of $\Theta_0 + \Phi$ on super-horizon scales;
- $-\frac{k^2}{3}\Psi$ is the gravitational infall of the photon-baryon fluctuations in the potential well, relevant on sub-horizon scales.

Eq. (3.35) describes a forced harmonic oscillator with the effective dimensionless mass $m_{eff} = 1 + R$, simply accounting for the inertia of baryons, as it is evident if we rewrite it as (Peebles & Yu 1970):

$$\frac{d}{d\eta}\left(m_{eff}\frac{d\Theta_0}{d\eta}\right) + \frac{k^2}{3}\Theta_0 = -\frac{k^2}{3}m_{eff}\Psi - \frac{d}{d\eta}\left(m_{eff}\frac{d\Phi}{d\eta}\right) \ . \tag{3.36}$$

Baryons contribute to the gravitational mass of the system as it is evident by the presence of m_{eff} on the right hand side of Eq. (3.36), while they do not contribute significantly to the pressure or restoring force of the system. The change in the momentum of the photon-baryon fluid is determined by a competition between pressure restoring and gravitational driving force.

In the following we discuss qualitatively the primary and the secondary anisotropies, arising at last scattering and along the line of sight, respectively.

3.4.1 Primary anisotropies

Let us assume that both the gravitational potentials Ψ and Φ and the baryon to photon ratio R are constant in time. The first statement is true on super-horizon scales in a flat universe dominated by matter or radiation, while both of them are true on sub-horizon scales, on time intervals much shorter than the Hubble scale. Under these assumptions, Eq. (3.35) becomes the equation of an harmonic oscillator with constant acceleration provided by gravitational infall:

$$\frac{d^2\Theta_0}{d\eta^2} + k^2 c_s^2 \Theta_0 = -\frac{k^2}{3}\Psi \ . \tag{3.37}$$

In this work we assume adiabatic initial conditions, consistent with present observations (Spergel *et al.* 2003) meaning that the initial super-horizon curvature is perturbed (Ma &

Bertschinger 1995). Intuitively (White & Hu 1997), one may see that, since the background temperature redshifts as aT = constant and $a \sim t^{2/3(1+w)}$, the temperature fluctuations and the gravitational potential are linked initially by

$$\Theta = -\frac{\delta a}{a} = -\frac{2}{3(1+w)}\Psi \ . \tag{3.38}$$

One may also see that on super-horizon scales, in radiation and matter dominated eras, the gravitational potentials are constant in time. That may be seen most easily by deriving a second order equation for δ, combining (3.18) and (3.19). For vanishing anisotropic stress and isotropic perturbations only ($\pi = 0$), one may see that $\delta \propto a^2$ and a, in the radiation and matter dominated eras, respectively. By using the Poisson equation (3.16) on large scales where peculiar velocities are absent (for adiabatic initial conditions), one may be easily see indeed that the gravitational potential is constant. Such condition is violated in transition epochs, for example at equivalence between radiation and matter or matter and dark energy. The latter consideration is most important for the integrated Sachs-Wolfe effect, which we treat in the following; for our purposes here, the equality (3.38) truly represents the initial conditions for anisotropies deep in the radiation dominated era. The solution of Eq. (3.37) equation is

$$\Theta_0(\eta) = [\Theta_0(0) + m_{eff}\Psi]\cos(ks) - m_{eff}\Psi \ , \tag{3.39}$$

where $s = \int c_s d\eta$ is the sound horizon. Since in the early Universe photons are the dominant component, we can approximate the effective mass of the fluid as $m_{eff} \approx 1$; as a consequence the oscillation takes the simpler form

$$\Theta_0(\eta) = [\Theta_0(0) + \Psi]\cos(ks) - \Psi \ , \tag{3.40}$$

that represents an oscillator with the zero point, i.e. the state at which pressure and gravity are balanced, displaced by gravity. The displacement $-\Psi > 0$ yields hotter photons in the potential wells because the gravitational infall increases both the photon energy, through gravitational blueshift, and their number density. After the last scattering, the photons acquire a gravitational redshift, climbing out of the potential wells, that cancels exactly the blueshift given by $-\Psi$ yielding an effective temperature perturbation of

$$\Theta_0(\eta) + \Psi = [\Theta_0(0) + \Psi]\cos(ks) \ , \tag{3.41}$$

where the effective fluctuation is determined by the phase of the oscillation at last scattering. The temperature fluctuations present a harmonic series of peaks whose the m^{th} one is located at $k_m = m\pi/s$. Odd and even peaks represent compression and rarefaction phase inside the potential wells, respectively; the former are temperature crests, the latter are temperature troughs. Knowing that the typical size of the sound horizon at last scattering is $100h^{-1}$ Mpc, that the comoving distance at last scattering is about $6000h^{-1}$ Mpc, and using the empirical relation $l \simeq 180^o/\vartheta$ (ϑ is the angle in degrees) valid for spherical harmonics, one has that the temperature fluctuations produce acoustic oscillations in the CMB power spectrum at multipole equal and higher than 200, as we can see in Fig. 3.3. In that figure we plot the CMB power spectrum for a flat ΛCDM concordance model in which the main cosmological parameters are fixed as follows: vacuum density $\Omega_V = 0.73$, Hubble constant $h = 0.72$, baryon density $\Omega_b = 0.046$, cold dark matter density $\Omega_{cdm} = 1 - \Omega_V - \Omega_b$, reionization optical depth $\tau = 0.11$, scalar perturbations only with spectral index $n_s = 0.96$. In the matter dominated era we recover the familiar Sachs-Wolfe effect (Sachs & Wolfe 1967)

$$[\Theta_0 + \Psi] = \frac{1}{3}\Psi \ , \tag{3.42}$$

as a direct consequence of Eq. (3.38) with $w = 0$. This effect is the dominant source of anisotropies on large angular scales, responsible for the low multipole ($l < 100$) region in the CMB power spectrum. That is evident plotting the CMB power spectrum in log-linear scale (Fig. 3.3). The Sachs-Wolfe effect is a combination of an intrinsic temperature and a gravitational redshift and it gives the effective super-horizon perturbations in the photon temperature when the photons last scatter and climb out of the potential well Ψ.

We now include the effect of the baryons that contributes to the inertial and gravitational mass of the fluid m_{eff} decreasing the sound of speed and changing the balance of pressure and gravity. The gravitational infall now leads to greater compression of the fluid in a potential well displacing the zero point of the oscillation (baryon drag); this relative shift is active at last scattering enhancing all peaks from compression (odd ones) over those from rarefaction (even ones). This behavior makes the relative heights of the acoustic peaks extremely sensitive to the baryon density $\Omega_b h^2$ (see Fig. 3.3). Taking the baryon-photon

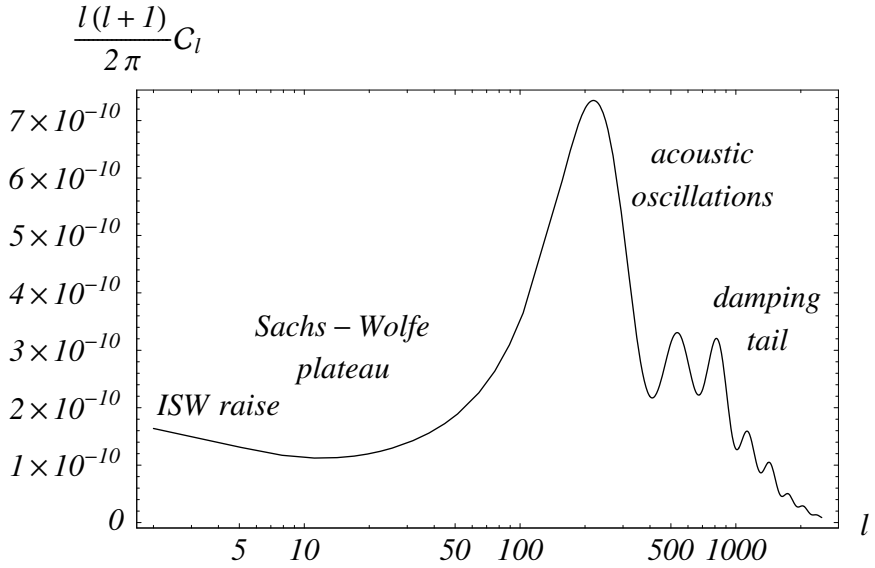

Figure 3.3: CMB power spectrum for the ΛCDM concordance model in log-linear scale. The main physical processes are listed (see text for details).

ratio constant in time, the effective temperature perturbation becomes

$$\Theta_0(\eta) + \Psi = \frac{1}{3}\Psi(1+3R)\cos(ks) - R\Psi \ , \tag{3.43}$$

where it is evident how the extra gravity provided by the baryons enhance compression into potential wells.

Since the photons possess a finite mean free path in the baryon fluid due to the Thomson scattering, photons and baryons are not perfectly coupled. Thus, as the photons random walk through the baryons, hot and cold spots are mixed. Fluctuations remain only in the unscattered fraction causing a near exponential decrease in amplitude as the diffusion length overtakes the wavelength. The result of that photon diffusion is that the acoustic oscillations are damped by a factor $\exp\left[-(k/k_D)^2\right]$ where the squared diffusion scale is given by

$$k_D^{-2} = \frac{1}{6}\int_0^\eta d\eta \left(\frac{d\tau}{d\eta}\right)^{-1} \frac{R^2 + 4(1+R)/5}{(1+R)^2} \ , \tag{3.44}$$

which is essentially the distance a photon can random walk by η (Hu & White 1997a). This process destroys the baryonic acoustic oscillations and is known as Silk damping (Silk 1968). In Figs 3.3 and 3.4 the damping tail is visible in the CMB power spectrum at multipoles higher than 1000, where the amplitude falls down.

Summarizing, we have seen how the CMB anisotropy is essentially an image of the acoustic fluctuations at last scattering modified by diffusion damping and free streamed to the present. Since inhomogeneities at the last scattering appear as anisotropies on the sky today, this can be equivalently viewed as a simple projection of the plane wave on the sphere. As we stressed above, we choose initial adiabatic perturbations, so the peak locations of the CMB power spectrum only depends on the background cosmology: the dominant factor in the peak locations is the cosmic geometry, i.e. the comoving distance to the last scattering, including contribution from all cosmological components, given their dynamics.

3.4.2 Secondary anisotropies

The secondary anisotropies can be divided in two categories: those produced by gravitational effects and those produced by scattering effects after the recombination. Compared with the primary signal, secondary anisotropies provide more details on the evolution of cosmic structures.

If metric fluctuations evolve as the photons stream through them, they leave their mark as a gravitational redshift or blueshift; this effect is known as the Integrated Sachs-Wolfe (ISW) effect and can be divided into three main contributions: early ISW (from radiation-matter transition), late ISW (from accelerating expansion at low redshifts) and Rees-Sciama effect (from sub-horizon evolution of structures, including the non-linear regime, Rees & Sciama 1968). Metric fluctuations can also lens the photons and distort the primary signal; this is the gravitational lensing effect and will be analyzed in detail in Sec. 3.5. Other gravitational effects are produced by vector and tensor perturbations (gravitational waves) or more exotic sources of metric distortions such as topological defects (Kaiser & Stebbins 1984); we do not discuss them further in this work.

The concept behind the ISW effect is that if the depth of the potential well changes as the photons cross it, the blueshift from falling in and the redshift from climbing out no longer cancel leading to a residual temperature fluctuation, or vice versa for potential peaks. An approximate solution to the Boltzmann equation (3.31), including both ordinary Sachs-

Wolfe effect and ISW, obtained assuming the recoupling as instantaneous, is given by

$$\frac{\Theta_l(k,\eta_0)}{2l+1} = [\Theta_0 + \Psi](\eta_*)\, j_l[k(\eta_0 - \eta_*)] + \int_{\eta_*}^{\eta_0} d\eta \left(\frac{d\Psi}{d\eta} - \frac{d\Phi}{d\eta}\right) j_l[k(\eta_0 - \eta)] \ , \qquad (3.45)$$

where the integral between the present η_0 and the last scattering η^* represents the ISW. As we stressed in Sec. 3.4.1, The change in the cosmic equation of state makes $d\Psi/d\eta$ and $d\Phi/d\eta$ non-vanishing in particular on super-horizon scales; this process injects power expecially on large angular scales, appearing at very low multipoles (see Fig. 3.3). The late ISW occurs in Cosmological Constant or dark energy dominated cosmologies, as the Universe starts accelerating and the rapid expansion causes the decay of the density fluctuations that drive the decay of the gravitational potentials. The early ISW is also caused by the change in the cosmic equation of state, occurring in a low matter density universe, where the radiation is still significant at decoupling. For this reason, it contributes mostly on scale corresponding to a few degrees in the sky (Hu & Sugiyama 1995a). Finally, the Rees-Sciama effect is due to the sub-horizon dynamics of cosmological structures, in particular in the non-linear regime, also leading to a change in the potential wells or peaks while CMB photons cross them. It is relevant on small scales, not comparable to the primary signal until well into the diffusion damping tail.

The light emitted during an early round of structure formation may be able to reionize all or part of the Universe (Kogut *et al.* 2003 and references therein). Re-scattering both erases primary anisotropies and generates new ones, damping fluctuations just as diffusion leaves anisotropies only in the unscattered fraction $e^{-\tau}$. The relevant scale for this process is the horizon scale at the epoch of re-scattering. On scales smaller than that, rescattering itself results in a damping of primary anisotropies.

Finally, hot clusters provide a variation in the optical depth which causes scattering of the primary CMB photons. The Doppler effect due to the peculiar velocity of the cluster yields an anisotropy known as kinematic Sunyaev-Zel'dovich (SZ) effect (Sunyaev & Zel'dovich 1972). Compton scattering of CMB photons on hot electrons also produces spectral distortions; this effect is the thermal SZ and upscatter photons to the Rayleigh-Jeans to the Wien regime leaving a clear fingerprint on the CMB spectral distribution (see Birkinshaw 1999 for a review).

3.5 CMB lensing

In this section we begin the treatment of a central topic for this work, namely the process of gravitational lensing of primordial CMB anisotropies by growing structures along the line of sight. The first part is general and will be also useful in the following, as we review the formalism necessary to compute the gravitational lensing effect on a pair of propagating photons separated by an angle θ; in the last part, we specialize and then apply such formalism in order to describe the lensing effect on the CMB angular power spectrum. As in the previous sections, our framework is defined by the metric (3.15) without anisotropic stress, leading to $\Psi = -\Phi$.

The mass concentrations along the path of photons traveling in the Universe will deflect the photon trajectory as a gravitational lens. We can evaluate the rate of change in the photon direction $\vec{s}$, as a function of the comoving path length λ along the photon geodesic, applying the photon geodesic equation to the perturbed metric (3.15) we obtain (Weinberg 1972; Schneider, Ehlers & Falco 1992)

$$\frac{d\vec{s}}{d\lambda} = 2\vec{s} \times \left(\vec{s} \times \vec{\nabla}\Psi\right) \equiv -2\vec{\nabla}_{\perp}\Psi \ , \tag{3.46}$$

where $\vec{\nabla}_{\perp}\Psi$ is the derivative of the gravitational potential, transverse to the line of sight. The gradient of the gravitational potential can be viewed as a force deflecting the photons while they propagate through the unperturbed spacetime. Because the only observable photon direction is that at the observer position, it is convenient to propagate photons backward in time (i.e. relatively to their final direction). Therefore, the total deflection angle between the photon source at last scattering surface and the observer is given by

$$\vec{\xi} = -2\int_0^{r_{ls}} dr \vec{\nabla}_{\perp}\Psi \ ; \tag{3.47}$$

similarly, the photon angular excursion relative to its observed value, propagated backward to the last scattering, is given by

$$\vec{\alpha} = -2\int_0^{r_{ls}} dr \frac{r_{ls} - r}{r_{ls} r} \vec{\nabla}_{\perp}\Psi \ , \tag{3.48}$$

where the factor depending on the distances takes into account the geometry of the lens-source system (Schneider, Ehlers & Falco 1992; Bartelmann & Schneider 2001); in our

case the last scattering surface is the source plane located at r_{ls}, while the (infinitesimal) deflection plane is located at r, and since we assumed a flat space the distance between the source plane and the deflection plane is simply their difference. Finally the global effect due to the lensing is simply the integral between the source and the observer. Since we are interested in the angular excursion of a photon on the CMB and not in the absolute change in its direction, the relevant quantity for our discussion is $\vec{\alpha}$.

Two photons observed with an angular separation θ have a different angular separation when emitted from the source position. Its mean is equal to the unperturbed value while the dispersion is given by (Seljak 1994)

$$\sigma(\theta) = \left[\frac{1}{2}\left\langle(\vec{\alpha}_1 - \vec{\alpha}_2)^2\right\rangle\right]^{1/2} = [C_{GL}(0) - C_{GL}(\theta)]^{1/2} \ , \tag{3.49}$$

where brackets denotes the ensemble average performed over all the pairs of photons with a fixed observed angular separation θ. The quantity $C_{GL}(\theta)$ is the correlation function of the gravitational lensing, which contains the contribution of the gravitational potential perturbations, encoded in (3.48). It is defined as

$$C_{GL}(\theta) = 16\pi^2 \int dk k^3 \int dr \left(\frac{r_{ls} - r}{r_{ls} r}\right)^2 J_0(k\theta r) P_\Psi(k, \eta)|_{\eta=\eta_0 - r} \ , \tag{3.50}$$

where $J_0(x)$ is the Bessel function of order zero and $P_\Psi(k, \eta)$ is the power spectrum of the potential; the latter is usually defined assuming Gaussianity:

$$\left\langle \Psi\left(\vec{k}, \eta\right) \Psi^*\left(\vec{k}, \eta\right)\right\rangle = P_\Psi(k, \eta)\delta^3\left(\vec{k} - \vec{k'}\right) \ . \tag{3.51}$$

Basically Eq. (3.50) is the Fourier expansion of the ensemble average of Eq. (3.48) and its derivation is based on the Limber equation in Fourier space (see e.g. Kaiser 1992), in which it is assumed that the dominant scales contributing to the dispersion are much smaller than the photon travel distance; this condition is satisfied for sources at cosmological distances. We discuss the Limber approximation in detail in the next chapter. No assumption on the power spectrum has been made, so that Eq. (3.50) can be used both in the linear and in the non-linear regime of density perturbations, provided that the Gaussianity is maintained.

The evaluation of the gravitational lensing effect on the CMB is simplified and more intuitive if only small angular scales are considered and if the fluctuations in relative

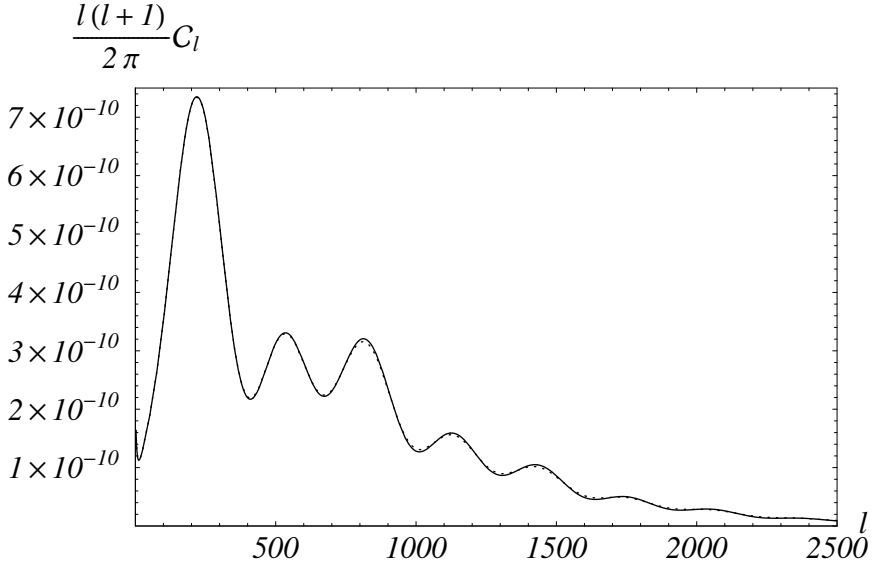

Figure 3.4: CMB power spectrum for the ΛCDM concordance model. The solid line represents the case without lensing effect while the dotted line is with lensing effect.

separation between the two photons can be considered Gaussian. This assumption should limit the validity of the calculation to the linear scales only, where the prediction of most models that initial fluctuations are Gaussian makes its validity reliable. In reality it is valid up to the quasi-linear regime, because the relative fluctuations are obtained by a projection of a three-dimensional distribution over a broad radial window function and are in general more Gaussian than the three-dimensional distribution of the gravitational potential itself (Bartelmann & Schneider 2001).

Let us now focus on the modification induced by lensing on the CMB anisotropy temperature power spectrum. With the approximation shown above, we can write the temperature anisotropies in terms of its two dimensional transform in the Fourier space:

$$\Theta\left(\vec{\theta}\right) = \int d^2\vec{l} e^{-i\vec{l}\cdot\vec{\theta}} \Theta\left(\vec{l}\right) \ . \tag{3.52}$$

Defining $\vec{\theta}_1$ and $\vec{\theta}_2$ the unlensed positions of the two photons, the correlation function including lensing is given by

$$\begin{aligned} \widetilde{C}(\theta) &= \left\langle \Theta\left(\vec{\theta}_1 + \vec{\alpha}_1\right) \Theta\left(\vec{\theta}_2 + \vec{\alpha}_2\right) \right\rangle_{\vec{\theta}_1\cdot\vec{\theta}_2 = \cos\theta} = \\ &= \int d^2\vec{l} \int d^2\vec{l}' e^{-i\vec{l}\cdot\vec{\theta}_1 + \vec{l}'\cdot\vec{\theta}_2} \left\langle e^{-i\vec{l}\cdot\vec{\alpha}_1 + i\vec{l}'\cdot\vec{\alpha}_2} \Theta\left(\vec{l}\right) \Theta\left(\vec{l}'\right) \right\rangle \ . \end{aligned} \tag{3.53}$$

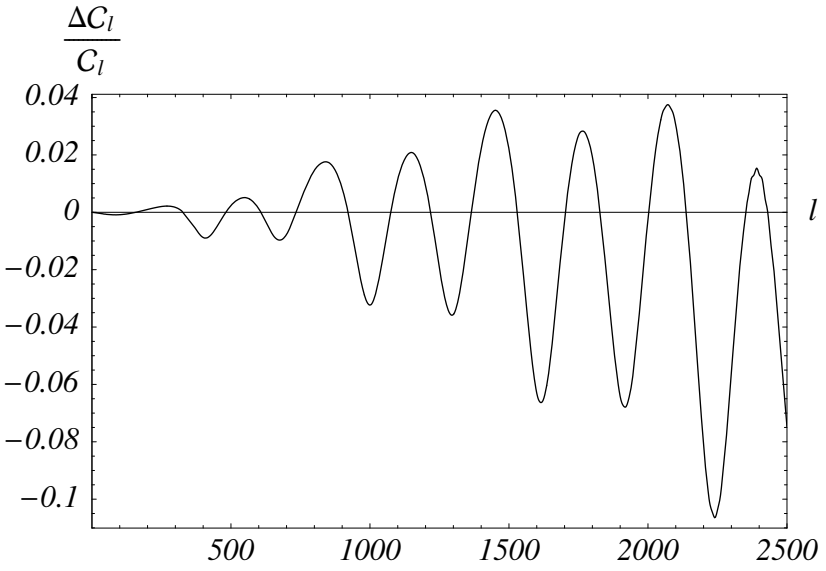

Figure 3.5: Relative amplitude $\Delta C_l/C_l$ for the ΛCDM concordance model.

In the previous equation we have to average over the intrinsic temperature anisotropies $\Theta\left(\vec{l}\right)$, exploiting the Gaussian CMB statistics in the two dimensional Fourier transform form:

$$\left\langle \Theta\left(\vec{l}\right)\Theta\left(\vec{l'}\right)\right\rangle = \frac{\delta^2\left(\vec{l}-\vec{l'}\right)}{(2\pi)^2}C_l \ . \tag{3.54}$$

We also average over the lensing fluctuations $\vec{\alpha}$, giving the characteristic function of a Gaussian field

$$\left\langle \exp\left[-i\vec{l}\cdot\left(\vec{\alpha}_1-\vec{\alpha}_2\right)\right]\right\rangle = \exp\left[-\frac{1}{2}\left\langle\left[\vec{l}\cdot\left(\vec{\alpha}_1-\vec{\alpha}_2\right)\right]^2\right\rangle\right] \ . \tag{3.55}$$

Using (3.49), we get the lensed correlation function

$$\widetilde{C}(\theta) = \frac{1}{(2\pi)^2}\int_0^\infty ldlC_l\int_0^{2\pi}d\varphi_l \exp\left\{-\frac{l^2}{2}\left[\sigma^2(\theta)-C_{GL,2}(\theta)\cos 2\varphi_l\right]-il\cos\varphi_l\right\} \ , \tag{3.56}$$

where $C_{GL,2}$ is obtained from (3.50) by replacing the Bessel function of order 0 with that of order 2. Assuming $l^2C_{GL,2} \ll 1$, which corresponds to the small deflection limit, we can expand in Taylor series the exponential of previous equation, keeping only the first term $J_0(l\theta)$, and integrating over the angle φ_l; this leads to

$$\widetilde{C}(\theta) = \frac{1}{2\pi}\int_0^\infty ldle^{-\frac{1}{2}l^2\sigma^2(\theta)}C_lJ_0(l\theta) \ . \tag{3.57}$$

The lensing effect in terms of the CMB power spectrum is given by

$$\widetilde{C}_l = \int_0^\pi \theta d\theta \int_0^\infty l' dl' e^{-\frac{1}{2}l'^2\sigma^2(\theta)} C_{l'} J_0(l'\theta) J_0(l\theta) \ , \tag{3.58}$$

and can be simplified additionally assuming $\epsilon = \sigma(\theta)/\theta$ to be constant or slowly changing with θ and small, obtaining

$$\widetilde{C}_l = \int_0^\infty \frac{l' dl'}{(\epsilon l')^2} C_{l'} I_0\left(\frac{l}{\epsilon^2 l'}\right) \exp\left[\frac{l^2 + l'^2}{2(\epsilon l')^2}\right] \ , \tag{3.59}$$

in which $I_0(x)$ is the modified Bessel function of order zero. In order to understand the lensing effect on the CMB power spectrum we need to use $l \approx l'$ everywhere except in the exponential and assume $\epsilon \ll 1$ to asymptotically expand $I_0(x)$. In this limit we have

$$\widetilde{C}_l = \frac{1}{\sqrt{2\pi}\epsilon} \int_0^\infty \frac{dl'}{l'} C_{l'} \exp\left[-\frac{(l-l')^2}{2(\epsilon l')^2}\right] \ . \tag{3.60}$$

Eq. (3.60) tells us that the effect of gravitational lensing on the CMB angular power spectrum is essentially a smoothing of the power spectrum with a Gaussian of relative width ϵ. Fig. 3.4 shows the lensing effect on the CMB power spectrum for the ΛCDM concordance model. The lensing induces a modest change in the power spectrum: indeed the lensed and unlensed spectra are indistinguishable on large scales (small multipoles). The peaks of acoustic oscillations are smoothed accordingly to (3.60). This is because $\sigma(\theta)/\theta$ is an increasing function of the multipole (Seljak 1996a) and because the relative width of the oscillations becomes narrower toward the smaller angular scales. The influence of the lensing on the CMB power spectrum is more evident in Fig. 3.5 where we plot the relative amplitude between the lensed and the unlensed power spectra $\Delta C_l/C_l = \left(C_l - C_l^{lens}\right)/C_l$; as we can see the effect is relevant at very high multipoles while it is practically null at low multipoles.

Of course the lensing does not affect the power spectrum only. Actually it re-maps the primordial anisotropies, injecting a non-Gaussian pattern in them, as it will becomes clear in the rest of this work. Such non-Gaussian pattern has an impact already at the level of the CMB three point statistics. We shall now study in detail the harmonic transform of the three point correlation function when lensing effect and ISW are taken into account, getting closer to the subject of the present work.

Chapter 4

CMB three point correlation function and gravitational lensing

In this chapter we expand the analysis of the lensing effect on the CMB anisotropies, by studying how it affects the overall CMB statistics, indeed injecting power where the primary anisotropy are expected to yield a null contribution within cosmic variance, i.e. the non-Gaussian distortion of the primary image. As another, most important ingredient for our purposes, we shall see how the power injection is actually non-vanishing only at the epoch of the onset of cosmic acceleration, overlapping with structure formation, being null earlier and at present. Such non-Gaussian power injection is actually already evident at the level of the three-point correlation function. Technically, it is caused by the correlation between the lensing and the ISW effects on the CMB temperature anisotropies. We will focus on the harmonic expression of the three point correlation function, namely the bispectrum, studying its geometrical properties. Throughout the discussion we adopt a flat ΛCDM model as reference cosmology in which the main cosmological parameters are fixed as follows: vacuum density $\Omega_V = 0.73$, Hubble constant $h = 0.72$, baryon density $\Omega_b = 0.046$, cold dark matter density $\Omega_{CDM} = 1 - \Omega_V - \Omega_b$, reionization optical depth $\tau = 0.11$, three massless neutrino species, scalar perturbations only with spectral index $n_s = 0.96$. In Sec. 4.1 we describe the ISW and its correlation with the lensing; in Sec. 4.2 we compute the three point statistics in the harmonic domain generated by that correlation, pointing out

the computational challenges for its evaluation; Sec. 4.3 contains a full geometrical analysis of the bispectrum.

4.1 ISW and lensing correlation

We wish to study the distortion induced on the CMB anisotropies by the gravitational lensing and its correlation with the ISW; we take into account also the Rees-Sciama effect, and specifically the ISW caused by the dynamics of non-linear density fluctuations along the photon path (Rees & Sciama 1968). As we discussed in the previous chapter, the gravitational lensing produces a deflection of CMB photons: in a direction $\hat{n}$ in the sky we see the anisotropy originally scattered on a different one, $\hat{n} + \vec{\alpha}$, where $\vec{\alpha}$ is the deflection angle. The ISW effect is a redshift or a blueshift of the CMB photons when they pass through the potential perturbations of evolving structures. When they fall in overdensities, the photons gain energy (gravitational blueshift) and when they climb back out, they are redshifted, or vice-versa for underdensities. The process is not balanced because the structure is evolving and its potential perturbation gets steeper or shallower when the photons propagate through it.

Taking into account only the two effects described above, we can decompose the CMB anisotropy in a direction $\hat{n}$ in the sky as

$$\Theta(\hat{n}) = \Theta_P(\hat{n} + \vec{\alpha}) + \Theta_{ISW}(\hat{n}) \ , \tag{4.1}$$

where the first term represents the primordial CMB anisotropy at decoupling, which was last scattered on a direction $\hat{n} + \vec{\alpha}$ and gravitationally lensed to our line of sight $\hat{n}$, whereas the second term is the CMB anisotropy contribution from the ISW effect. We assume that the primordial anisotropies are Gaussian, so the lensing and ISW effects are the only sources of non-Gaussianity. Expanding Eq. (4.1) to the first order in $\vec{\alpha}$ we obtain

$$\Theta(\hat{n}) \simeq \Theta_P(\hat{n}) + \Theta_{ISW}(\hat{n}) + \vec{\nabla}\Theta_P(\hat{n}) \cdot \vec{\alpha} \ . \tag{4.2}$$

Now we analyze each contribution to Eq. (4.2) in terms of physical quantities. As before we work in the conformal Newtonian gauge, and we include only scalars, assuming no

anisotropic stress. The line element is $ds^2 = a^2\left[-(1-2\Psi)dt^2 + (1-2\Psi)dx^i dx_i\right]$ where Ψ is the only relevant gravitational potential if the anisotropic stress is zero. Since the CMB anisotropies are sourced by the gravitational potential, and assuming an instantaneous decoupling, the primordial contribution to the anisotropy $\Theta(\hat{n})$ can be written as

$$\Theta_P(\hat{n}) = \int \frac{d^3k}{(2\pi)^3} \exp\left(i\vec{k}\cdot\hat{n}r_{ls}\right) \Psi\left(\vec{k}\right) T_R(k) \ , \tag{4.3}$$

where $\Psi\left(\vec{k}\right)$ made the dependence of Ψ from $\vec{k}$ explicit, and r_{ls} is the conformal distance to the last scattering surface. $T_R(k)$ is the radiation transfer function modifying the primordial power spectrum to take into account the super-horizon and sub-horizon dynamics: in the previous chapter we saw how for adiabatic initial conditions, the primordial temperature fluctuation Θ encodes the initial spectrum of the fluctuations in the gravitational potential, and how a hierarchical series of differential equations propagate that power on different scales. $T_R(k)$, which can be evaluated numerically, takes into account the corresponding transfer of the initial power from super-horizon to sub-horizon scales. Its role is totally analogous to the transfer function for the matter power spectrum, to be discussed next. For simplicity, all quantities in (4.3) are evaluated at decoupling.

Taking into account the time variation of the gravitational potential along the line of sight, the ISW effect can be expressed as (Sachs & Wolfe 1967; Martinez-Gonzalez, Sanz & Silk 1990; Seljak 1996)

$$\Theta_{ISW}(\hat{n}) = 2\int_0^{r_{ls}} dr \frac{\partial}{\partial\eta}\Psi(\eta, \hat{n}r) \ , \tag{4.4}$$

where η is the conformal time, coinciding with r if the geometry is flat. Note that the above relation is another form of the last term in Eq. (3.45), where the harmonic expansion was exploited. The deflection angle $\vec{\alpha}$ is responsible for the gravitational lensing effect and is defined as the gradient on the angular coordinates of the lensing potential $\phi(\hat{n})$ (Schneider, Ehlers & Falco 1992; Bartelmann & Schneider 2001):

$$\vec{\alpha} = \vec{\nabla}_\perp \phi(\hat{n}) \ . \tag{4.5}$$

As we saw in the previous chapter, the lensing potential is simply the projection of the gravitational potential along the line of sight, this can be written as (Kaiser 1998):

$$\phi(\hat{n}) = -2\int_0^{r_{ls}} dr \frac{r_{ls}-r}{r_{ls}r}\Psi(r, \hat{n}r) \ . \tag{4.6}$$

Let us now specify better the density perturbations, powering the gravitational potential fluctuations and therefore the whole lensing process. The gravitational potential Ψ is built out of the density fluctuations through the Poisson equation and the linear power spectrum is defined as usual as

$$P_L(k,z) = Ak^{n_s}T_M^2(k,z) \ , \tag{4.7}$$

where A represents the primordial perturbation amplitude and $T_M(k,z)$ is the matter transfer function. As for radiation, the latter describes, at each z, how the primordial power is transferred on the scale k, which may or may not have crossed the horizon. To describe the non-linear behavior of density perturbations, we use a semi-analytical approach (Ma 1998) consisting essentially of a re-mapping and rescaling of the linear one; the linear power spectrum $P_L(k,z)$ is computed at the wavenumber

$$k_L = \frac{k}{\left[1+4\pi k^3 P_{NL}(k,z)\right]^{1/3}} \ , \tag{4.8}$$

and is related to the non-linear one $P_{NL}(k,z)$ via the empirical formula

$$P_{NL}(k,z) = G\left[\frac{4\pi k^3 P_L(k,z)}{f^{3/2}\sigma_8^{\beta}(z)}, z\right]\left(\frac{k_L}{k}\right)^3 P_L(k_L,z) \ , \tag{4.9}$$

where σ_8 is the normalization of the matter power spectrum on cluster scales, $\beta = 0.83$, $f = g_0$ for the ΛCDM model considered here (Ma 1998) and G is defined as

$$G(x,z) = \frac{\left[1+\ln(1+x/2)\right]\left[1+0.02x^4+1.08\cdot 10^{-4}x^8/g(z)\right]}{1+2.1\cdot 10^{-5}x^{15/2}} \ ; \tag{4.10}$$

$g(z)$ is the perturbation growth rate defined by the matter transfer function on small scales as

$$g(z) = g_0(1+z)\frac{T_M(k\to 0,z)}{T_M(k\to 0,0)} \ , \tag{4.11}$$

where g_0 is the present value of the growth factor. As we shall see in Ch. 6, the linear growth factor $g(z)$ is a key ingredient for our purposes; it is plotted in Fig. 4.1 for the present cosmology. Note how at high redshifts, i.e. in the radiation dominated era, $g(z)$ gets proportional to $a = 1/(1+z)$, as discussed in the previous chapter. The decrease at low redshifts is due to the dominance of the Cosmological Constant, slowing down the

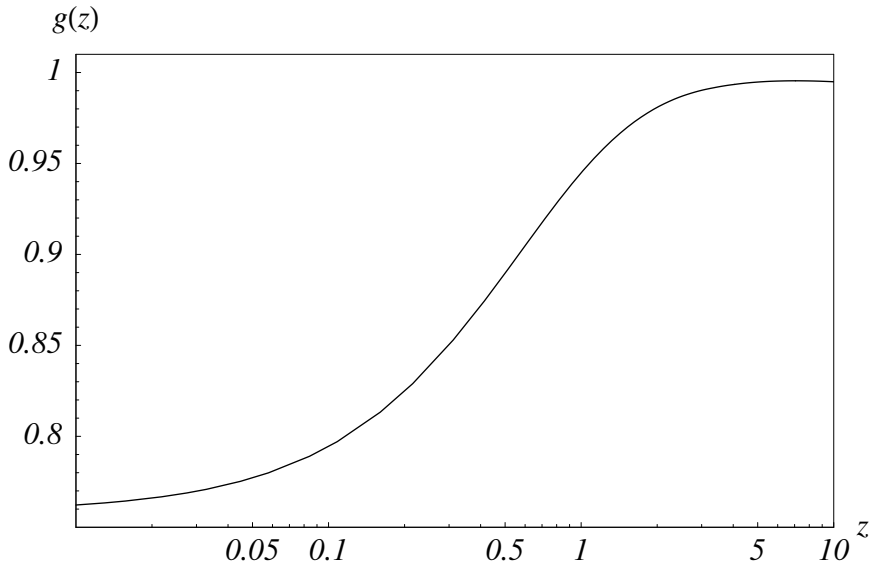

Figure 4.1: Growth factor $g(z)$ for our ΛCDM model normalized to unity on the last scattering surface.

perturbation growth. To compute $P_{NL}(k,z)$ we must solve numerically an implicit equation, represented by Eq. (4.8) and Eq. (4.9), at any epoch z and for any wavenumber k. In Fig. 4.2 we plot the matter power spectra $P_L(k,z)$ and $P_{NL}(k,z)$ for the cosmology considered here; as we can see, the non-linearity produces a bump in the matter power spectrum around $k = 0.5$ Mpc^{-1} at $z = 0$ increasing the power at higher wavenumber (smaller scales). At higher redshift the non-linear contribution becomes smaller and the wavenumber at which the non-linearity starts moves towards higher values, as expected.

We now expand the observed CMB fluctuation of Eq. (4.2) in spherical harmonics:

$$a_{lm} = \int d\Omega_{\hat{n}} \left[\Theta_P(\hat{n}) + \Theta_{ISW}(\hat{n}) + \vec{\nabla}\Theta_P(\hat{n}) \cdot \vec{\alpha} \right] Y^*_{lm} \ . \tag{4.12}$$

The first and the second terms clearly are the coefficients of the harmonic expansion of the primordial and secondary anisotropy, respectively, while the third one represents the lensing effect. Using Eq. (4.5), the lensing contribution may be written as

$$\begin{aligned} &\int d\Omega_{\hat{n}} \left(\vec{\nabla}\Theta_P \cdot \vec{\nabla}_\perp \phi \right) Y^*_{lm} = \\ &= \int d\Omega_{\hat{n}} \left[\vec{\nabla} \sum_{l'm'} \left(a^P_{l'm'} \right)^* Y^*_{l'm'} \right] \cdot \left[\vec{\nabla} \sum_{l''m''} \left(a^{lens}_{l''m''} \right)^* Y^*_{l''m''} \right] Y^*_{lm} \ , \end{aligned} \tag{4.13}$$

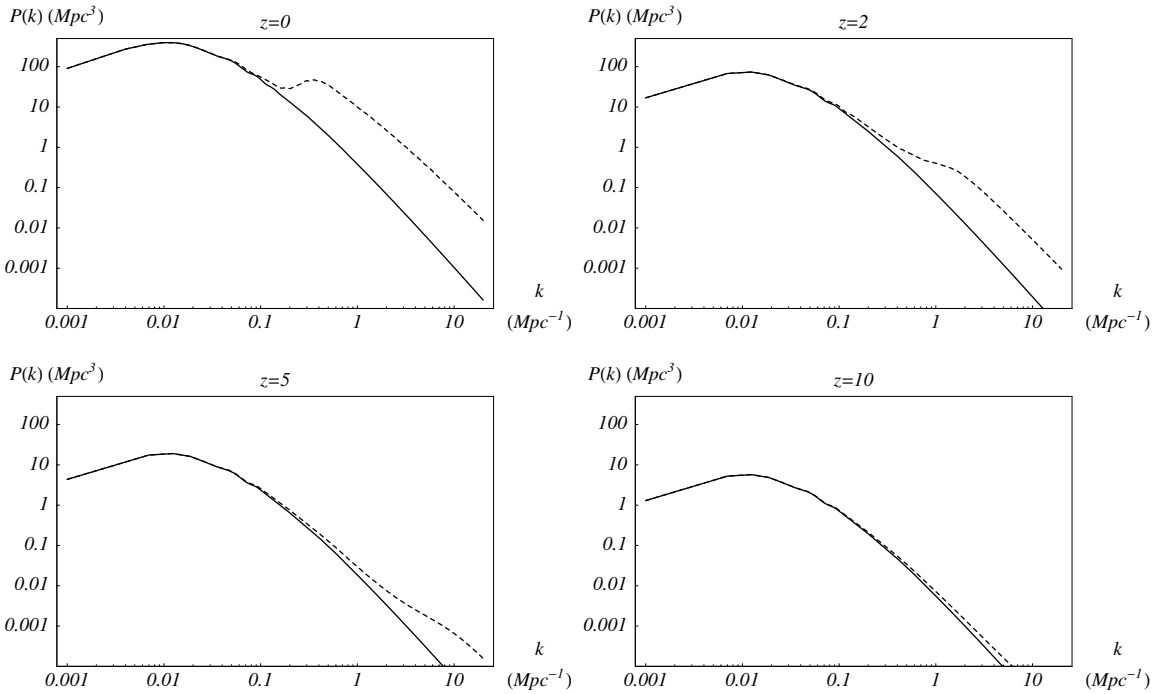

Figure 4.2: Matter power spectra $P_L(k,z)$ (solid line) and $P_{NL}(k,z)$ (dashed line) at different redshifts as function of k.

where we have expanded both the primordial contribution and the lensing one in spherical harmonics, independently. Exchanging the sums with the integral we can rewrite the right hand side of the equation above in the form

$$\sum_{l'm'}\sum_{l''m''}(-1)^{m+m'+m''}\left(\int d\Omega_{\hat{n}}\vec{\nabla}Y_{l'm'}\cdot\vec{\nabla}Y_{l''m''}Y_{l-m}\right)\left(a^{P}_{l'm'}\right)^{*}\left(a^{lens}_{l''m''}\right)^{*}\ , \tag{4.14}$$

where we applied the identity $Y^{*}_{lm}=(-1)^{m}Y_{l-m}$. Integrating by parts one gets

$$\begin{aligned}&\int d\Omega_{\hat{n}}\nabla^2 Y_{l'm'}Y_{l''m''}Y_{l-m}=\\&-\int d^2\hat{n}\vec{\nabla}Y_{l'm'}\cdot\vec{\nabla}Y_{l''m''}Y_{l-m}-\int d\Omega_{\hat{n}}\vec{\nabla}Y_{l'm'}\cdot\vec{\nabla}Y_{l-m}Y_{l''m''}\ ,\end{aligned} \tag{4.15}$$

and using the eigenvalues equation for the spherical harmonics $\nabla^2 Y_{lm}=l(l+1)Y_{lm}$, Eq. (4.14) becomes

$$\sum_{l'm'}\sum_{l''m''}(-1)^{m+m'+m''}\frac{l'(l'+1)-l(l+1)+l''(l''+1)}{2}G^{-m\,m'\,m''}_{l\,l'\,l''}\left(a^{P}_{l'm'}\right)^{*}\left(a^{lens}_{l''m''}\right)^{*}\ , \tag{4.16}$$

where the Gaunt's integral $G_{l\,l'\,l''}^{-m\,m'\,m''}$ is defined as

$$G_{l_1 l_2 l_3}^{m_1 m_2 m_3} = \int d^2\hat{n} Y_{l_1 m_1}(\hat{n}) Y_{l_2 m_2}(\hat{n}) Y_{l_3 m_3}(\hat{n}) = \\ = \sqrt{\frac{(2l_1+1)(2l_2+1)(2l_3+1)}{4\pi}} \begin{pmatrix} l_1 & l_2 & l_3 \\ 0 & 0 & 0 \end{pmatrix} \begin{pmatrix} l_1 & l_2 & l_3 \\ m_1 & m_2 & m_3 \end{pmatrix}. \quad (4.17)$$

The parenthesis are the Wigner's 3J symbols (see Sec. 4.2.2 and Appendix A), finally we are able to write the full harmonic expansion of Eq. (4.2):

$$a_{lm} = a_{lm}^P + a_{lm}^{ISW} + \sum_{l'm'} \sum_{l''m''} (-1)^{m+m'+m''} G_{l\,l'\,l''}^{-m\,m'\,m''} \cdot \\ \cdot \frac{l'(l'+1) - l(l+1) + l''(l''+1)}{2} \left(a_{l'm'}^P\right)^* \left(a_{l''m''}^{lens}\right)^* . \quad (4.18)$$

We clearly see three contributions to (4.18): the primordial one $\left(a_{lm}^P\right)$, the ISW one $\left(a_{lm}^{ISW}\right)$ and the product between the primordial one and the lensing one $\left(a_{lm}^{lens}\right)$. As we shall see in the next section, the correlation between lensing and ISW induces a non-vanishing bispectrum power.

4.2 The three point statistics in the harmonic domain and Wigner's 3J symbols

We divide this section in two subsections. In the first we write the relevant algebra to describe the CMB bispectrum, and discuss the power injection from lensing; in the second one we show how to calculate the Wigner's 3J symbols, a necessary ingredients in these computations, as we shall see.

4.2.1 CMB bispectrum induced by lensing and ISW correlation

The CMB power spectrum contains all the statistical information about the CMB anisotropies *only* if the a_{lm} are Gaussianly distributed. Here we study the non-Gaussianity due to weak lensing and ISW correlation on the CMB anisotropies assuming that the primordial ones are Gaussian. The non-Gaussianity arises when evolving structures correlate the CMB photons between the last scattering surface and us: the photons are deflected

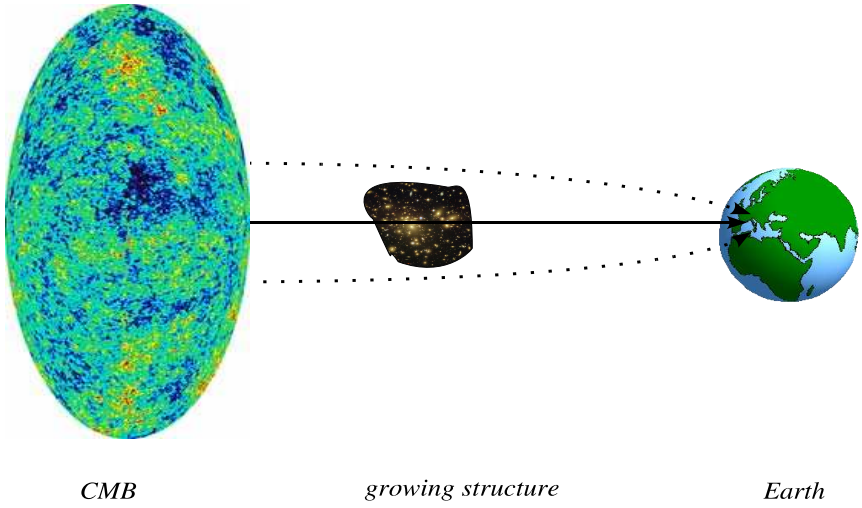

Figure 4.3: A structure between the last scattering surface and us correlates the CMB anisotropy via the ISW effect (solid line) and the lensing effect (dashed line).

by the gravitational lensing when they pass nearby density perturbation whereas the same structure redshifts or blueshifts them via the ISW (see Fig. 4.3). Because of the corresponding correlation, the CMB fluctuations acquire a non-Gaussian pattern which may be described in terms of higher order statistics in the anisotropies.

The bispectrum is the harmonic transform of the three point correlation function and it is defined as

$$B_{l_1 l_2 l_3}^{m_1 m_2 m_3} = \langle a_{l_1 m_1} a_{l_2 m_2} a_{l_3 m_3} \rangle \ , \tag{4.19}$$

where a_{lm} are the coefficients of the expansion of the total intensity CMB fluctuations and we average over all the possible realization according to the CMB statistics. With the bispectrum we probe the harmonic space with triangles: the triplet (l_1, l_2, l_3) give us the triangle configuration, i.e. its shape, while the triplet (m_1, m_2, m_3) represents the triangle orientation, i.e. how it is oriented in the l-space. For a universe which is isotropic on average, the ensemble averaged bispectrum does not depend on the triangle's orientation but only on its configuration. With these considerations we can build the angle averaged

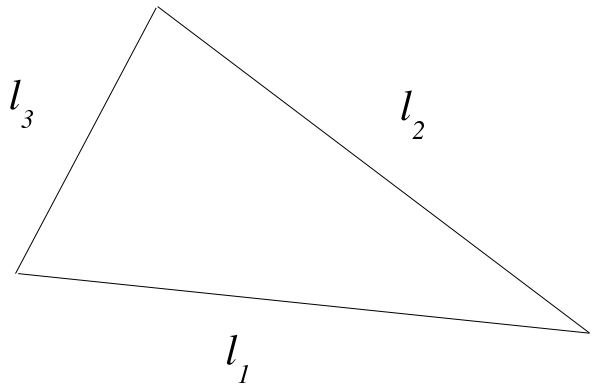

Figure 4.4: Configuration of the angular bispectrum in the l-space: the bispectrum may be thought to probe the harmonic space with triangles with sides given by l_1, l_2 and l_3.

bispectrum

$$B_{l_1 l_2 l_3} = \sum_{m_1 m_2 m_3} \begin{pmatrix} l_1 & l_2 & l_3 \\ m_1 & m_2 & m_3 \end{pmatrix} B_{l_1 l_2 l_3}^{m_1 m_2 m_3} \ , \tag{4.20}$$

summing over m; the Wigner's 3J symbols transform the m indeces under a rotation preserving the triangle configuration (see Appendix B). Since l_1, l_2 and l_3 form a triangle and the angular correlation function is invariant under parity, the three multipoles must satisfy the triangularity condition $|l_i - l_j| \leq l_k \leq l_i + l_j$ (for all permutation of indices) and $l_i + l_j + l_k =$ even; if one of these two conditions is not satisfied the bispectrum is zero. An example of triangular configuration is plotted in Fig. 4.4. After some algebra, substituting Eq. (4.18) into Eq. (4.19) we obtain

$$B_{l_1 l_2 l_3}^{m_1 m_2 m_3} = G_{l_1\, l_2\, l_3}^{m_1\, m_2\, m_3} \frac{l_1(l_1+1) - l_2(l_2+1) + l_3(l_3+1)}{2} C_{l_1}^P Q_{l_3} + 5P \ , \tag{4.21}$$

where $C_{l_1}^P$ is the primordial power spectrum, Q_{l_3} encodes the correlation between lensing and ISW effect as we specify later and $5P$ means permutations over the three multipoles. In writing Eq. (4.21) we have neglected the correlation between the primordial anisotropies and those arising from the ISW. From this consideration and from our assumption of Gaussianity of the primordial anisotropies, the only terms that survive to the average are those involving the primordial power spectrum C_l, the ISW a_{lm}^{ISW} and the lensing $\left(a_{l''m''}^{lens}\right)^*$. Substituting Eq. (4.21) into the expression of the angle averaged bispectrum (4.20) and using

the orthogonality relation of the 3J symbols (see. Appendix A), we obtain:

$$B_{l_1 l_2 l_3} = \sqrt{\frac{(2l_1+1)(2l_2+1)(2l_3+1)}{4\pi}} \begin{pmatrix} l_1 & l_2 & l_3 \\ 0 & 0 & 0 \end{pmatrix} \cdot \\ \cdot \frac{l_1(l_1+1) - l_2(l_2+1) + l_3(l_3+1)}{2} C_{l_1}^P Q_{l_3} + 5P \ . \tag{4.22}$$

In the following we shall concentrate on the angle averaged bispectrum; hereafter we will refer to Eq. (4.22) simply as bispectrum. To derive the expression of Q_l we start from

$$\left\langle \left(a_{l_1 m_1}^{lens}\right)^* a_{l_2 m_2}^{ISW} \right\rangle = -4 \left\langle \int d\Omega_{\hat{n}_1} d\Omega_{\hat{n}_2} \int dr \frac{r_{ls}-r}{r_{ls} r} \Psi(r, \hat{n}_1 r) \cdot \right. \\ \left. \cdot \int d\eta \frac{\partial \Psi(\eta, \hat{n}_1 r)}{\partial \eta} Y_{l_1 m_1}^*(\hat{n}_1) Y_{l_2 m_2}(\hat{n}_1) \right\rangle \ ; \tag{4.23}$$

expanding the gravitational potential Ψ in terms of its Fourier modes and using the Rayleigh expansion $\exp\left(\vec{k}\cdot\hat{n}r\right) = 4\pi \sum_{lm} i^l Y_{lm}^*(\hat{k}) Y_{lm}(\hat{n}) j_l(kr)$ for the exponentials ($\hat{k}$ is the direction in the Fourier space and $j_l(kr)$ are the spherical Bessel functions), we obtain

$$\left\langle \left(a_{l_1 m_1}^{lens}\right)^* a_{l_2 m_2}^{ISW} \right\rangle = -4(4\pi)^2 \int d\Omega_{\hat{n}_1} d\Omega_{\hat{n}_2} \int dr \frac{r_{ls}-r}{r_{ls} r} \int d\eta \cdot \\ \cdot \int \frac{d^3k}{(2\pi)^3} \int \frac{d^3k'}{(2\pi)^3} \left\langle \Psi\left(\vec{k}, r\right) \frac{\partial \Psi\left(\vec{k}', \eta\right)}{\partial \eta} \right\rangle j_{l'}(kr) j_{l''}(k'\eta) \cdot \\ \cdot i^{l'+l''} Y_{l'm'}^*(\hat{k}) Y_{l'm'}(\hat{n}_1) Y_{l''m''}^*(\hat{k}') Y_{l''m''}(\hat{n}_2) Y_{l_1 m_1}^*(\hat{n}_1) Y_{l_2 m_2}(\hat{n}_2) \ . \tag{4.24}$$

Using the identity $dk^3 = k^2 dk d\Omega_k$, and integrating over $d\Omega_{\hat{n}_1}$, $d\Omega_{\hat{n}_2}$ and $d\Omega_{\hat{k}}$ we have

$$\left\langle \left(a_{l_1 m_1}^{lens}\right)^* a_{l_2 m_2}^{ISW} \right\rangle = -4(4\pi)^2 \int dr \frac{r_{ls}-r}{r_{ls} r} \int d\eta \cdot \\ \cdot \int \frac{k^2 dk}{(2\pi)^3} \int \frac{k'^2 dk'}{(2\pi)^3} \left\langle \Psi(k, r) \frac{\partial \Psi(k', \eta)}{\partial \eta} \right\rangle j_{l'}(kr) j_{l''}(k'\eta) \ , \tag{4.25}$$

where we applied the orthogonality relation of spherical harmonics. We introduce now the Limber approximation (see Afshordi, Loh & Strauss 2004 for reviews), in which the spherical Bessel functions are replaced by the relation

$$j_l(x) = \sqrt{\frac{\pi}{2l+1}} \left[\delta\left(l + \frac{1}{2} - x\right) + \Delta_l \right] \ , \tag{4.26}$$

where δ is the Dirac's delta and Δ_l goes as l^{-2}. In the following we neglect Δ_l in order to simplify the evaluation of the bispectrum; the error made on the Q_l quantities to this

approximation is about 1% at $l = 10$ and falls down as l^{-1} (Giovi, Baccigalupi & Perrotta 2005). Under the assumption of Gaussian statistics, we define

$$\frac{2}{(2\pi)^3}\left\langle \Psi(k,r)\frac{\partial\Psi(k',r)}{\partial r}\right\rangle = \frac{\partial P_\Psi(k,r)}{\partial r}\delta(k-k')\ ; \tag{4.27}$$

performing now the integrals in η, k and k' and integrating in z instead of r the cross-power becomes

$$Q_l \equiv \left\langle \left(a_{lm}^{lens}\right)^* a_{lm}^{ISW}\right\rangle \simeq 2\int_0^{z_{ls}} dz \frac{r\left(z_{ls}\right)-r(z)}{r\left(z_{ls}\right)r^3(z)}\left[\frac{\partial P_\Psi(k,z)}{\partial z}\right]_{k=\frac{l+1/2}{r(z)}}\ , \tag{4.28}$$

in which $P_\Psi(k,z)$ is the power spectrum of the gravitational potential related to the matter power spectrum (Sugiyama 1995; Hu 2000; Verde & Spergel 2002) by the relation

$$P_\Psi(k,z) = \left(\frac{3}{2}\Omega_m\right)^2\left(\frac{H_0}{k}\right)^4 P(k,z)(1+z)^2\ . \tag{4.29}$$

In Eq. (4.28) the redshift derivative of $P_\Psi(k,z)$ has to be evaluated at the wavenumber $k = (l+1/2)/r(z)$ where the the left hand side represents the scale entering the non-linear regime at the epoch represented by z, while the right hand side is purely geometric. In the matter power spectrum we may take into account both the linear and the non-linear growth described by Eq. (4.9). We want to stress that the integrand of (4.28) is made by a product of a geometrical factor $R(z)$, which depends on cosmological distances, and a derivative factor $F(l,z)$, including the evolution of the cosmological fluctuations; these two factors are defined as

$$R(z) = 2\frac{r\left(z_{ls}\right)-r(z)}{r\left(z_{ls}\right)r^3(z)}\ , \tag{4.30}$$

$$F(l,z) = \left[\frac{\partial P_\Psi(k,z)}{\partial z}\right]_{k=\frac{l+1/2}{r(z)}}\ . \tag{4.31}$$

We now study how the contribution to Q_l is distributed over the redshift. For this purpose, it is relevant to study the redshift behavior of dQ/dz for a given l. This analysis tells us at which redshift the integrand of (4.28) is relevant, and answers our question. In Fig. 4.5 we show dQ/dz both including (dashed line) and not including (solid line) the non-linear growth for a fixed multipole. As we can see, in the linear regime, the contribution is always positive, while the non-linearity produce a negative feature; as we can see in a moment,

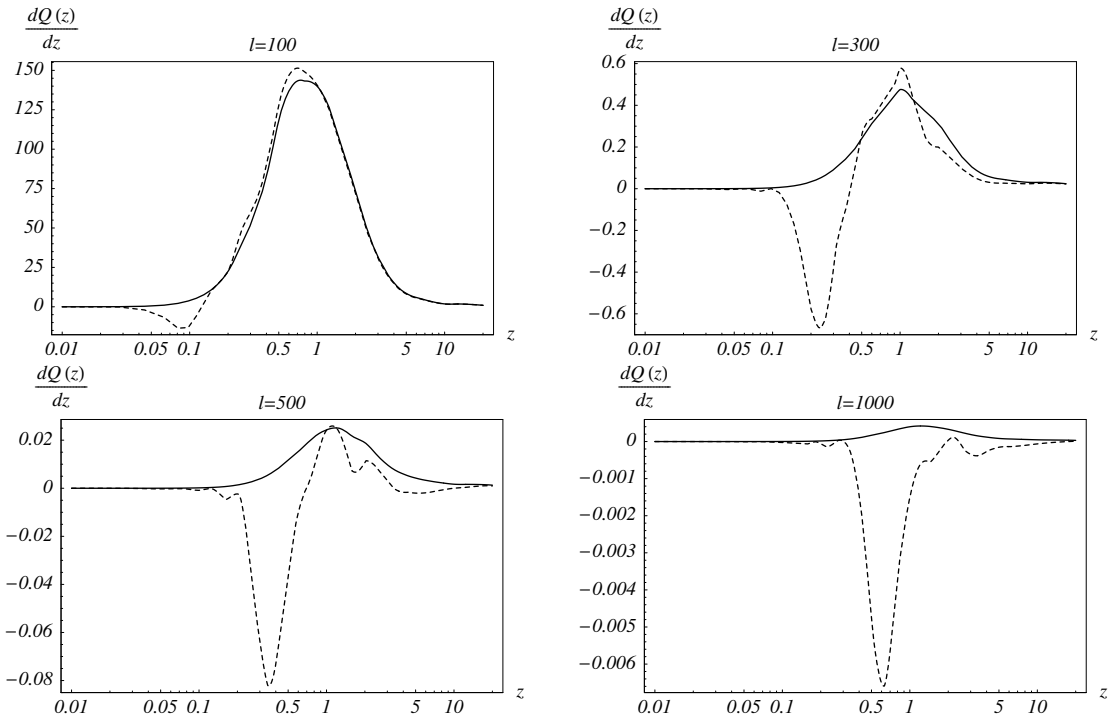

Figure 4.5: dQ/dz as function of redshift in units of 10^{-20} for different multipoles. The solid line describes the contribution from linear perturbations only, while the dashed one represents the case in which the non-linear power is considered.

this can be explained by looking at the time-variation of the gravitational potential, since $dQ/dz \propto dP_\Psi/dz$. The most important and apparent feature is the asymptotic behavior of dQ/dz at $z \to 0$ and $z \to \infty$: in both cases the contribution is vanishing. Actually, most of the power is concentrated between 0.1 and 10 for the scales considered. This aspect, and the overall behavior of the curves, are explained in the following discussion. The relation $\lambda(z) = 2\pi r(z)/l$ links the cosmological scale $\lambda(z)$ with the distances $r(z)$ and the multipole l; for a given l, decreasing the redshift means decreasing $\lambda(z)$. In the past ($z \to \infty$) the scale $\lambda(z)$ is outside the horizon and the Universe is matter or radiation dominated; therefore the gravitational potential remains constant and dQ/dz vanishes. As z decreases, the scale $\lambda(z)$ gets in horizon crossing; in this regime the free streaming of the underlying matter density fluctuations will produce a decrease of the gravitational potential. This yields a $dQ/dz > 0$, visible as the positive part of the curves in the Fig. (4.5). Decreasing further z makes the scale $\lambda(z)$ smaller and smaller matching the scale which is entering the non-

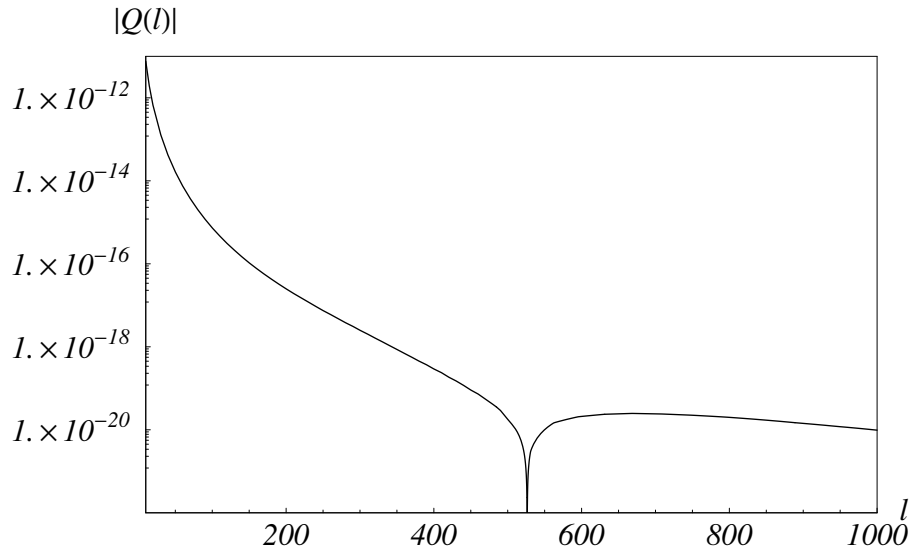

Figure 4.6: $|Q_l|$ for our ΛCDM concordance model. At $l = l_c \approx 550$ the integral is null because the linear contribution balances the non-linear one: for $l < l_c$ the linear growth dominates, for $l > l_c$ the non-linear growth dominates.

linear phase at that epoch; now the power P_Ψ is increasing in time, yielding the negative part of the curves in Fig. 4.5, coming from $dQ/dz < 0$. Approaching the present time ($z \to 0$) the wavenumber k goes to infinity and the power spectrum vanishes (see Fig. 4.2). We make the important conclusion that dQ/dz probes structure formation at non-zero redshifts only, peaking at structure formation, and vanishing at earlier epochs and at present. In particular, as we already stressed, for multipoles between 1000 and 100 dQ/dz is non-null in a redshift interval extremely interesting for the onset of cosmic acceleration, say between 0.1 and 10, and, most importantly, it cuts out the present. As we shall see in the following, these features make the bispectrum useful to study the dark energy dynamics at the epoch in which it starts to be relevant. We conclude this section analyzing Eq. (4.28) in the multipole space; a logarithmic plot of $|Q_l|$ is shown in Fig. 4.6. As we can see, in this example there is a very clear feature at $l_c \approx 550$, where Q_l changes sign and $|Q_l|$ has a cusp. Recalling that Q_l is a line of sight integral, and hence in redshift, the meaning of the cusp in Fig. 4.6 is easy to understand. For $l < l_c$ the linear contribution of dQ/dz is greater than the non-linear one and the overall integral is positive; for $l > l_c$ the non-linear regime dominates and the overall integral is negative; at $l = l_c$ the non-linear power balances

exactly the linear one and the overall integral is zero. The position of the cusp depends on the growth of the cosmic structures and the latter depends on the cosmological parameters; in Ch. 6 we will try to exploit the phenomenology discussed there to discriminate between different cosmological models.

4.2.2 Wigner's 3J symbols

One of the computational challenges to deal with the bispectrum in its full configuration is the evaluation of the Wigner's 3J symbols in Eq. (4.22). We built a numerical machinery to compute them, and we show here the main criteria and features of our approach.

The Wigner's 3J symbols are non-trivial functions of their arguments and they have a closed formula only for very few combinations of l_1, l_2 and l_3, m_1, m_2 and m_3 (see Appendix A); calculating them up to multipoles of the order of 1000 requires refined numerical techniques as we show now. There are routines, developed for nuclear and molecular physics, able to calculate the 3J symbols; unfortunately they fail when the multipoles reach values of the order of 100. Indeed the higher orbital momenta (i.e. the higher multipole) needed in nuclear physics is the higher electron energy level and, for the heaviest element, it is just of the order of 100. On the other hand we need a routine that can evaluate the 3J symbols up to multipoles ten times larger. To obtain the 3J symbols we follow an approach similar to Schulten and Gordon (1975), where two exact recursion relations to evaluate the full set of the 3J symbols were found: the first one evaluates the 3J symbols varying l_1 while the second one varying m_2. Since we are interested in the angle averaged bispectrum, summing m, we choose the second recursion relation for computational convenience.

The recursive relation for the 3J symbols is computed for fixed l_1, l_2, l_3, m_1 and for all the possible values of m_2; m_3 is given by the relation $m_3 = -(m_1 + m_2)$, if this equality is not verified, the 3J symbols vanish. The recursive relation is

$$C(m_2 + 1)g(m_2 + 1) + D(m_2)g(m_2) + C(m_2)g(m_2 - 1) = 0 \ , \tag{4.32}$$

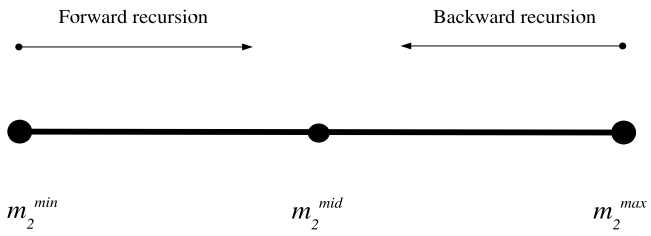

Figure 4.7: Scheme of the recursion relation. The forward recursion starts at $m_2^{\min}$ while the backward one at $m_2^{\max}$; they match in m_2^{mid} where the Wigner's 3J symbols are normalized; the last step is the overall renormalization and the phase condition.

where

$$g(m_2) = \begin{pmatrix} l_1 & l_2 & l_3 \\ m_1 & m_2 & m_3 \end{pmatrix} \tag{4.33}$$

represents the 3J symbols as function of m_2; the coefficients $C(m_2)$ and $D(m_2)$ are defined by

$$C(m_2) = \sqrt{(l_2 - m_2 + 1)(l_2 + m_2)(l_3 + m_3 + 1)(l_3 - m_3)} \ , \tag{4.34}$$

$$D(m_2) = l_2(l_2+1) + l_3(l_3+1) - l_1(l_1+1) + 2m_2m_3 \ , \tag{4.35}$$

and the boundaries of the m_2 domain are given by

$$m_2^{\min} = \max[-l_2, \ -(l_3 + m_1)] \ , \tag{4.36}$$

$$m_2^{\max} = \min[l_2, \ l_3 - m_1] \ . \tag{4.37}$$

To assure numerical stability it is necessary to perform the recursion (4.32) from both ends of the m_2 domain, exploiting the recursion relation forward and backward; since $C(m_2^{\min}) = C(m_2^{\max} + 1) = 0$, the terminal recursions contain only two terms:

$$D(m_2^{\min})g(m_2^{\min}) + C(m_2^{\min} + 1)g(m_2^{\min} + 1) = 0 \ , \tag{4.38}$$

$$D(m_2^{\max})g(m_2^{\max}) + C(m_2^{\max})g(m_2^{\max} - 1) = 0 \ . \tag{4.39}$$

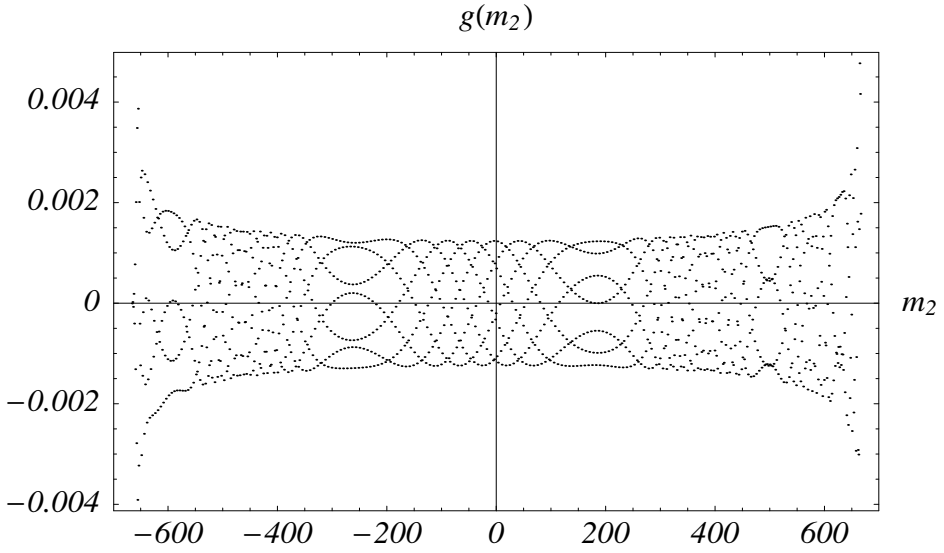

Figure 4.8: Wigner 3J symbols $g(m_2)$ as a function of m_2 evaluated with the recursion relation described in the text. The multipoles are fixed to the following values: $l_1 = 313$, $l_2 = 666$, $l_3 = 750$ and $m_1 = 34$. The value of m_3 is constrained by the relation $m_3 = -(m_1 + m_2)$.

The starting value for the two recursions at the boundaries is arbitrary; a common choice is $g(m_2^{\min}) = g(m_2^{\max}) = 1$. The two recursions meet somewhere in the middle point m_2^{mid} where they will normalized to have the same value. To have the exact full set of the 3J symbols we have to apply the normalization condition and the phase convention

$$\sum_{m_i=m_2^{\min}}^{m_2^{\max}} (2l_1+1)g^2(m_i) = 1 \ , \tag{4.40}$$

$$\text{sign}[g(m_2^{\max})] = (-1)^{l_2-l_3-m_1} \tag{4.41}$$

to the $g(m_2)$ found with the forward and the backward recursions. A rough scheme of the two recursion mechanisms is represented in Fig. 4.7. To give an example of the evaluation of the 3J symbols, in Fig. 4.8 we show an output of our numerical code with $l_1 = 313$, $l_2 = 666$, $l_3 = 750$ and $m_1 = 34$.

Before concluding we make an historical remark. The algorithm developed by Schulten and Gordon to evaluate the 3J symbols was made in 1975; at that time the precision and the speed of the computing machines was much lower than now, so an almost "perfect" and very optimized algorithm was necessary. From this point of view, the double

recursion relation is essential to obtain the correct values of the 3J symbols. During the testing phase of our numerical code we learned that it is possible to work with only one recursion, forward or backward, but with quadruple precision (during the computation and for very high multipole the code must be able to handle numbers of the order of $10^{\pm 1000}$); in this way it is sufficient to normalize the whole set of symbols with (4.40) and (4.41). The use of only one recursion relation is due to the improvement of the performance of the present computers.

4.3 A geometrical analysis of the CMB bispectrum

In Sec. 4.2 we wrote the basic equation describing the bispectrum arising from the correlation between lensing and ISW; here we investigate its main geometrical properties. Since the bispectrum has a triangular configuration we must first define the shape of the triangles; our first choice (and the easiest one) is to study the equilateral configuration with $l_1 = l_2 = l_3 = l$. We limit our range in multipole to $10 \leq l \leq 1000$; the lower bound is set not to approach large angular scales, in order to satisfy the approximations done writing Eq. (4.28).

In the equilateral configuration we probe the CMB with equilateral triangles of different sizes in the multipole space; in this case Eq. (4.22) simplifies and becomes

$$B_l = 3l(l+1)\sqrt{\frac{(2l+1)^3}{4\pi}} \begin{pmatrix} l & l & l \\ 0 & 0 & 0 \end{pmatrix} C_l^P Q_l \ . \tag{4.42}$$

Looking at this new expression, we can notice that the bispectrum is essentially a product between the primordial power spectrum and the correlation of the lensing and the ISW at the same scales; we expect that the bispectrum contains signatures from both C_l^P and Q_l. In Fig. 4.9 we plot the equilateral configuration of the bispectrum as a function of the even multipoles only (for odd l the 3J symbols are zero); two very clear features appear: the bumps and the cusp. The former are a record of the acoustic oscillations of the power spectrum of the primordial anisotropies, represented by C_l^P in (4.42), while the latter is the signature of the change in sign of Q_l due to the balance between the linear and non-linear growth of cosmic structures, as we already discussed.

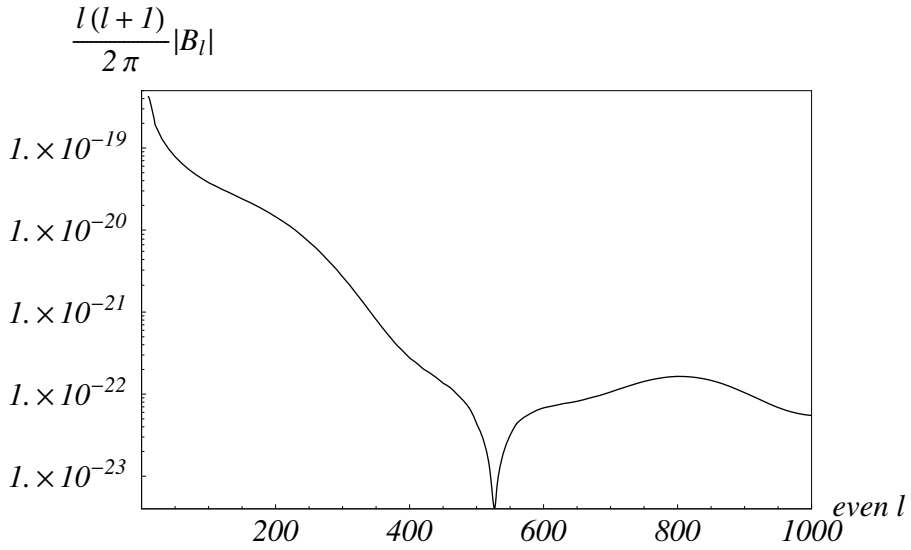

Figure 4.9: Bispectrum equilateral configuration for our ΛCDM model. The bumps are produced by the primordial power spectrum acoustic oscillations; the change in sign, visible as a cusp in logarithmic scale, is the fingerprint of the transition from the linear to the non-linear dominated regime. The plot has been done only for even l, otherwise the 3J symbols are null.

We consider now all the triangular shapes, with no restriction, in the harmonic space; besides equilateral triangles, we will have also isosceles and scalene ones. The bispectrum lives in the three-dimensional space of the three multipoles l_1, l_2 and l_3; thus a representation and a complete analysis of this observable is not so easy. To understand why, it is convenient to write Eq. (4.22) expanding the permutations, obtaining

$$\begin{aligned} B_{l_1 l_2 l_3} = & \sqrt{\frac{(2l_1+1)(2l_2+1)(2l_3+1)}{4\pi}} \begin{pmatrix} l_1 & l_2 & l_3 \\ 0 & 0 & 0 \end{pmatrix} \cdot \\ & \cdot \left[\frac{l_1(l_1+1) - l_2(l_2+1) + l_3(l_3+1)}{2} \left(C^P_{l_1} Q_{l_3} + C^P_{l_3} Q_{l_1} \right) + \right. \\ & + \frac{l_1(l_1+1) - l_3(l_3+1) + l_2(l_2+1)}{2} \left(C^P_{l_1} Q_{l_2} + C^P_{l_2} Q_{l_1} \right) + \\ & \left. + \frac{l_2(l_2+1) - l_1(l_1+1) + l_3(l_3+1)}{2} \left(C^P_{l_2} Q_{l_3} + C^P_{l_3} Q_{l_2} \right) \right] . \end{aligned} \tag{4.43}$$

Reading this formula, we see that the primordial power spectrum and the lensing-ISW correlation are not simply their product at the same l, but we have a mixing between C^P_l and Q_l at different multipoles. We may see this process as a reprojection of the primordial

power over different scales, due to the lensing mechanism.

In Fig. 4.10 we plot the bispectrum in six snapshots fixing each time one multipole. The flat regions are those for which the triangular inequality is not verified (i.e. the three multipoles don't form a triangle); despite of the plots, the bispectrum domain is defined only for $l_1 + l_2 + l_3 =$ even, being otherwise zero because of the 3J symbols. As we can see, increasing l_3 makes the bispectrum surface squeezing along the direction $l_1 = l_2$ and inflating along the orthogonal direction; this behavior is purely geometrical: changing the third multipole the region where the triangular inequalities is verified and where the bispectrum is defined changes. The physics is enclosed into the peaks and canyons clearly visible in the figures; the peaks reflect the harmonic oscillations in the power spectrum while the canyons are the fingerprints of the lensing-ISW correlation; the latter are the higher dimensional counterparts of the cusp shown in Fig. 4.6. As in the equilateral case, the canyons represent the transition from linear to non-linear dominance of the growth of perturbations in the $Q(l)$ integrals and yield a change in sign in the bispectrum appearing "cuspidal" in module and producing "a fall" of the bispectrum's surface; this zero-value is physical and not geometrical as those due to the triangular inequality. The figures show how the combination of the two effects produces a complex pattern for the bispectrum's coefficients: the lensing-ISW correlation redistributes the oscillatory power of C_l^P on multipoles different from the ones of the primordial acoustic oscillations.

To finish this chapter we attempt a study of the three-dimensional bispectrum without fixing any multipole; to do that we plot in Fig. 4.11 the hypersurface of constant $S = Log|B_{l_1 l_2 l_3}|$. For higher values of S (first row of Fig. 4.11) the bispectrum lives near to the axes origin, located at $l_1 = l_2 = l_3 = 10$, and develops along the lines $l_i = l_j$ for $l_k = 10$ (for all permutation of i, j and k); this behavior is due to the fact that the signal is taken only at very low multipoles where the triangular relation is satisfied. Decreasing S (second row of Fig. 4.11) we can see structures growing out of these lines to form a tetrahedron in l-space; inside the tetrahedron, along its edges, there are some swelling that meet in the vertex $l_1 = l_2 = l_3 = 10$. In the last row of Fig. 4.11 we additionally decrease S; a blob in the center of the tetrahedron appears whereas in the last panel of the figure only the tetrahedron remains and the bispectrum takes all the space inside it: all the signal

is acquired. The tetrahedron is simply the bound where the bispectrum is geometrically constrained and its volume is the region where the triangular relation is verified, being a pure geometrical feature. The growing swelling along the edges are produced by the linear phase of the cosmological structure formation while the blob in the center is due to the non-linear phase. That is because higher values of S probe the bispectrum in the linear regime where there is the maximum power (see Figs. 4.6 and 4.9), while the non-linear contribution induces smaller value of S. If, as we already discussed, we want to see the equivalent of the "cusp" of Fig. 4.6, we may notice that the blob is separated from the swelling and this separation is just the equivalent of the "cuspidal" feature of Fig. 4.6.

We conclude here this chapter. We computed and studied the CMB bispectrum arising from the correlation between lensing and ISW effects, we studied its main properties in particular looking at its capability to probe the Universe at redshift relevant for the onset of cosmic acceleration. Despite of the computational difficulty due to the three-dimensional dependence over the angular multipoles, we pushed the phenomenological analysis to the full configuration.

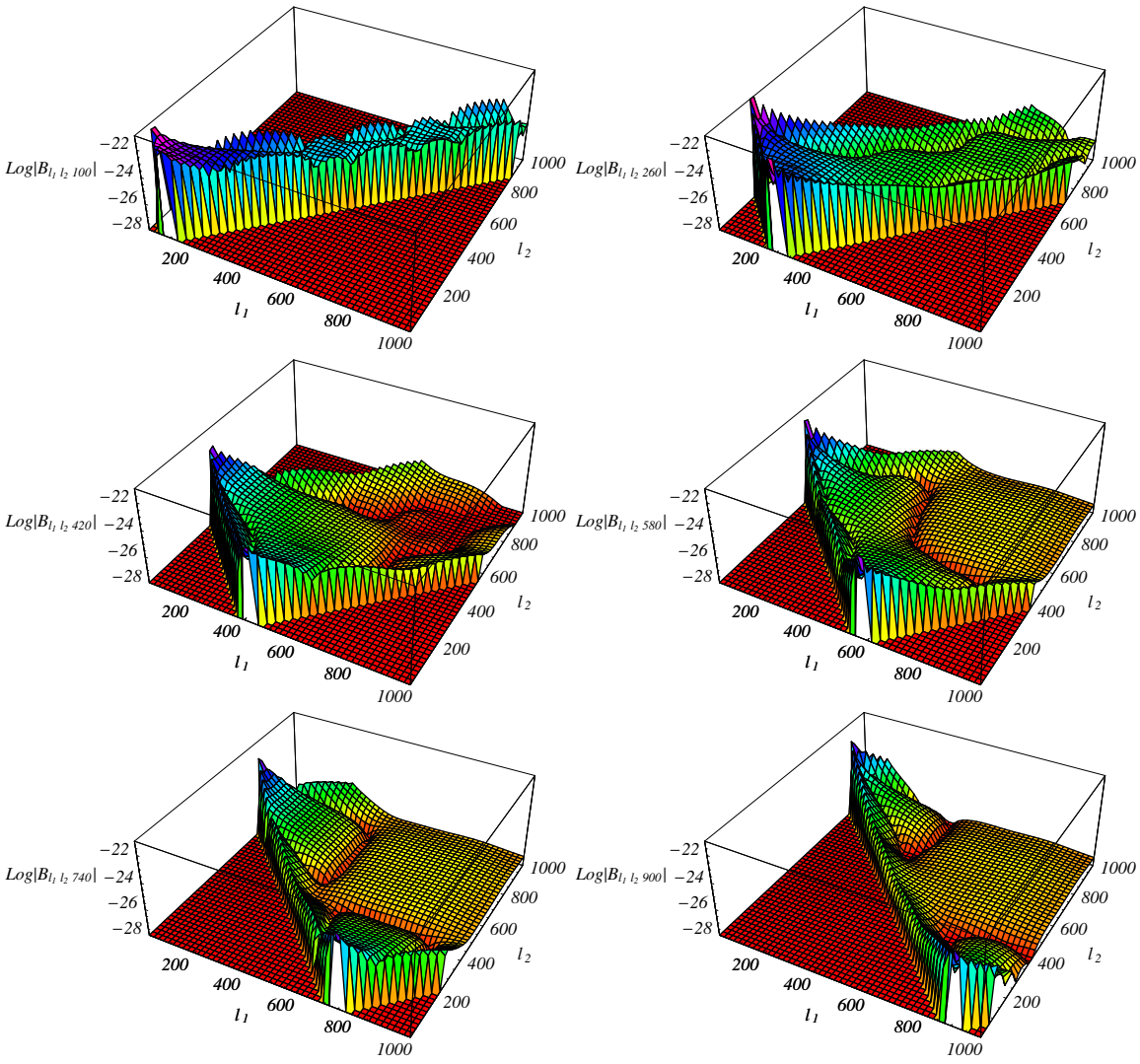

Figure 4.10: Logarithmic plot of the three-dimensional bispectrum fixing one multipole; from left to right and from top to bottom: $l_3 = 100$, $l_3 = 260$, $l_3 = 420$, $l_3 = 580$, $l_3 = 740$ and $l_3 = 900$. The flat regions, fixed at a reference 10^{-28} for graphical reasons, are those for which the triangular inequality is not verified and the bispectrum is null.

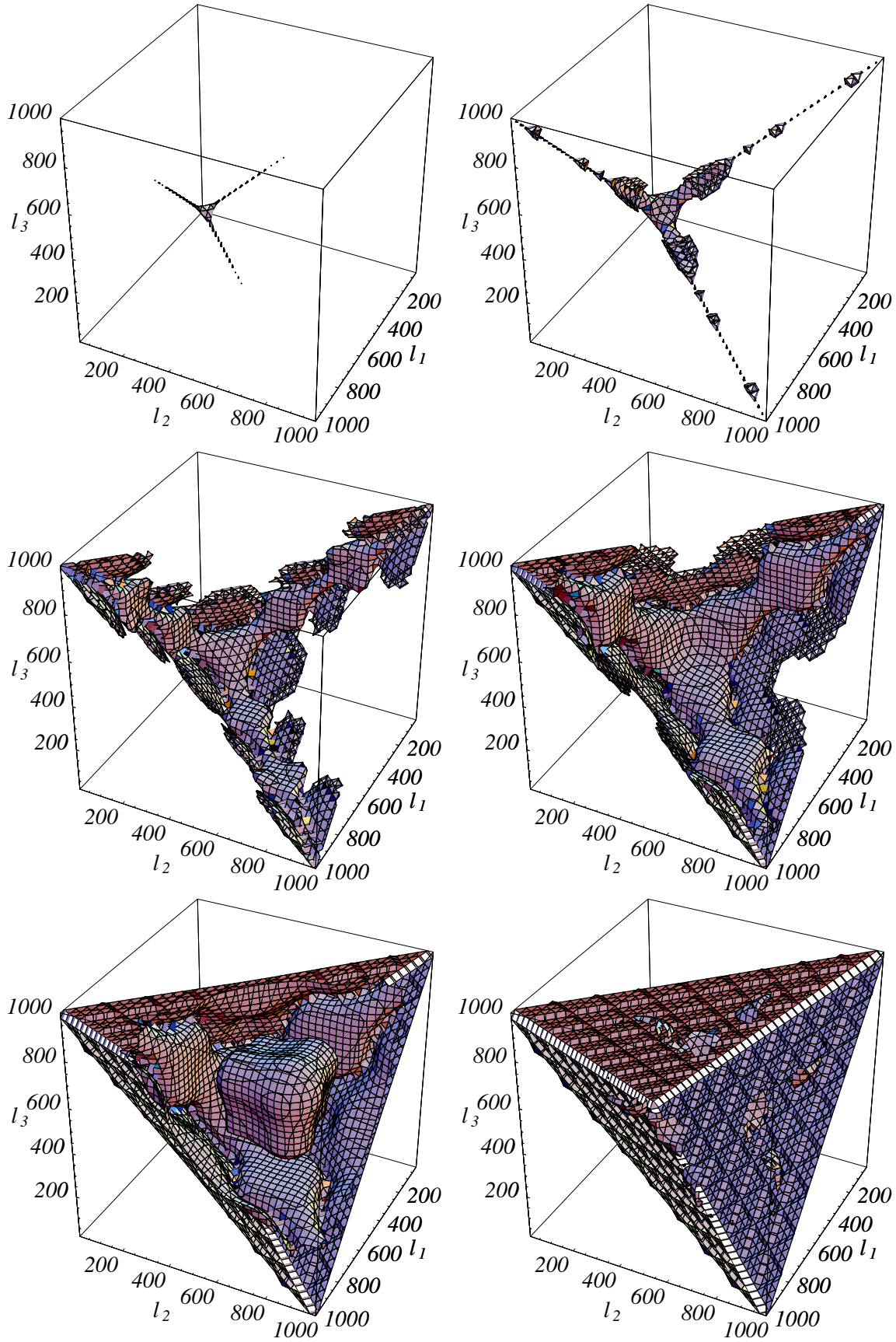

Figure 4.11: Hypersurface of $Log|B_{l_1 l_2 l_3}| = S$. From left to right and from top to bottom $S = 10^{-22}$, 10^{-23}, 10^{-25}, 10^{-26}, 10^{-27}, $10^{-27.5}$.

Chapter 5

Dark energy models

As we have shown in Ch. 2, the dark energy is merely a generalization of the Cosmological Constant, and represents an attempt to find an explanation to the coincidence and fine-tuning problems affecting a vacuum energy density as small as the cosmological critical density today. As we have already mentioned, a large class of dark energy models involves the introduction of a scalar field, the Quintessence, self-interacting and with a shallow potential energy in order to mimic the effect of the Cosmological Constant on the cosmic expansion. Here we want to give an illustration of the main properties of the Quintessence, focusing on the dynamical differences between models currently allowed by observations; in the next chapter, we shall look for the signatures of such differences in the CMB three-point anisotropy statistics. In Sec. 5.1 we describe the general properties of the Quintessence field; in Sec. 5.2 we discuss its background and perturbations dynamics in the framework of the most relevant models proposed for its potential; in Sec. 5.3 we describe a phenomenological approach to the equation of state of the Quintessence which will be useful in the following; in Sec. 5.4 we resume the current constraints on the dark energy equation of state.

5.1 Quintessence

In Sec. 2.4 we briefly introduced the dark energy showing how it modifies the Friedmann equation, how the scalar field evolves with the Klein-Gordon equation and in

which way the energy density and the pressure are defined starting from the scalar field itself. In this chapter we extend that analysis, concentrating on the dark energy dynamics and perturbations. Those properties, i.e. dynamics and spatial perturbations, may allow the dark energy to imprint distinct signatures on CMB and LSS, which may be detected, rejecting the Cosmological Constant scenario.

The Quintessence behavior described in Sec. 2.4 is essentially the minimal one, in which the field is self interacting only; the Quintessence is usually treated in more general context (non-minimal theories) where all the possible degrees of freedom, i.e. with other entities, may be active (see e.g. Matarrese, Baccigalupi & Perrotta 2004 and references therein). In the Extended Quintessence (Perrotta, Baccigalupi & Matarrese 2000, 2000a), the scalar field is non-minimally coupled to the Ricci scalar R with the action

$$S = \int d^4x\sqrt{-g}\left[\frac{1}{16\pi G_*}f(\phi,R) - \frac{1}{2}\omega(\phi)\partial^\mu\phi\partial_\mu\phi - V(\phi) + \mathcal{L}_f\right] , \tag{5.1}$$

originally introduced by Hwang (1991), where $\omega(\phi)$ specifies the kinetic energy of the scalar field, G_* is the bare gravitational constant (Esposito-Farese & Polarski 2001), $\mathcal{L}_f$ is the Lagrangian including all the fluids but Quintessence, finally $f(\phi,R)$ is the function that couples the scalar field to the gravity. An analogous generalization involves the coupling between dark energy and matter (Amendola 2000).

The action above is more general then the one in Sec. 2.4 but, for our purposes, we restrict to a single scalar field with a minimal coupling, which corresponds to have $\omega = 1$ and $f(\phi,R) = R$ in (5.1). The dynamics of the Quintessence scalar field ϕ is completely described by the unperturbed and perturbed Klein-Gordon equation

$$\Box\phi + \frac{dV}{d\phi} = 0 , \tag{5.2}$$

$$\delta(\Box\phi) + \frac{d^2V}{d\phi^2}\delta\phi = 0 , \tag{5.3}$$

where $\Box \equiv (-g)^{-1/2}\partial_\mu[(-g)^{1/2}g^{\mu\nu}\partial_\nu]$ is the D'Alembertian operator applied to a scalar and δ is the variation with respect ϕ. Eq. (5.2) describes the background evolution of the scalar field classical expectation value, while Eq. (5.3) describes the dynamics of its linear perturbation. In order to describe the Quintessence perturbations we choose a flat FRW universe, working in the Newtonian gauge, as we did in (3.15). We also work neglecting the

anisotropic stress, $\Phi = -\Psi$, which is non-null at a linear level, in Extended Quintessence scenarios (Hwang 1991). The Quintessence homogeneous and inhomogeneous pieces in space may be defined as

$$\phi\,(\eta, \vec{x}) = \phi_0(\eta) + \delta\phi\,(\eta, \vec{x}) \ , \tag{5.4}$$

where the fluctuation $\delta\phi$ obeys to the perturbed Klein-Gordon Eq. (5.3) that in the Fourier space becomes

$$\ddot{\delta\phi} + 3H\dot{\delta\phi} + \left(\frac{k^2}{a^2} + \frac{d^2V}{d\phi^2}\right)\delta\phi = 4\dot{\phi}\dot{\Phi} - 2\frac{dV}{d\phi}\Phi \ . \tag{5.5}$$

The perturbations in energy density and pressure of the Quintessence field are described by:

$$\delta\rho_\phi = \dot{\phi}\dot{\delta\phi} + \frac{dV}{d\phi}\delta\phi - \dot{\phi}\Phi \ , \tag{5.6}$$

$$\delta p_\phi = \dot{\phi}\dot{\delta\phi} - \frac{dV}{d\phi}\delta\phi - \dot{\phi}\Phi \ . \tag{5.7}$$

In the following we give a brief description of the most important aspects of the dark energy dynamics, concerning the background expansion and its perturbations.

5.2 Tracking solutions

As we saw in Ch. 2, the motivation to substitute the Cosmological Constant with the Quintessence is the attempt to alleviate the coincidence and the fine-tuning that affect Λ. In this section we show that the Quintessence field in general admits attractors in the space of the trajectories of ϕ. This allow the field to induce the present acceleration in the cosmic expansion phase starting from a wide set of initial conditions in the early Universe, thus alleviating the fine-tuning problem. These trajectories are named tracking solutions. The time in which the scalar field reaches the tracker depends on the energy scale of the potential and fixes the observed amount of the dark energy at the present. Thus the tracking solution may solve the problem of initial conditions, but not the coincidence, ultimately related to the energy today and fixed by hands in tracking trajectories. Our treatment follows closely that of Liddle and Scherrer (1998); they also define the "scaling solution" as those in which the scalar field energy density scales exactly as a power law of the scale factor.

To show the main properties of the tracking solutions, we consider a flat FRW universe filled by a perfect fluid f, either matter or radiation, and a scalar field ϕ. We assume that both the Quintessence and fluid energy density evolve with the scale factor as

$$\rho_\phi \propto a^{\beta_\phi} = a^{-3\left(1+w_\phi\right)} , \tag{5.8}$$

$$\rho_f \propto a^{\beta_f} = a^{-3\left(1+w_f\right)} , \tag{5.9}$$

being w_ϕ and w_f the equation of state of the Quintessence and the perfect fluid, respectively. In order to have Eqs. (5.8) and (5.9), w_ϕ must remain constant during the single epoch when each fluid dominates. The energy conservation (2.8) for the Quintessence can be rewritten as

$$\dot{\rho}_\phi = -3H\dot{\phi}^2 , \tag{5.10}$$

simply using the definition of the energy density (2.27) and the pressure (2.28) for a scalar field. Since the energy conservation tells that $\dot{\rho}_\phi/\rho_\phi = -\beta_\phi H = -3\left(1+w_\phi\right)H$, the previous equation becomes

$$\frac{\dot{\phi}^2}{2\rho_\phi} = \frac{\beta_\phi}{6} = \frac{1+w_\phi}{2} . \tag{5.11}$$

This means that the ratio between kinetic energy and the total energy density of the Quintessence must remain constant in the regime given by (5.8). The two extreme regimes, when the kinetic energy becomes dominant or negligible with respect the total energy density, provide two limits for the equation of state of the Quintessence: $w_\phi = -1$ if $\dot{\phi}^2$ is negligible, yielding $\rho_\phi =$ constant and a Cosmological Constant behavior; $w_\phi = 1$ if $\dot{\phi}^2$ is dominant with $\rho_\phi \propto a^{-6}$.

In the epoch when the perfect fluid dominates, the scale factor evolves with time as $a \propto t^{2/\beta_f}$, thus the Klein-Gordon equation (5.2) can be rewritten as

$$\ddot{\phi} + \frac{6}{\beta_f t}\dot{\phi} + \frac{dV}{d\phi} = 0 . \tag{5.12}$$

Substituting the power law behavior (5.8) into its conservation equation (5.10), we obtain the time-evolution of $\dot{\phi}$ as a function of β_f and β_ϕ

$$\dot{\phi} \propto t^{-\beta_\phi/\beta_f} . \tag{5.13}$$

We are able now to determine the shape of the potential $V(\phi)$ in order to have tracking solutions for ρ_ϕ. In fact the solution of the previous equation, that depends on the ratio β_ϕ/β_f, is

$$\phi \propto \begin{cases} \ln t & (\beta_f = \beta_\phi) \\ A t^{1-\beta_\phi/\beta_f} & (\beta_f \neq \beta_\phi) \end{cases} , \tag{5.14}$$

substituting this result into Eq. (5.12) and solving for the scalar field potential, we obtain

$$V(\phi) = \begin{cases} \frac{2}{\lambda^2}\left(\frac{6}{\beta_f} - 1\right) e^{-\lambda\phi} & (\beta_f = \beta_\phi) \\ \frac{6-\beta_\phi}{2\beta_\phi}\left(1 - \frac{\beta_\phi}{\beta_f}\right)^2 A^{2-\gamma}\phi^\gamma & (\beta_f \neq \beta_\phi) \end{cases} , \tag{5.15}$$

that can be rewritten also in terms of the equation of state of the perfect fluid and Quintessence:

$$V(\phi) = \begin{cases} \frac{2}{\lambda^2}\frac{1-w}{1+w} e^{-\lambda\phi} & (w = w_f = w_\phi) \\ \frac{1}{2}\frac{1-w_\phi}{1+w_\phi}\left(\frac{w_f - w_\phi}{1+w_f}\right)^2 A^{2-\gamma}\phi^\gamma & (w_f \neq w_\phi) \end{cases} , \tag{5.16}$$

where λ and A are constant of integration and $\gamma = 2\beta_\phi/(\beta_\phi - \beta_f)$.

The potential found when $\beta_f = \beta_\phi$ is the well investigated exponential potential (Lucchin & Matarrese 1985; Halliwell 1987; Burd & Barrow 1988) for the limiting case where $\rho_\phi \ll \rho_f$. Providing $\beta_f/\lambda^2 < 1$, this potential has a tracker solution with $\rho_\phi = \left(\beta_f/\lambda^2\right)\rho_{tot}$ as a unique late-time attractor (Wetterich 1988a, Ratra & Peebles 1988). In order to provide acceleration, the Quintessence energy density may not scale as the dominant component (matter) today, and some mechanism must be invoked to break such behavior (Wetterich 1988a; Liddle & Scherrer 1998).

The class of potentials found when $\beta_f \neq \beta_\phi$ are power law potentials with exponent γ, including the inverse power law potential studied by Ratra and Peebles (1988). To have a growing Quintessence energy density compared to the perfect fluid, that means $\beta_f > \beta_\phi$, we need a negative γ otherwise we have that ρ_ϕ decrease more rapidly than ρ_f. We can express β_ϕ in terms of γ and β_f obtaining

$$\beta_\phi = \frac{\gamma}{\gamma - 2}\beta_f \ . \tag{5.17}$$

This relation shows that, in order to have scaling solutions for a positive power law potential, the exponent γ must be restricted to $\gamma > 2$ because both β_f and β_ϕ are positive. Eq. (5.17)

can be rewritten in terms of the equation of state as

$$w_\phi = \frac{\gamma w_f + 2}{\gamma - 2} \ . \tag{5.18}$$

Thus, following Liddle and Scherrer (1998), we have classified all the potentials that show a scaling behavior for Quintessence energy density, they are exponential, yielding a Quintessence energy density scales as the dominant cosmological component, or negative (inverse) power law in which the Quintessence energy density decreases less rapidly than the dominant perfect fluid. For positive power laws, the Quintessence energy density decreases more rapidly than the dominant component.

Now we turn to study the attractor properties of the power law potentials. For convenience we rewrite the power law potential as $V(\phi) = V_0\phi^\gamma$, thus Eq. (5.12) can be rewritten as

$$\ddot{\phi} + \frac{6}{\beta_f t}\dot{\phi} + \phi^{\gamma-1} = 0 \ , \tag{5.19}$$

where V_0 has been absorbed simply rescaling t; thus A becomes

$$A = \left[\left(\frac{2}{\gamma-2}\right)\left(\frac{6}{\beta_f} - \frac{\gamma}{\gamma-2}\right)\right]^{\frac{1}{\gamma-2}} \ . \tag{5.20}$$

With the change of variables $t = e^y$, $u(y) = \phi(y)/\phi_e(y)$ (Ratra & Peebles 1988; Liddle & Scherrer 1998), being $\phi_e(y)$ the exact solution given by Eqs. (5.14) and (5.20), the Klein-Gordon equation (5.19) becomes

$$\frac{d^2u}{dy^2} + \left(\frac{6}{\beta_f} - \frac{4}{\gamma-2} - 1\right)\frac{du}{dy} + \frac{2}{\gamma-2}\left(\frac{\gamma}{\gamma-2} - \frac{6}{\beta_f}\right)\left(u - u^{\gamma-1}\right) = 0, \tag{5.21}$$

that can be split into a system of differential equations:

$$\begin{cases} \frac{du}{dy} = p \\ \frac{dp}{dy} = -\left(\frac{6}{\beta_f} - \frac{4}{\gamma-2} - 1\right)p - \frac{2}{\gamma-2}\left(\frac{\gamma}{\gamma-2} - \frac{6}{\beta_f}\right)\left(u - u^{\gamma-1}\right) \end{cases} . \tag{5.22}$$

This system has three critical points, for which the scalar field asymptotically approaches the exact solution ϕ_e with $\dot{\phi} = 0$, they are located at $p = 0$ and $u = 0, \ \pm 1$ in the (u, p) plane. In order to have attractors in the phase space, the critical points must be stable. While $(u = 0, p = 0)$ is always unstable (saddle point), the stability of $(u = \pm 1, p = 0)$

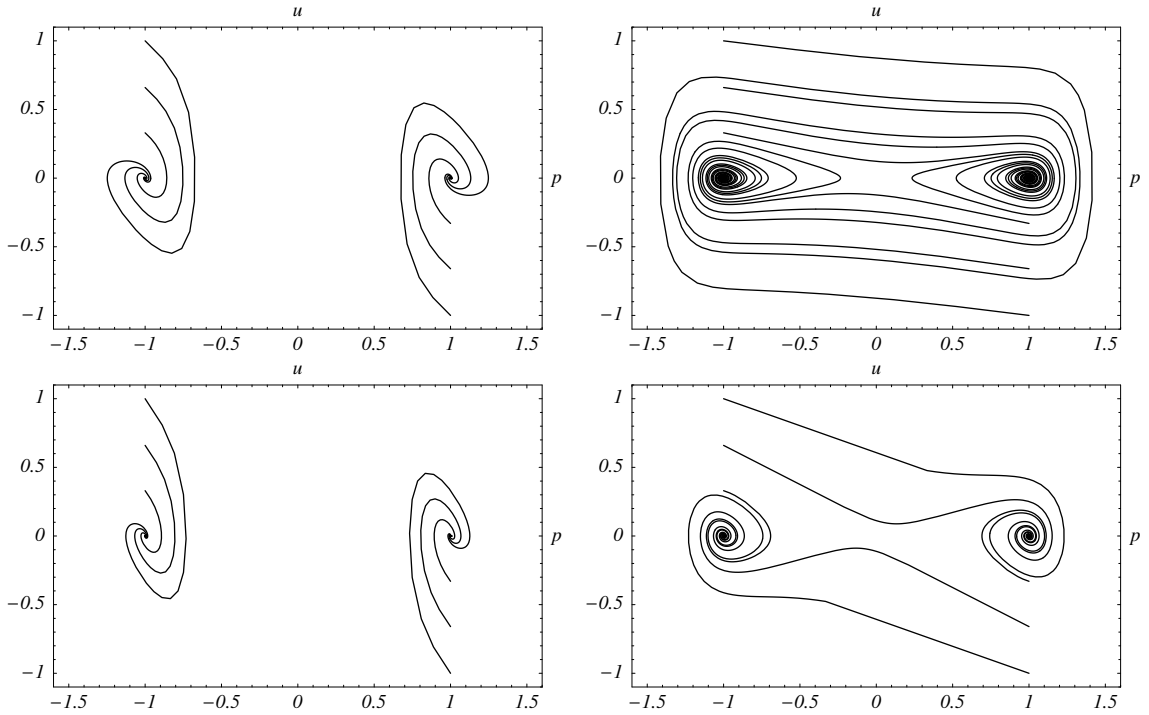

Figure 5.1: Tracking trajectories with different initial conditions in the phase plane (u, p) for radiation dominated (first row) and matter dominated (last row) eras for power law potentials. The power law slope is $\gamma = -6$ in the first column and $\gamma = 12$ in the second column. The trajectories spiral inwards joining the attractor.

depends on the shape of the potential, i.e. on γ (Liddle & Scherrer 1998), thus the stability conditions can be written as

$$\gamma < 2\frac{6+\beta_f}{6-\beta_f} \quad (\gamma < 0) \ , \tag{5.23}$$

$$\gamma > 2\frac{6+\beta_f}{6-\beta_f} \quad (\gamma > 0) \ . \tag{5.24}$$

For γ negative the inequality is always verified; on the other hand for positive values of γ the stability condition may not be verified. Thus the inverse power law potential possesses always stable attractors, while the power law potentials with positive exponent have stable attractors only for sufficiently large values of γ depending on the dominant perfect fluid. For example in radiation domination ($\beta_f = 4$) the attractor scaling solutions exist for $\gamma > 10$, while for matter domination ($\beta_f = 3$) the stability condition gives us $\gamma > 6$. In Fig. 5.1 we plot tracking trajectories both in the radiation and the matter dominated epochs for

positive and negative power laws. Making a rough analysis, the trajectories that cross the $u = 0$ axis correspond to solutions in which the scalar field oscillates around its minimum in the potential, while trajectories confined in the semi-plane $u > 0$ or $u < 0$ correspond to solutions in which ϕ approaches its minimum without oscillating.

The relevant property of the potentials discussed above is that for a wide range of initial conditions, the trajectories of the scalar field approach some critical points (see Fig. 5.1) providing a classical solution to the fine-tuning problem of the Cosmological Constant. The introduction of a scalar field is motivated by several reasons, also physical and not only phenomenological; one is that it arises naturally in unified theories and is a necessity in supersymmetric theories where it plays the role of supersymmetric partners of the standard model fermion fields. Many potentials have been introduced in the literature; here we briefly review four relevant potentials that have been studied, and their theoretical origin.

- Quadratic potential: $V(\phi) = \frac{1}{2}m^2\phi^2$.

  This potential was introduced in the chaotic inflation scenario by Linde (1983) and the only free parameter is the mass m of the field that should be $m = \sqrt{2\Omega_\phi \rho_c}/M_P \simeq 10^{-33}$ eV if the field today has the value of the Planck mass (Brax, Martin & Riazuelo 2000) and has to provide acceleration. Since this value is very tiny, a problem analogue to having a very low value of ρ_ϕ arises. Thus, in this case, the introduction of the Quintessence does not solve the problems listed in Sec. 2.3 affecting the Cosmological Constant, not even the fine-tuning. In addition, according to Eq. (5.17) that imposes $\gamma > 2$, this potential does not present attractors.

- Exponential potential: $V(\phi) = M^4 e^{-\lambda\phi}$.

  This potential leads to a "time-varying" Cosmological Constant, which has a late time asymptotic solution characterized by a constant ratio $\rho_\phi(t)/\rho(t)$ (Wetterich 1988) as we have already seen in the above discussion. Exponential potentials arise naturally in all models of unification with gravity as Kaluza-Klein theories, supergravity theories or string theories (see e.g. Green, Schwarz & Witten 1987 and references therein). As we already have shown, this potential has only one attractor depending on the value of λ (Wetterich 1988a; Copeland, Liddle & Wands 1998).

- Ratra-Peebles potential: $V(\phi) = \frac{M^{4+\alpha}}{\phi^\alpha}$ with $\alpha > 0$.
  The inverse power law potential was first studied by Ratra and Peebles (1988). As we shown above, this potential possess two attractors in the phase plane for all the values of α and allows attracting tracking solutions for ρ_ϕ. The inverse power law potentials $V \propto \phi^{-\alpha}$ arise in super-symmetric gauge theories (Binetruy 1999); and is generated at low energy. This model has been developed in order to reconcile the phases of cosmic evolution when the scalar field is dominant, with the phase in which ϕ becomes subdominant.

- Supergravity inspired potential: $V(\phi) = \frac{M^{4+\alpha}}{\phi^\alpha} e^{\frac{1}{2}\left(\frac{\phi}{M_P}\right)^2}$ with $M_P^2 = \frac{1}{8\pi G}$.
  This potential is derived from applying correction originating from supergravity effects to the inverse power law potentials. In particular Brax and Martin (1999, 2000) showed that inverse power law models leading to Quintessence are stable against quantum corrections, both in the supersymmetric and non-supersymmetric cases.

We discuss now the latter two potential in some more details, as they well represent the different dynamics that the dark energy might have, and we shall use them as sort of reference models in the next chapter.

5.2.1 Ratra-Peebles potential

As above, we may write the Ratra-Peebles (RP) potential as

$$V_{RP}(\phi) = \frac{M^{4+\alpha}}{\phi^\alpha} \ . \tag{5.25}$$

If the Quintessence is subdominant, the attractor is characterized by $\rho_\phi \propto a^{-4/(\alpha+2)}$. This potential depends on two free parameters: the energy scale M and the index $\alpha > 0$. A remarkable feature is that the two attractive tracking solutions in the phase plane, shown in Fig. 5.1, exist *independently* on the value of α and the energy scale M. The index α is a priori a free parameter that determines the shape of the potential, whereas the energy scale is fixed by the requirement that $\Omega_\phi \simeq 0.7$ today (see e.g. Zlatev, Wang & Steinhardt 1998). The relation between M and Ω_ϕ can be obtained as follows if at the present, $\phi \approx M_P$; substituting this condition into Eq. (5.25) and neglecting the kinetic term into Eq. (2.27)

we obtain

$$M \approx (\Omega_\phi \rho_c M_P^\alpha)^{\frac{1}{\alpha+4}} \ . \tag{5.26}$$

To give an order of magnitude, fixing $\alpha = 6$ we have $M = 10^6$ GeV.

The Klein-Gordon equation with the RP potential in the radiation and in the matter domination era has exact tracking solutions for the evolution of ϕ that are both attractors; according to Eq. (5.14) they are

$$\phi \propto \begin{cases} a^{-\frac{4}{\alpha+2}} & \text{(radiation era)} \\ a^{-\frac{3}{\alpha+2}} & \text{(matter era)} \end{cases} \ . \tag{5.27}$$

consequently, using Eq. (5.17), the Quintessence energy density scales with a as

$$\rho_\phi \propto \begin{cases} a^{-\frac{4\alpha}{\alpha+2}} & \text{(radiation era)} \\ a^{-\frac{3\alpha}{\alpha+2}} & \text{(matter era)} \end{cases} \ . \tag{5.28}$$

while the equation of state is

$$w_\phi = -\frac{2}{\alpha+2} \ . \tag{5.29}$$

Since ρ_ϕ evolves slower than radiation and matter, the Quintessence becomes the dominant component at some stage of the cosmic evolution, depending essentially on M.

To quantify the properties of the family of inverse power law potentials we fix the index $\alpha = 6$, we require that $\Omega_\phi = 0.7$, obtaining $M \approx 4.8 \times 10^6$ GeV from (5.26) and we assume that ϕ is on track today. As pointed out by Steinhardt, Wang & Zlatev (1999), this scenario possesses at least three important advantages. First, one can hope to avoid the fine-tuning, as we mentioned already. Second, the solution will be on track today for a huge range of initial conditions. In fact, fixing the initial condition at $z = 10^{28}$ (the end of inflation, see e.g. Dodelson 2003 and references therein), the allowed range of initial values for the Quintessence energy density are $10^{-37}\text{GeV}^4 \leq \rho_\phi \leq 10^{61}\text{GeV}^4$, being the lower and the upper bound approximately the background energy density ρ_f at equality and at the initial time respectively. If ϕ starts at rest, this means that the initial condition are $10^{-18} M_P \leq \phi_i \leq 10^{-2} M_P$. Third, the value of the Quintessence equation of state is constrained automatically to $-1 \leq w_\phi \leq 0$; its precise value depends only on the functional form of the potential, i.e. the slope α, once Ω_ϕ is fixed.

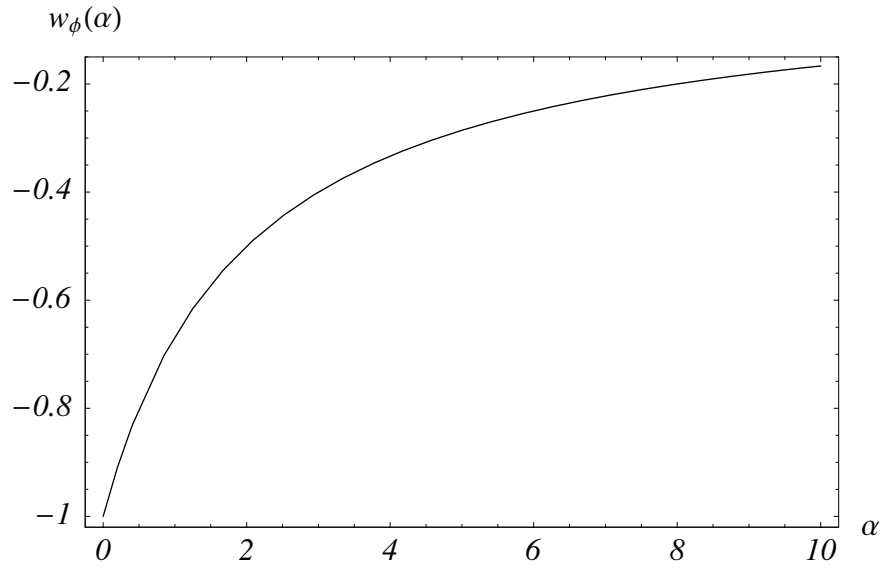

Figure 5.2: Quintessence equation of state w_ϕ for Ratra-Peebles potential as function of α. In order to be consistent with the current constraints, α must be in the range $0 < \alpha < 0.5$.

In the Ratra-Peebles scenario, if we require the present equation of state to be in agreement with the current constraints (Spergel *et al.* 2003), say $-1 < w < -0.8$, the exponent must be the range $0 < \alpha < 0.5$, yielding a shallow potential shape, see Fig. 5.2. At the present, the tracking regime is broken because the dark energy is no longer a subdominant component, but the shallow potential shape makes the present equation of state not far from the tracking one in Eq. (5.29), differing typically at the 10% level (Baccigalupi *et al.* 2002).

5.2.2 SUGRA potential

A more physically realistic potential for ϕ has been built by Brax and Martin (1999, 2000) taking into account Supergravity (SUGRA) corrections to the inverse power law potential:

$$V_S(\phi) = \frac{M^{4+\alpha}}{\phi^\alpha} e^{\frac{1}{2}\left(\frac{\phi}{M_P}\right)^2} . \tag{5.30}$$

The exponential factor in (5.30) is a direct consequence of imposing that the expectation value of the superpotential vanishes (Brax & Martin 1999; Copeland, Nunes & Rosati 2000). The presence of the exponential term into the potential flattens the shape in the region

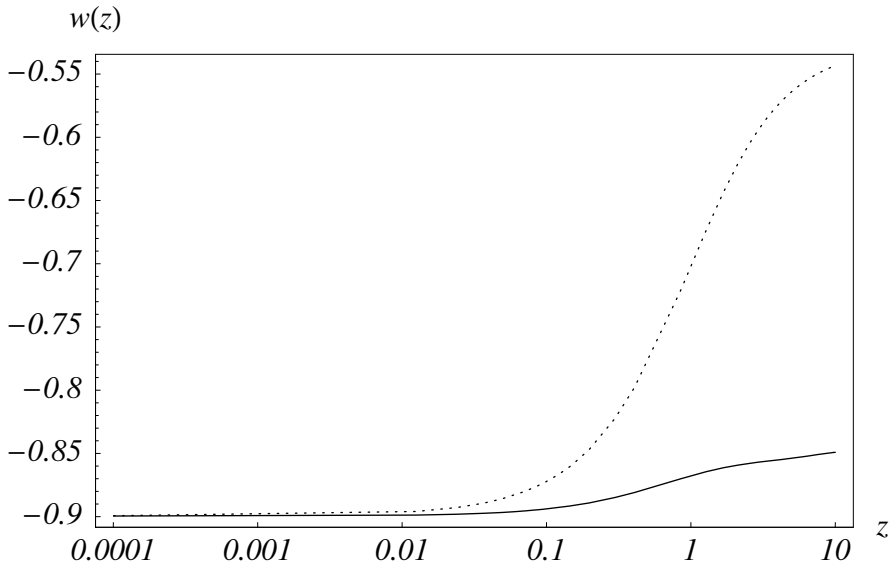

Figure 5.3: Equation of state as function of redshift in logarithmic scale for the Ratra-Peebles (solid line) and the SUGRA potential (dotted line) both having the same value (-0.9) at the present. The other cosmological parameters are fixed to a concordance model (see text). Due to the exponential factor in the SUGRA potential, the present value of the equation of state is obtained with $\alpha_{RP} = 0.34$ for RP and $\alpha_S = 1.76$ for SUGRA.

corresponding to the late time evolution of the scalar field, leaving unchanged the dynamics during the radiation and the matter era. Thus the SUGRA potential provides a solution to the fine-tuning problem just as the RP one in typical tracking trajectories. Since the initial value of ϕ is very small with respect the Planck mass, the exponential factor is not negligible only at low redshift. Thus the evolution of the equation of state is almost unchanged with respect the inverse power law potential at high redshifts (when $\phi \ll M_P$) while is modified at low redshift (when $\phi \simeq M_P$). Qualitatively the exponential factor in (5.30) has the effect to reincrease the potential energy in comparison to the kinetic one pushing down the equation of state towards $w_\phi = -1$ when the kinetic energy vanishes. This means that a given equation of state at present is obtained for values of α sensibly larger than in the RP case, meaning that the dark energy dynamics, and thus the cosmological expansion rate, as a function of the redshift, are generally sensibly different in the two cases.

To show the main phenomenological differences between the RP potential and the SUGRA one we plot in Fig. 5.3 the equation of state for these two potentials imposing

$w = -0.9$ today (the underlying cosmology is a flat FRW universe with $h = 0.7$, $\Omega_b h^2 = 0.022$, $\Omega_{cdm} + \Omega_b = 0.3$, $\Omega_\phi = 0.7$, three species of massless neutrinos and a scale invariant scalar perturbation spectrum with no gravitational waves). The small redshift behaviors are similar for both models, since they have to converge to $w = -0.9$ for $z \to 0$, whereas at higher redshift the two Quintessence scenarios have a markedly different shape reflecting the two different values of α required to have the same equation of state at the present; specifically $\alpha_{RP} = 0.34$ for RP and $\alpha_S = 1.76$ for SUGRA. In other words, fixing the present value of the equation of state the time evolution of w is greater for the SUGRA potential.

5.2.3 Quintessence perturbations

We examine now qualitatively and briefly how the Quintessence fluctuations modify the growth of matter density perturbations, represented in terms of the density contrast δ_m, with respect the Λ case (for more details see Ferreira & Joyce 1997; Perrotta & Baccigalupi 1999 and references therein). As we see in a moment, on small scales the Quintessence is smooth, thus its perturbations in energy density and pressure are negligible with respect to those of matter, and the evolution of δ_m is the same as the case with Cosmological Constant (Caldwell, Dave & Steinhardt 1998). On super-horizon scales the effect of Quintessence perturbations modify the growth rate of δ_m because the scalar field clusters contributing to the energy density and pressure perturbations. Indeed, looking at Eq. (5.5), we may notice that, as well as the background ϕ, also the perturbation $\delta\phi$ behave as a scalar field with an effective mass given by $m_\phi^2 = d^2V/d\phi^2$. It is important to associate to $\delta\phi$ the wavenumber $k_\phi \sim d^2V/d\phi^2$ and the wavelength $\lambda_\phi = k_\phi^{-1}$ characterizing the different regimes in the Quintessence perturbation, massless for $\lambda \ll \lambda_\phi$, and vice-versa in the opposite regime. Since in typical Quintessence models the potential is flat in order to provide acceleration, λ_ϕ is of the order of the horizon scale H^{-1} (Ma *et al.* 1999). This is the reason why on sub-horizon scales ($\lambda \ll \lambda_\phi$) the Quintessence perturbations $\delta\rho_\phi$ do not affect the evolution of δ_m, as $\delta\phi$ behaves as scalar radiation, as we anticipated above. On the other hand, on large scales ($\lambda \gg \lambda_\phi$) the Quintessence perturbation $\delta\rho_\phi$ may grow, dragged by the background dynamics (Brax, Martin & Riazuelo 2000), leading to a clustering of the scalar field and affecting the evolution of the matter density contrast. The

influence of perturbations in the Quintessence field on growth of matter perturbations are evident when we compare the matter transfer function of a Quintessence model with that of a ΛCDM model. On scales smaller than λ_ϕ the transfer functions are indistinguishable, while on scales larger than λ_ϕ a bump occurs in Quintessence models with respect to ΛCDM cosmologies, powered by the Quintessence fluctuations (Ma *et al.* 1999). We do not push our analysis further. Indeed, for equation of state consistent with the present constraints (Tegmark *et al.* 2004), such effect is modest (Ma *et al.* 1999).

The qualitative behavior of Quintessence perturbations shown above is not unique and tightly depends on the way in which we model the Quintessence. For example, with the action (5.1) of the Extended Quintessence, the energy density perturbations $\delta\rho_\phi$ can be non-vanishing also if $\delta\phi \to 0$ (Perrotta & Baccigalupi 2002). This behavior is caused by the metric induced perturbations, related to the Ricci scalar that couples with the scalar field itself. Since the growth in the matter perturbations may drag the Extended Quintessence density perturbations to a non-linear regime, the formation of Quintessence clumps also on sub-horizon scales cannot be excluded, and this possibility is under investigation by several authors (Perrotta & Baccigalupi 2002; Amendola 2004).

5.3 A phenomenological approach

From a phenomenological point of view, it is very difficult to get some general information constraining some particular Quintessence model from observations. In fact, as we have seen, several Quintessence potentials have been proposed in these years; a common feature of almost all of them is that they lead to a similar late time behavior. On the other hand we can approach the problem from another point of view, parameterizing the Quintessence equation of state in terms of known observables. This approach allows us to study the Quintessence effects in cosmology without any specification about the potential of the scalar field. On the other hand, we loose a proper treatment of Quintessence fluctuations.

Since the Quintessence becomes dominant only in the recent cosmological epochs, it is useful to parameterize the equation of state at low redshifts. This has been done by several authors, and here we concentrate on the model proposed by Chevallier & Polarski

(2001) and fully developed by Linder (2003). Very detailed models to parameterize the dark energy equation of state exist (see e.g. Corasaniti & Copeland 2003 and references therein), but the easiest way to do that is to expand w into Taylor's series around $z = 0$ obtaining

$$w(z) = w_0 + w_1 z \ , \tag{5.31}$$

where $w_0 = w(0)$ is the value of the equation of state today and $w_1 = w'(0)$ is its redshift derivative at the present. Although very easy, for $z \gg 1$ this parameterization leads to a diverging w, producing unsuitable effects on the distance to the last scattering surface, linear growth rate of perturbations, etc.

A new parameterization, as proposed by Chevallier and Polarski (2001) and Linder (2003), consists in the expansion of the equation of state in Taylor's series as a function of the scale factor a instead of the redshift z. Thus the expansion around the present time will be at $a = 1$ instead of $z = 0$, giving

$$w(a) = w_0 + w_a(1 - a) \ . \tag{5.32}$$

Recalling the relation between the scale factor and the redshift $a = 1/(1 + z)$, the former relation becomes

$$w(z) = w_0 + w_a \frac{z}{1 + z} \ . \tag{5.33}$$

The model (5.33) keeps both the mathematical simplicity, with only two free parameters, and the physical interpretation of (5.31) having several advantages. First of all, the model (5.33) does not show the linear growth of (5.31) at high redshift while at low redshift the two models reproduces to the same behavior. Second, as we shall show later with an example, the parameterization (5.33) mimics with an high accuracy the equation of state of many scalar field models and the derived distance-redshift relations. Third, it is a convenient way to compare the predictions in dark energy cosmologies with the observational data. The only issue is that Eq. (5.33) is not able to reproduce the equation of state for the potentials yielding an oscillating or rapid evolution behavior for the scalar field. In Fig. 5.4 we plot the equation of state as a function of redshift for the model (5.33) and SUGRA fixing for both models the value of the equation of state today to $w_0 = -0.9$; w_a is set to reproduce the SUGRA one at $z = 1$ yielding $w_a \approx 0.4$. The accuracy of the model (5.33) in matching

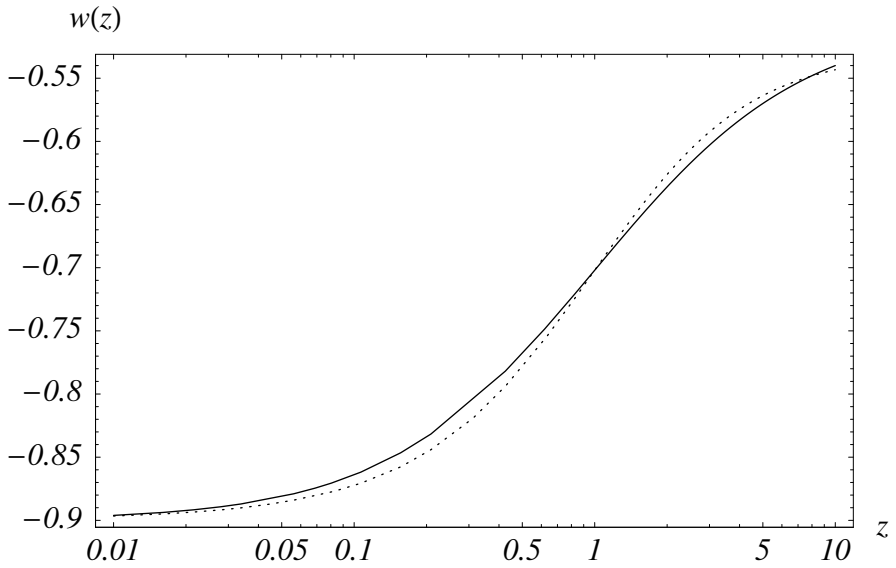

Figure 5.4: Comparison between the dark energy equation of state as modelized in Eq. (5.33) (solid line) and the SUGRA potential (dotted line). Both the models have the same present value of the equation of state, $w_0 = -0.9$, while $w_a \approx 0.4$.

the equation of state for the SUGRA behavior, in the range of redshift plotted in the figure (which is relevant because the dark energy starts to show its effects on the expansion rate), is always between 1.6 % and -1.8%.

We close this section rewriting Eq. (5.33) in a more convenient way as

$$w(z) = w_0 + (w_\infty - w_0)\frac{z}{1+z} \ , \tag{5.34}$$

where w_0 is the same as in (5.33) and w_∞ is the asymptotic value, for $z \to \infty$, of the dark energy equation of state. Using the previous form of the equation of state, it is easy to see that the Quintessence density parameter scales with the redshift as

$$\Omega_V(z) = \Omega_V (1+z)^{3(1+w_\infty)} \exp\left[3\,(w_0 - w_\infty)\,\frac{z}{1+z}\right] \ . \tag{5.35}$$

The form (5.34) of the model described in this section will be widely used in the next chapter.

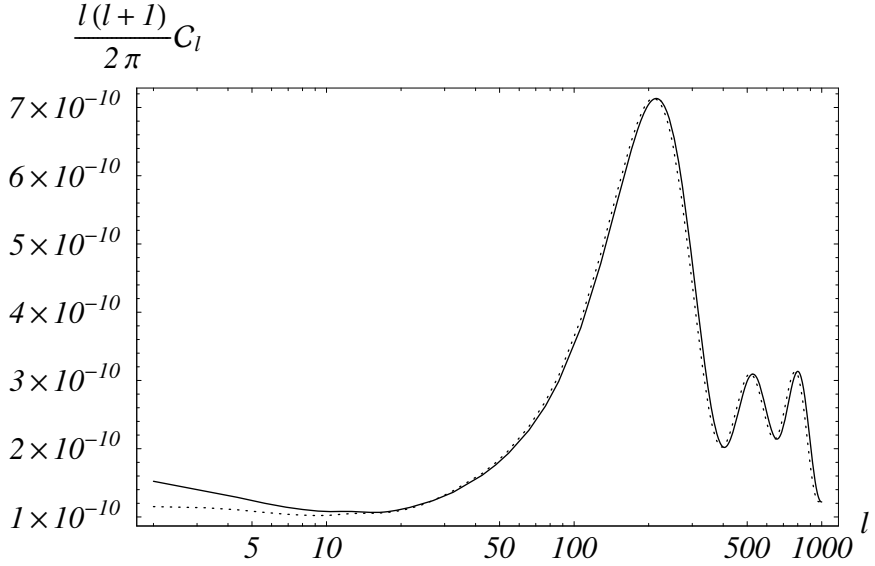

Figure 5.5: Effects of varying w_0 on CMB power spectrum. The two models differ only on the value of the present value of the equation of state, assumed constant in time, being $w_0 = -1$ (solid line) and $w_0 = -0.8$ (dotted line); the other parameters are fixed to the concordance model of Fig. 3.3. The two power spectra are normalized to the first acoustic peak, which is essentially equivalent to fix the primordial power.

5.4 Present constraints on the equation of state

Measures of the Quintessence equation of state come mainly from CMB, SNIa and LSS. In this Section we review the main effects of the dark energy on CMB and LSS, and the existing constraints. For $w > -1$, the Quintessence geometrically reduces the distances with respect to the Cosmological Constant. The comoving distance to the last scattering surface, located at redshift $z_{ls} \simeq 1100$ depends on the Quintessence parameters through the relation

$$r\,(z_{ls}) = H_0^{-1} \int_0^{z_{ls}} \frac{dz}{\sqrt{\Omega_m(1+z)^3 + \Omega_V(1+z)^{3(1+w_0)}}}\ , \tag{5.36}$$

where for simplicity we assumed $w = w_0$ constant; $r\,(z_{ls})$ is clearly reduced when w_0 moves from -1 to higher values. The displacement of the last scattering surface shifts all the acoustic features in the CMB power spectrum toward lower multipoles that correspond to larger angular scales in the sky. This projection clearly affects all the cosmological objects in the Universe including the LSS. A different mechanism modifies the late ISW effect on the CMB power spectrum at low multipoles ($l < 10$) produced by the low redshift ($z < 10$)

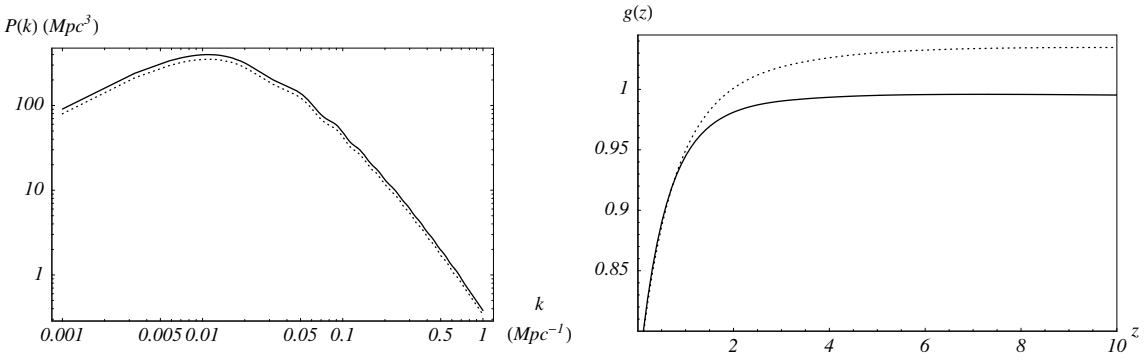

Figure 5.6: Effects of varying w_0 on present matter power spectrum, normalized to the same primordial amplitude on large scales (left panel), and on the growth factor of linear perturbations, normalized to the same value at present (right panel). The underlying cosmology is fixed by the model described in the text, the same as Fig. 5.5, and the dark energy is modeled with a Cosmological Constant (solid line) and a Quintessence with present equation of state fixed to $w_0 = -0.8$.

dynamics of the gravitational potentials. For $w > -1$, the changing in the cosmic equation of state begins at higher redshifts with respect to the Cosmological Constant case. This increases the gravitational potential dynamics, and the ISW is consequently stronger. In Fig. 5.5 we show the effects of varying w_0 on the CMB power spectrum.

The influence of the Quintessence on the LSS is reflected into the mass power spectrum. Both in the Cosmological Constant and the Quintessence model the perturbation growth is inhibited by the domination of the dark energy at low redshift. In fact the presence of a dark energy component makes larger the Hubble parameter $H(z)$ that acts as a friction term in the cosmological perturbation equations involving the first time-derivatives of the perturbations. Consequently, Quintessence and Cosmological Constant lead to different growth of density perturbations. Therefore, normalizing to the same power in the early Universe, we have a lower mass power spectrum in Quintessence models compared to that of a Cosmological Constant, because $H(z)$ is bigger. The effect of varying w_0 on the matter power spectrum is shown in the left panel of Fig. 5.6; while in the right panel we plot the growth factor, normalized to the same value at present.

To measure the dark energy equation of state we can cross correlate the information enclosed in the CMB power spectrum, in the mass power spectrum of the LSS and in SNIa data. At the present the constraints on the equation of state have been derived from the

	w_0	Dataset
Spergel *et al.* (2003)	$w_0 = -0.98 \pm 0.12$	WMAPext+2DF
Tegmark *et al.* (2004)	$w_0 = -1.05^{+0.13}_{-0.14}$	WMAP+SDSS
Sanchez *et al.* (2005)	$w_0 = -0.85^{+0.18}_{-0.17}$	WMAPext+VSA+2DF
Mac Tavish *et al.* (2005)	$w_0 = -0.94^{+0.094}_{-0.096}$	WMAPext+VSA+B03+2DF+SDSS

Table 5.1: Summary of the most recent measures of the present value of the dark energy equation of state. In all dataset SNIa are included (See references in first column for further details).

CMB (mainly with the projection effect as the ISW is dominated by the cosmic variance) and LSS. The CMB data come from WMAP+CBI+ACBAR (WMAPext, Spergel *et al.* 2003), and the three-dimensional power spectrum from over 2×10^5 galaxies from the Sloan Digital Sky Survey (SDSS, Tegmark *et al.* 2004a). The analysis assumed a constant equation of state. Combining WMAPext with the 2 Degrees Field (2DF) data Spergel *et al.* (2003) obtain $w_0 < -0.78$ (95 % c.l.), imposing $w_0 > -1$, and $w_0 = -0.98 \pm 0.12$ dropping the prior. On the other hand, the results from Tegmark *et al.* (2004) are $w_0 = -0.72^{+0.34}_{-0.27}$ with only WMAP data, and $w_0 = -1.05^{+0.13}_{-0.14}$ including also SDSS and SNIa data; they varied the baryon density, the dark matter density, the dark energy density, the scalar spectral index, the amplitude of scalar fluctuations, the optical depth and assumed no spatial curvature and no gravitational waves; an additional hypothesis made on the dark energy is that does not cluster (i.e. is homogeneous). Very recently Sanchez *et al.* (2005) obtained $w_0 = -0.87^{+0.12}_{-0.12}$ combining the WMAPext data, the Very Small Array (VSA, Dickinson *et al.* 2004) data, the final 2DF data (Cole *et al.* 2005) and the SNIa data (Riess *et al.* 2004); while the value from Mac Tavish *et al.* (2005) is $w_0 = -0.94^{+0.094}_{-0.096}$ with the same dataset of Sanchez *et al.* (2005) *plus* the BOOMERanG 2003 data (B03) and the SDSS data. In Tab. 5.1 we summarize the main measures of w_0. The effect of dropping the prior on w_0 on the other parameters is similar to those of dropping the flatness assumption. This behavior is easy to understand physically: as we reported above a change in w_0 essentially leads to a shift in the CMB peaks, plus a small modification in the late ISW and a change in the amplitude in the matter power spectrum. The same projection effect is reproduced by the curvature, yielding a degeneracy in the angular diameter distance that can be broken by the late ISW

effect. On the other hand the latter is affected by the cosmic variance.

In conclusion, all the significant constraints obtained so far on the equation of state assumed a constant redshift behavior. On the other hand, if the dark energy were described by such a behavior, the observations are so far consistent with a Cosmological Constant, with a few percent accuracy. The question of the comparison of a realistic, redshift dependence Quintessence equation of state is currently completely open. In the next chapter we shall try to quantify how the knowledge of the CMB three point statistic can improve the previous analysis, considering the weak lensing dependence on w_0, w_∞ and Ω_V; the treatment is based on the analysis carried out in Ch. 4.

Chapter 6

CMB bispectrum and high redshift expansion rate

In the previous chapter we developed the tools necessary to compute and study the CMB anisotropy three-point statistics in the angular domain, in a variety of cosmological models, involving in particular a dynamical dark energy component. We saw how the lensing power, causing a non-Gaussian distortion in the primary CMB image, is injected at an epoch corresponding to the onset of cosmic acceleration and structure formation, being zero earlier and at the present; we therefore expect an enhanced sensitivity of this CMB observable to the cosmic behavior at that epoch, and in particular to the dark energy dynamics. In this chapter we provide a first quantification of such expectation, showing in particular how the knowledge of the CMB bispectrum from lensing, i.e. the three-point anisotropy statistics in the angular domain, can improve a conventional analysis based on the CMB power spectrum in constraining the dark energy dynamics. In Sec. 6.1 we outline the main phenomenology highlighting the complementarity between the two observables; in Sec. 6.2 we evaluate and study the expected signal to noise ratio relative to the bispectrum detection for the present and forthcoming CMB probes; in Sec. 6.3 we make a likelihood analysis for power spectrum, bispectrum and their combination, focused on the dark energy abundance and dynamics.

6.1 Bispectrum vs. power spectrum

The primordial CMB power spectrum and the bispectrum induced by lensing carry complementary information on the cosmological expansion history since they acquire their signal at very different epochs. The dominant power spectrum contribution arises at decoupling, when the Universe becomes transparent to the radiation and the photons last scatter; typically this occurs at redshift $z_{ls} = 1100$ (about 300000 years after the Big Bang). At that epoch, and in most cosmological models, the dark energy contribution to the cosmological expansion rate is negligible. Thus, as we anticipated in the previous chapter, the dark energy affects the CMB power spectrum mainly via a projection shift, since its presence modifies the comoving distances shifting the acoustic peaks:

$$r(z_{ls}) = H_0^{-1} \int_0^{z_{ls}} \frac{dz}{\sqrt{\Omega_m (1+z)^3 + \Omega_V e^{f(z)}}} \,, \tag{6.1}$$

where

$$f(z) = 3 \int_0^z dz' \frac{1 + w(z')}{1 + z'} \,. \tag{6.2}$$

In models with $w(z) > -1$, the distance to the last scattering is reduced. Since the physical scales associated with the acoustic oscillations do not depends on the dark energy, as we stressed above, the contraction of $r(z_{ls})$ results in a shift of the acoustic peaks toward smaller multipoles, i.e. larger angles. We made this argument clear in Sec. 5.4, but here in addition we see how the redshift dependence of w on z is washed out by two integrals. This clearly makes problematic the study the dark energy dynamics with the CMB power spectrum only. Such analysis is also affected by a degeneracy between dark energy equation of state and dark energy abundance, i.e. combinations of Ω_V and equation of state keeping $r(z_{ls})$ constant; such degeneracy becomes worse when we take into account the dark energy dynamics.

On the other hand the bispectrum signal arises when the dark energy starts to influence the cosmic expansion, as shown in Sec. 4.1. To show how the bispectrum breaks the projection degeneracy, we plot in Fig. 6.1 the power spectrum and the equilateral bispectrum for three cosmological models having roughly the same distance to the last scattering surface. The three models differ only for the dark energy parameters Ω_V, w_0

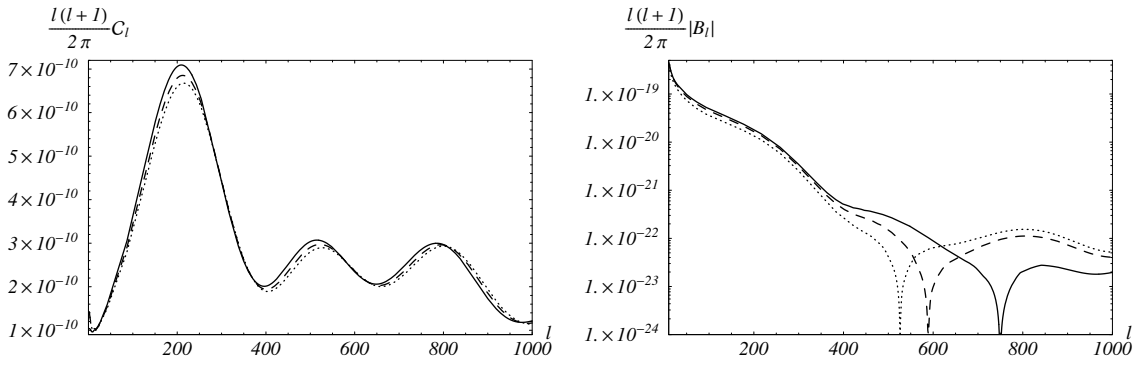

Figure 6.1: Power spectrum (left) and equilateral bispectrum (right) for different dark energy models with approximately the same distance from the last scattering surface. The models are: $\Omega_V = 0.75$, $w_0 = -0.76$ and $w_\infty = -0.76$ (solid line); $\Omega_V = 0.74$, $w_0 = -0.92$ and $w_\infty = -0.80$ (dashed line); $\Omega_V = 0.73$, $w_0 = -1$ and $w_\infty = -1$ (dotted line).

and w_∞ while the other parameters are fixed to concordance model, already used in Ch. 4, and the energy densities of the other components vary with Ω_V in order to keep a flat cosmology. In the power spectra the position of the acoustic peaks remains almost the same independently on the dark energy model; the three curves are almost superposed except for the amplitude of the first acoustic peak, due to the different ISW effect amplitude, and the fact that the curves are normalized to $l = 10$.

The situation is very different looking at the equilateral bispectrum; here the position in multipole of the transition between linear and non-linear regime (the "cusp") in the growth of cosmic structures is shifted by tens of multipoles, as a result of the different growth rate of structures. The amplitude of the bispectrum in the tail powered by the linear regime mainly determines the position of the cusp since the non-linear one exhibits a weaker dependence on the expansion rate: the higher is the power in the linear regime, the higher is the multipole at which the transition from linear to non-linear regime occurs. This behavior can be better understood plotting the linear perturbation growth factor (4.11), normalized to the same value at the present, for the dark energy models of Fig. 6.1, in Fig. 6.2. As we can see, the different dark energy parameters modify the growth factor: for those models in which the growth factor exhibits a larger dynamics, the cusp is shifted at higher multipoles. As is evident, the curve corresponding to the Λ model is sensibly smaller at almost all epoch, while the curve of the dark energy with more dynamics is the highest.

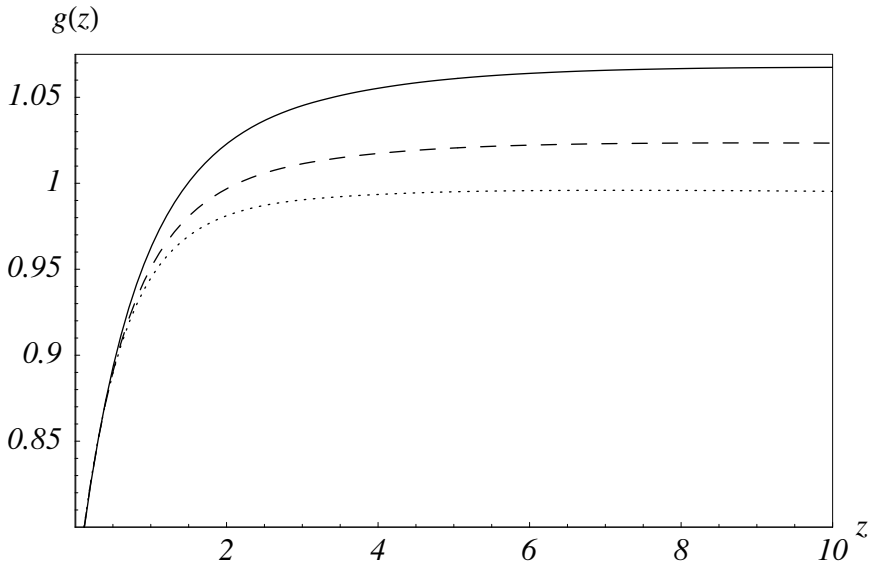

Figure 6.2: Growth factors as function of redshift for the same cosmological models of Fig. 6.1: $\Omega_V = 0.75$, $w_0 = -0.76$ and $w_\infty = -0.76$ (solid); $\Omega_V = 0.74$, $w_0 = -0.92$ and $w_\infty = -0.80$ (dashed); $\Omega_V = 0.73$, $w_0 = -1$ and $w_\infty = -1$. (dotted)

Correspondingly, the change at low redshifts, i.e. when the dark energy starts to dominate the expansion, is stronger in the scenario with a strong time variation of $w(z)$, inducing a larger amplitude for the derivative factor $F(l, z) > 0$ tail in the line of sight integral (4.28), and pushing the dominance of the linear power in the curves in Fig. 6.1 to smaller scales (Giovi, Baccigalupi & Perrotta 2003). To have a better insight in this central aspect, in Fig. 6.3 we plot the hypersurfaces of equal distance to the last scattering surface (left panel) and those of equal position of the cusp of the equilateral bispectrum in the multipole space (right panel) in the space of the dark energy parameters considered here. As we can see, the distance degeneracy produces hypersurfaces almost flat and orthogonal to the Ω_V direction; this dependence is very clear looking at the expression (6.1), in which the dynamics of the dark energy is washed out by two integrals, as we already stressed. The variation of the dark energy abundance simply shifts the hypersurface of equal distance. On the other hand, the degeneracy in the cusp position is more complex to interpret because, as we have seen above, the dark energy parameters enter in the computation of the bispectrum in several ways, from geometry and perturbations. What matters here is that the hypersurfaces are clearly misaligned, making them complementary for dark energy studies.

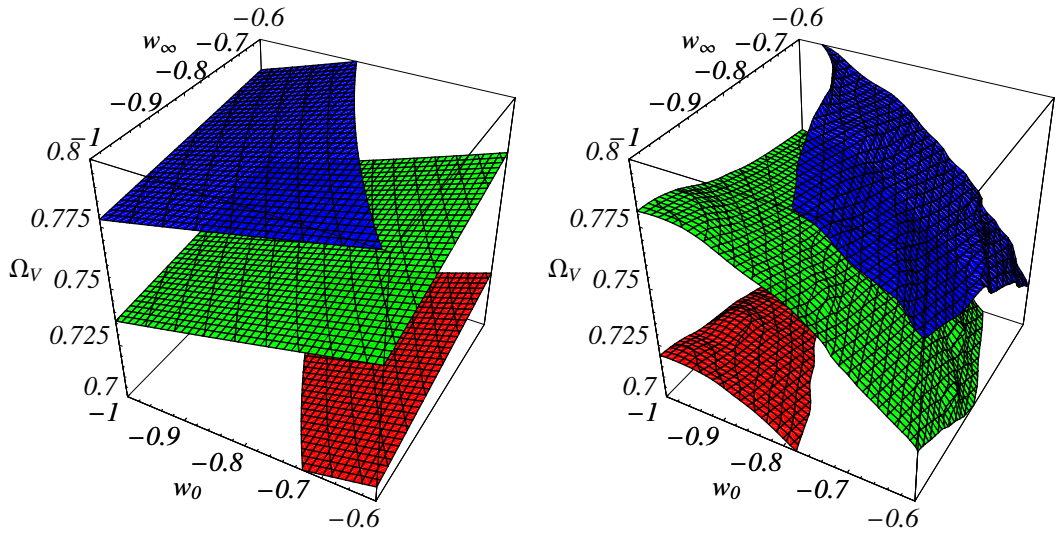

Figure 6.3: Left panel: hypersurfaces of equal distance to the last scattering surface. Right panel: hypersurfaces of equal cusp position in the multipole space.

6.2 Bispectrum's signal to noise ratio

We have shown how the equilateral bispectrum possesses promising properties which may reduce the projection degeneracy that affects the power spectrum when studying the dark energy. Of course in real observations the bispectrum is a noisy observable, polluted by cosmic variance even before the instrumental noise. Indeed, even for a perfect Gaussian statistics, the CMB sky is a realization of that, featuring a residual *rms* power also where the average is expected to be zero, such as in the CMB anisotropy three point power. On the other hand, just like for the ordinary CMB power spectrum, such uncertainty may be predicted in detail, as we show here. In this section we want to evaluate the signal to noise ratio of the bispectrum in the general case. We need to write the expression of the noise for the bispectrum, i.e. the covariance matrix of $B_{l_1 l_2 l_3}$ (Luo 1994; Heavens 1998; Gangui & Martin 2000a). Recalling the formalism developed in Ch. 4, the covariance matrix of (4.20) is

$$\left\langle B_{l_1 l_2 l_3} B_{l'_1 l'_2 l'_3} \right\rangle =$$
$$= \sum_{mm'} \begin{pmatrix} l_1 & l_2 & l_3 \\ m_1 & m_2 & m_3 \end{pmatrix} \begin{pmatrix} l'_1 & l'_2 & l'_3 \\ m'_1 & m'_2 & m'_3 \end{pmatrix} \left\langle a_{l_1 m_1} a_{l_2 m_2} a_{l_3 m_3} a^*_{l'_1 m'_1} a^*_{l'_2 m'_2} a^*_{l'_3 m'_3} \right\rangle =$$

$$= C_{l_1} C_{l_2} C_{l_3} \left[\delta_{l_1}^{l_1'} \delta_{l_2}^{l_2'} \delta_{l_3}^{l_3'} + \delta_{l_1}^{l_3'} \delta_{l_2}^{l_1'} \delta_{l_3}^{l_2'} + \delta_{l_1}^{l_2'} \delta_{l_2}^{l_3'} \delta_{l_3}^{l_1'} + \right. \tag{6.3}$$
$$\left. + (-1)^{l_1+l_2+l_3} \left(\delta_{l_1}^{l_1'} \delta_{l_2}^{l_3'} \delta_{l_3}^{l_2'} + \delta_{l_1}^{l_2'} \delta_{l_2}^{l_1'} \delta_{l_3}^{l_3'} + \delta_{l_1}^{l_3'} \delta_{l_2}^{l_2'} \delta_{l_3}^{l_1'} \right) \right] \ ,$$

where $\delta_{l_i}^{l_j}$ is the Kronecker's Delta. We also assumed a weak non-Gaussianity, so that the coupling between different scales is small, making the off-diagonal terms vanishing and the covariance matrix is diagonal. For $l_1 + l_2 + l_3 =$ even the bispectrum variance is written in terms of the power spectrum C_l as

$$\left(\sigma^B_{l_1 l_2 l_3}\right)^2 = n_{l_1 l_2 l_3} C_{l_1} C_{l_2} C_{l_3} \ , \tag{6.4}$$

where $n_{l_1 l_2 l_3}$ is defined as:

$$n_{l_1 l_2 l_3} = \left(1 + \delta_{l_1}^{l_2} + \delta_{l_2}^{l_3} + \delta_{l_3}^{l_1} + 2\delta_{l_1}^{l_2} \delta_{l_2}^{l_3} \right) \ . \tag{6.5}$$

The bispectrum variance depends on the triangular configuration, indeed the factor $n_{l_1 l_2 l_3}$ takes the value 1 if all the multipoles are different, 2 if two multipoles are equal and 6 if the three multipoles are all equal. This means that when we explore the l space with equilateral triangles the bispectrum variance is amplified by a factor 6 with respect the scalene triangles; if we use isosceles triangles the amplification reduces to a factor 2.

We are now able to estimate the bispectrum variance. First of all we assume an ideal experiment with full sky coverage, so that the only source of error is the cosmic variance $\left(\sigma^B_{l_1 l_2 l_3}\right)^2$; later we shall consider the instrumental noise. It is important to note that the single bispectrum coefficients are usually dominated by the cosmic variance. To give an idea of the magnitude of the signal we are studying, with respect to the case of the power spectrum, at $l \approx 200$ the value of the bispectrum is of the order of $B_l \approx 10^{-21}$ whereas the error (including only the cosmic variance) is of the order of $C_l^{3/2} \approx 10^{-19}$. At higher multipoles it gets worse. The situation changes remarkably if we consider the whole set of triangles (equilateral, isosceles and scalene), increasing the statistics and making the bispectrum detectable; to show that we consider the signal to noise ratio (Hu 2000 and references therein):

$$\left(\frac{S}{N} \right)^2 = \sum_{l_1, l_2, l_3 = l_{\min}}^{l_{\max}} \frac{B^2_{l_1 l_2 l_3}}{n_{l_1 l_2 l_3} C_{l_1} C_{l_2} C_{l_3}} \ . \tag{6.6}$$

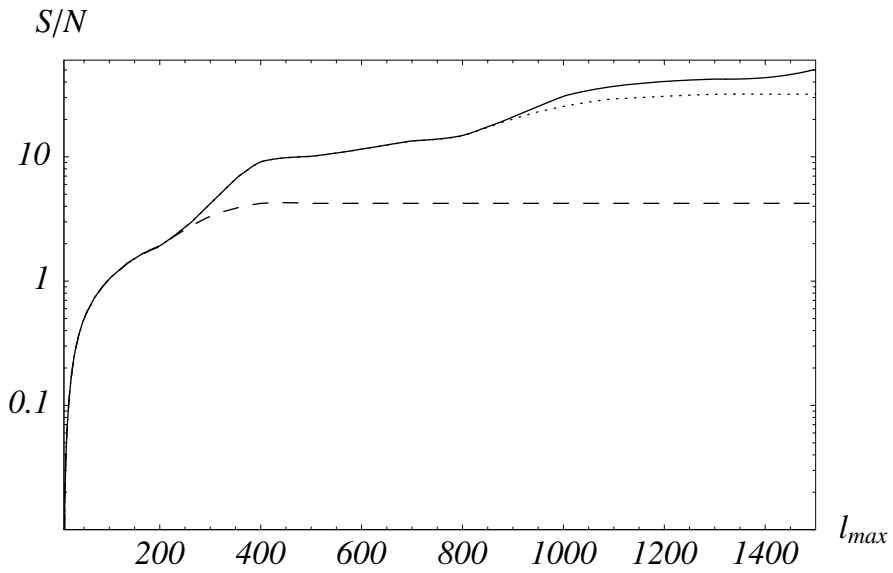

Figure 6.4: Bispectrum signal to noise ratio as function of $l_{\max}$ for a cosmic variance experiment (solid line), Planck nominal noise (dotted line) and two years WMAP nominal noise (dashed line). The cosmology corresponds to a model with $\Omega_V = 0.73$, $w_0 = -1$ and $w_\infty = -0.8$; the other parameters are fixed accordingly to the cosmic concordance model.

According to the approximation made in Ch. 4 in order to evaluate $B_{l_1 l_2 l_3}$, we adopt the lower limit $l_{\min} = 10$ in the sum above. The expression (6.6) includes the contributions from all multipole configurations. The equilateral ones account for $l_{\max}$ terms, which is just a small fraction of all the $l_{\max}^3$ terms; this makes clear how the scalene configurations represent the bulk of the bispectrum power.

In Fig. 6.4 we plot the signal to noise ratio as function of $l_{\max}$ up to $l_{\max} = 1500$ for three cases: cosmic variance only, Planck nominal noise and two years WMAP nominal noise, see Tab. 6.1. We don't take into account systematics and foregrounds and a full sky coverage is assumed; while those issues are more or less under control when measuring the CMB spectrum power, since the bispectrum signal is second order, it is natural to expect enhanced challenges for its measure. Some preliminary considerations on this issue shall be discussed in the next chapter. For comparison to (6.6), the nominal noise on the single power spectrum coefficient for a multichannel experiment is given by

$$(\Delta C_l)^2 \approx \frac{2}{2l+1}\left(C_l + \frac{1}{w_{tot} B_l^2}\right)^2 , \tag{6.7}$$

	WMAP			Planck (LFI)		Planck (HFI)			
ν_c (GHz)	40	60	90	44	70	100	143	217	353
θ_c(")	31.8	21	13.8	24	14	9.2	7.1	5.0	5.0
$\sigma_c(\times 10^{-6})$	4.1	9.4	21.8	2.7	4.7	2.0	2.2	4.8	14.7

Table 6.1: Experimental Parameter for WMAP and Planck. From Balbi *et al.* (2003).

where $w_{tot} \equiv \sum_{c=1}^{N} w_c \equiv \sum_{c=1}^{N} (\sigma_c \theta_c)^{-2}$ and $B_l \equiv \sum_{c=1}^{N} B_{c,l}^2 (w_c/w_{tot})$ being N the number of channels c, σ_c the average sensitivity per pixel, θ_c the FWHM angular resolution and $B_{c,l}$ the Gaussian beam response (see Balbi *et al.* 2003 and references therein). The specification of the main parameters in (6.7) are tabled into Tab. 6.1 for the WMAP and Planck experiments. Since the single bispectrum coefficient has a very low amplitude, we need to sum up all the signal in order to achieve as a signal to noise ratio larger than 1. In this discussion we adopted a cosmological model with $\Omega_V = 0.73$, $w_0 = -1$ and $w_\infty = -0.8$, the other cosmological parameters are set to our concordance model already used in Ch. 4. The behavior of the signal to noise ratio for Planck and WMAP is qualitatively the same: first the S/N rises, then it reaches a plateau. The plateau means that adding terms in the sum no extra information is gained as the signal vanishes below the cosmic variance and the instrumental noise. The multipole at which the plateau is reached is $l_p \simeq 400$ for WMAP and $l_p \simeq 1000$ for Planck. In the following we restrict our analysis including only the cosmic variance and probing the bispectrum up to $l_{\max} = 1000$; as shown in Fig. 6.4 these results are therefore representative of an experiment with the nominal performance of Planck.

The signal to noise ratio (6.6) is a total compression of the bispectrum's signal and is useful to investigate its detectability, but lacks the information of how the signal is distributed in l. A one-dimensional quantity which contains the contributions from all the possible configurations, but marginalizes over two of the three multipoles, is

$$B_{l_1} = \sum_{l_2, l_3 = l_{\min}}^{l_{\max}} B_{l_1 l_2 l_3} \ , \tag{6.8}$$

where we take $l_{\min} = 10$ and $l_{\max} = 1000$ above; B_{l_1} is an indicator of the multipoles from which the bispectrum takes its power. In Fig. 6.5 we plot B_{l_1}, and we see that the bispectrum receives most of its contributions at multipoles between 200 and 400. This

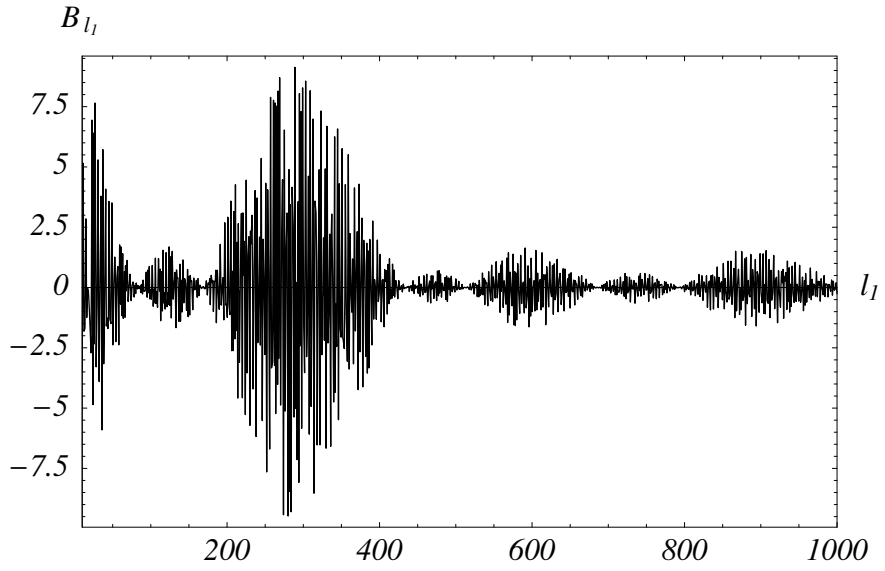

Figure 6.5: Bispectrum in units of 10^{-20} as a function of l_1 only, obtained by marginalization over l_2 and l_3; the cosmological model used is the same of Fig. 6.4. The small scale, positive and negative oscillations are due to the Wigner's 3J symbols; the large scale modulation is a physical feature related to the primordial acoustic peaks.

region is close to the maximum primordial power in the first acoustic peak, consistently with previous analysis (Spergel & Goldberg 1999). The remaining part of the signal is made of a relevant part at low multipoles, probably due to the rise of the overall bispectrum power (see Fig. 4.10), plus a series of oscillations with varying amplitudes. The latter may be related to the series of peaks in the primordial power spectrum. Finally, the positive and negative high frequency oscillations are entirely due to the behavior of the 3J Wigner symbols.

6.3 The impact of the bispectrum coefficients on the cosmological parameter estimation

We now discuss how the bispectrum improves the CMB sensitivity to the high redshift behavior of the dark energy with respect the power spectrum alone. As we already stressed, the power spectrum suffers the degeneracy of the comoving distance to the last scattering surface relatively to different values of the dark energy parameters. On the other hand the CMB bispectrum from weak lensing receives the relevant contribution at structure

formation, probing the dark energy behavior at that epoch (Giovi, Baccigalupi & Perrotta 2003), and we do expect a benefit from the combination of the two observables. We evaluate such benefit by means of a likelihood analysis on simulated data, which we describe here.

Due to a considerable computational difficulty in evaluating the bispectrum for all coefficients and in different cosmological models, most of the cosmological parameters are fixed according to the cosmological concordance model; we shall perform only a variation of the dark energy parameters Ω_V, w_0 and w_∞, which allows us to build a grid of C_l and Q_l values. Then, spanning over our parameter space, we calculate the bispectrum by mean of the relation (4.21). Once we have that as a function of Ω_V, w_0 and w_∞, we compute a three parameters likelihood both for the power spectrum and for the bispectrum; the combined analysis is simply obtained by multiplying the two of them. Our fiducial model has $\Omega_V = 0.73$, $w_0 = -1$ and $w_\infty = -0.8$; the other cosmological parameters are set to the values of the concordance model already used in the previous chapters, see the beginning of Ch. 4. Specifically, we evaluate the likelihood as usual as

$$\mathcal{L}_{s,b} = A_{s,b} \exp\left(-\frac{\chi^2_{s,b}}{2}\right) , \tag{6.9}$$

where the subscripts refer, respectively, to the power spectrum (s) and to the bispectrum (b), $A_{s,b}$ are normalization factors and $\chi^2_{s,b}$ are functions of the dark energy parameters defined as

$$\chi^2_s = \sum_{l=2}^{1000} \left[\frac{C^t_l - C^f_l}{\sigma^s_l}\right]^2 , \tag{6.10}$$

$$\chi^2_b = \sum_{l_1,l_2,l_3=10}^{1000} \left[\frac{B^t_{l_1 l_2 l_3} - B^f_{l_1 l_2 l_3}}{\sigma^b_{l_1 l_2 l_3}}\right]^2 . \tag{6.11}$$

In the expression above, we describe spectrum and bispectrum as Gaussian variables (Gangui & Martin 2000a; Takada & Jain 2004): that corresponds to ignore the possible non-Gaussianity arising in the early Universe, as well as to assume a Gaussian distribution for the bispectrum coefficients, exploiting the argument which states that in the case of weak lensing the signal is caused by many independent events. The superscript t refers to the theoretical model, while f refers to our fiducial model. As we already mentioned, we limit

our analysis to multipoles smaller than 1000, being consistent with a Planck-like experiment with nominal performance (see Fig. 6.4). The expression of the cosmic variance is $(\sigma_l^s)^2 = 2/(2l+1)C_l^2$ for the power spectrum and $(\sigma^b_{l_1 l_2 l_3})^2 = n_{l_1 l_2 l_3} C_{l_1} C_{l_2} C_{l_3}$ for the bispectrum, where $n_{l_1 l_2 l_3}$ is given by Eq. (6.5). We also neglect the correlation between the two observables as it is induced by higher order statistics (Takada & Jain 2004), which allows us to write down the combined likelihood simply as

$$\mathcal{L}_c = \mathcal{L}_s \mathcal{L}_b = A_c \exp\left(-\frac{\chi_s^2 + \chi_b^2}{2}\right) , \tag{6.12}$$

where A_c normalizes it.

We report the results of our likelihood analysis in three main cases, with one, two and three free parameters. As we show later this approach is necessary to understand how different the basins of degeneracy of spectrum and bispectrum are, and the benefit from their combination. We use the following priors: $0 \leq \Omega_V \leq 1$, $-1 \leq w_0 \leq -0.6$, $-1 \leq w_\infty \leq -0.6$. When Ω_V varies, the matter abundance is changed in order to keep flatness and leaving $\Omega_b h^2$ unchanged.

The simpler case is when two of the three dark energy parameters are fixed to their fiducial values, while the third one is allowed to vary. In that case, regardless of which parameter varies, the bispectrum doesn't improve the basic analysis on the power spectrum alone. The reason is simply the reduced signal to noise ratio of the bispectrum. When just one parameter varies, even w_∞, the tiny changes in the power spectrum signal dominate the exponential in the combined likelihood; note that when w_∞ varies, the relative changes in the bispectrum are stronger than in the power spectrum case (Giovi, Baccigalupi & Perrotta 2003, 2005). However, when the cosmic variance is taken into account, such advantage is canceled and the joint likelihood is almost identical to $\mathcal{L}_s$. As we shall see in the following, the results change greatly when a multi-dimensional analysis is performed. The reason is that the basins of degeneracy of spectrum and bispectrum open in markedly different ways, making their combination advantageous, as we see already in the two dimensional analysis below.

Let's begin by fixing $\Omega_V = 0.73$; though the power spectrum likelihood is very narrow (see Fig. 6.6, first row, left panel), it is degenerate along a specific direction, where

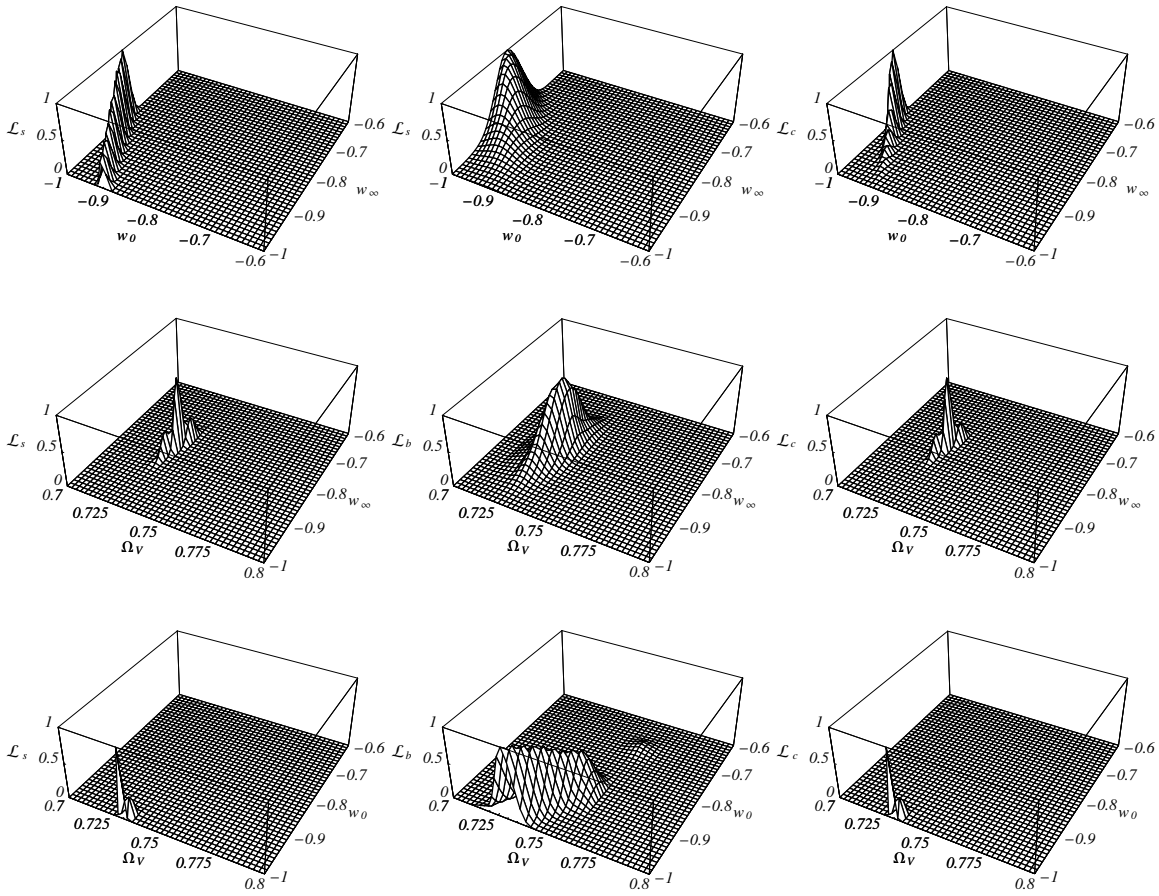

Figure 6.6: First row: likelihoods as function of w_0 and w_∞ with $\Omega_V = 0.73$. Second row: likelihoods as function of Ω_V and w_∞ with $w_0 = -1$. Third row: likelihoods as function of Ω_V and w_0 with $w_\infty = -0.8$. From left to right: power spectrum only, bispectrum only and their combination.

different values of w_0 and w_∞ produce similar values of the function $e^{f(z)}$ in Eq. (6.1) at the epoch of the structure formation. For this reason, the power spectrum is able to exclude a wide region of the parameter space, but is unable to constrain w_0 and w_∞ separately. The bispectrum likelihood is non-zero over a wider region of the parameter space, but vanishes on the region where the power spectrum is degenerate (Fig. 6.6, first row, center panel); while the projection degeneracy affecting the power spectrum is well understood, it is more difficult to track the dark energy variables in the bispectrum calculation, as they enter in several aspects, i.e. distances and perturbation growth. The only clear feature is

the vanishing of the lensing power at present and infinity (Giovi, Baccigalupi & Perrotta 2003), making the bispectrum sensitive to w_0 and to w_∞, in different ways. As a result, the degeneracy basins of spectrum and bispectrum are misaligned, allowing the separate measure of w_0 and w_∞ from their combination (Fig. 6.6, first row, right panel). In the second and third row of Fig. 6.6 we set w_0 and w_∞ to their fiducial values respectively. The situation is very different with respect to fixing Ω_V. We have a slight improvement when w_0 is fixed whereas fixing w_∞ that disappears. This is due to the constraining capability of the CMB power spectrum when only two parameters vary, similarly to the one dimensional likelihood case. We may notice that the bispectrum is more degenerate with respect to the dark energy abundance than on the equation of state. On the other hand the power spectrum has an opposite behavior. Summarizing, in two of the three cases of the two parameters likelihood analysis, the power spectrum constraints are still stronger except one, in which the dark energy abundance is fixed. We shall give a more exhaustive explanation of this behavior in the following discussion where all the three dark energy parameters are allowed to vary.

In Fig. 6.7, 6.8 and 6.9 we plot the three parameters likelihoods marginalized respectively over Ω_V, w_0 and w_∞; in each figure, the top-left panel is the power spectrum likelihood, the top-right panel is the bispectrum likelihood, the bottom-left panel is the combined likelihood and in the bottom-right panel we put the contour plots at 2σ and 1σ confidence levels for the power spectrum likelihood and the combined one. As expected, when marginalizing over Ω_V, the likelihood analysis gives almost the same result as when Ω_V is fixed (see above). Indeed, the leading feature is the projection degeneracy in the CMB power spectrum with respect to the combined variation of w_0 and w_∞; the latter gets worse when also Ω_V varies, although that variation affects also the matter abundance inducing relevant changes in the power spectrum; the resulting picture is therefore almost equivalent to the case when Ω_V is fixed. However, the three parameters case is different with respect to the previous one when the marginalization is performed over w_0 or w_∞. In the previous discussion we saw that when w_0 or w_∞ is fixed, the power spectrum constraints dominate the joint likelihood. As we have shown, having one of the two dark energy equation of state parameters fixed means breaking the projection degeneracy for the power spectrum,

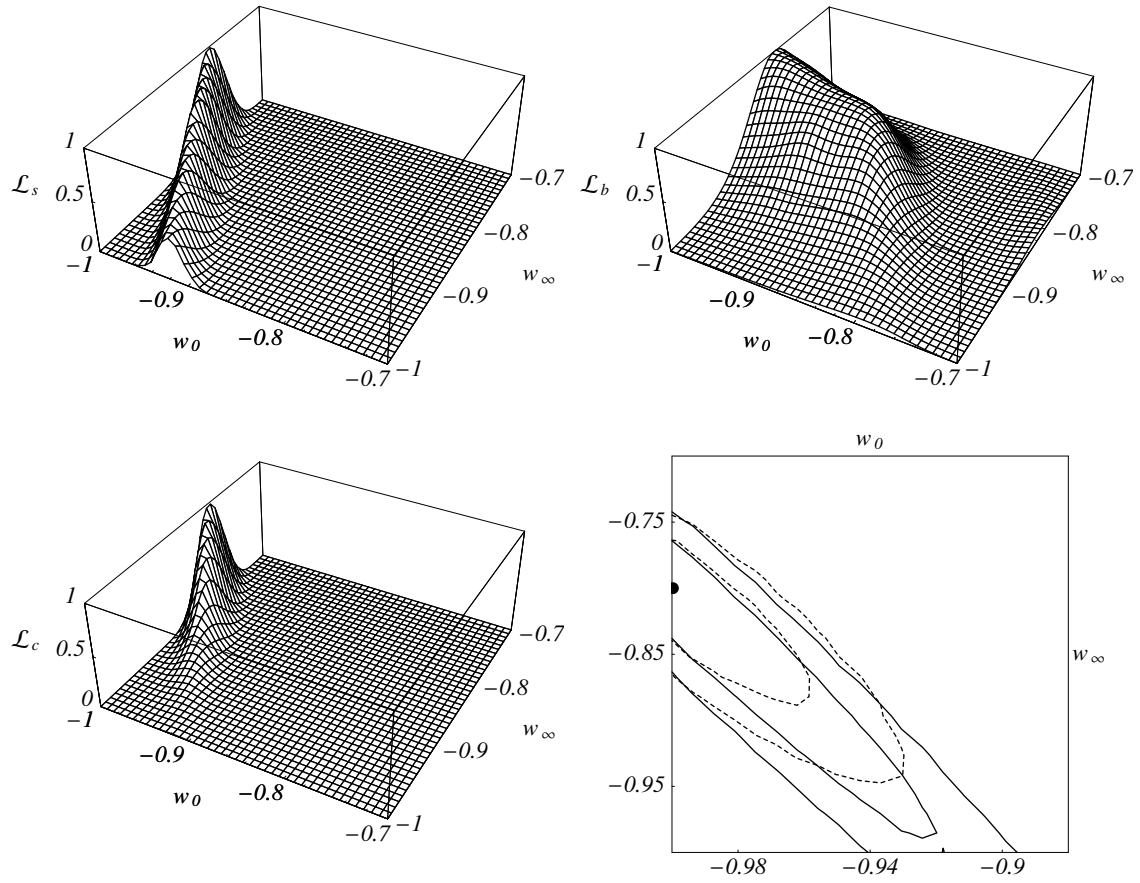

Figure 6.7: Likelihood marginalized over Ω_V for the power spectrum only (top-left), bispectrum only (top-right) and both (bottom-left). In the bottom-right panel we plot the contour levels at 1σ (innermost contours) and 2σ (outermost contours) for the power spectrum by itself (solid line) and combined with the bispectrum (dashed line), the dot is our fiducial model.

when also Ω_V varies. In the present case the latter argument disappears, and the power spectrum constraints are still fully affected by that degeneracy, causing the visible gain from having the bispectrum into the analysis. Note that the bispectrum likelihood in the top right panel of Fig. 6.7 is sharper in the w_∞ axis, showing how the bispectrum is more sensitive to the properties of dark energy at structure formation. The top panels of Fig. 6.8, obtained marginalizing over w_0, reveal two different weaknesses of spectrum and bispectrum, which make their combination fruitful. First, the weak sensitivity of the power spectrum to w_∞: the likelihood is almost flat for a long line in the w_∞ direction, until the latter

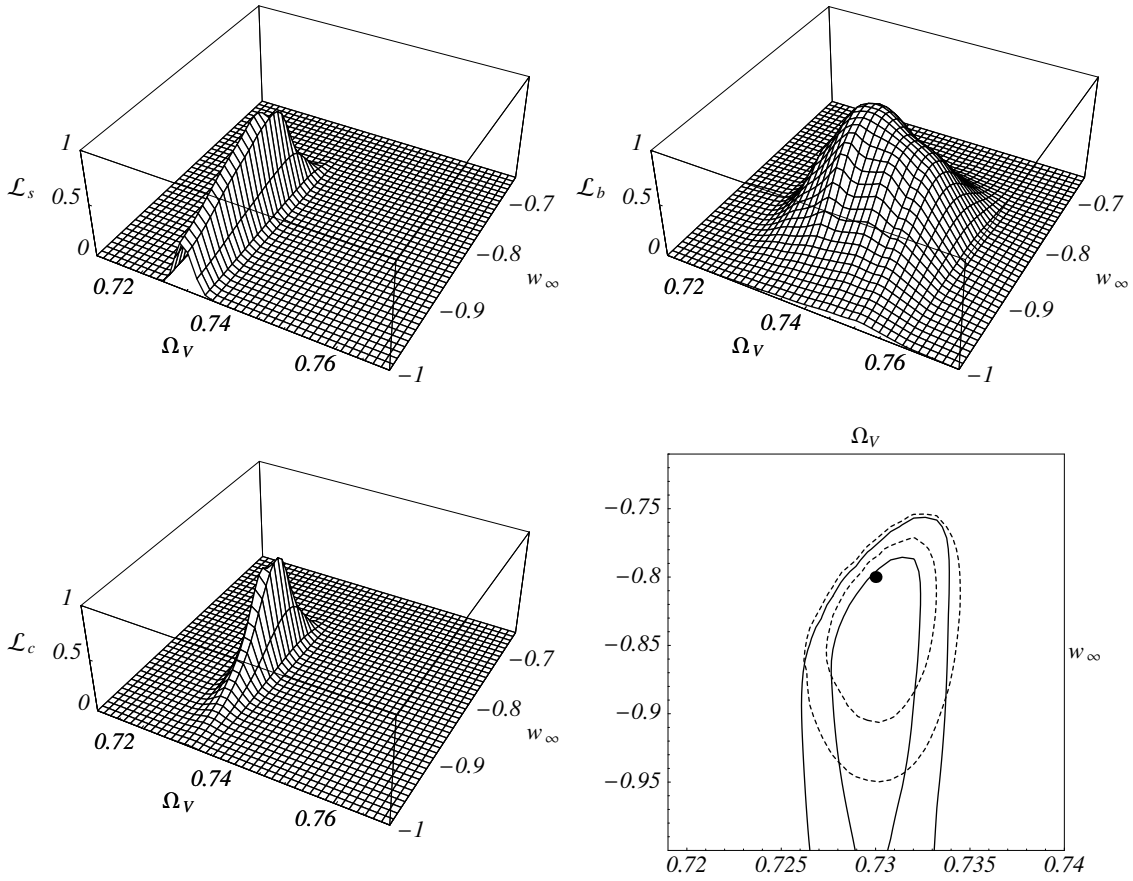

Figure 6.8: As in Fig. 6.7 but with marginalization over w_0.

parameter induces a change strong enough to let the likelihood vanishing. On the other hand, the sensitivity to Ω_V is strong as its variation affects the matter abundance, inducing important changes in the power spectrum shape. The opposite happens for the bispectrum. Now the preferred parameter is w_∞, as it determines the dark energy behavior at the time when the lensing power is injected. This orthogonality in the degeneracy direction of spectrum and bispectrum determines the relevant advantage of their combination, clearly visible in the bottom panels of Fig. 6.8. The minimum gain is got in the case of Fig. 6.9, where the marginalization is performed over w_∞. Indeed, the latter operation washes out the parameter of greatest importance for the bispectrum; in the top right panel, the bispectrum degeneracy direction roughly corresponds to the constancy of the dark energy

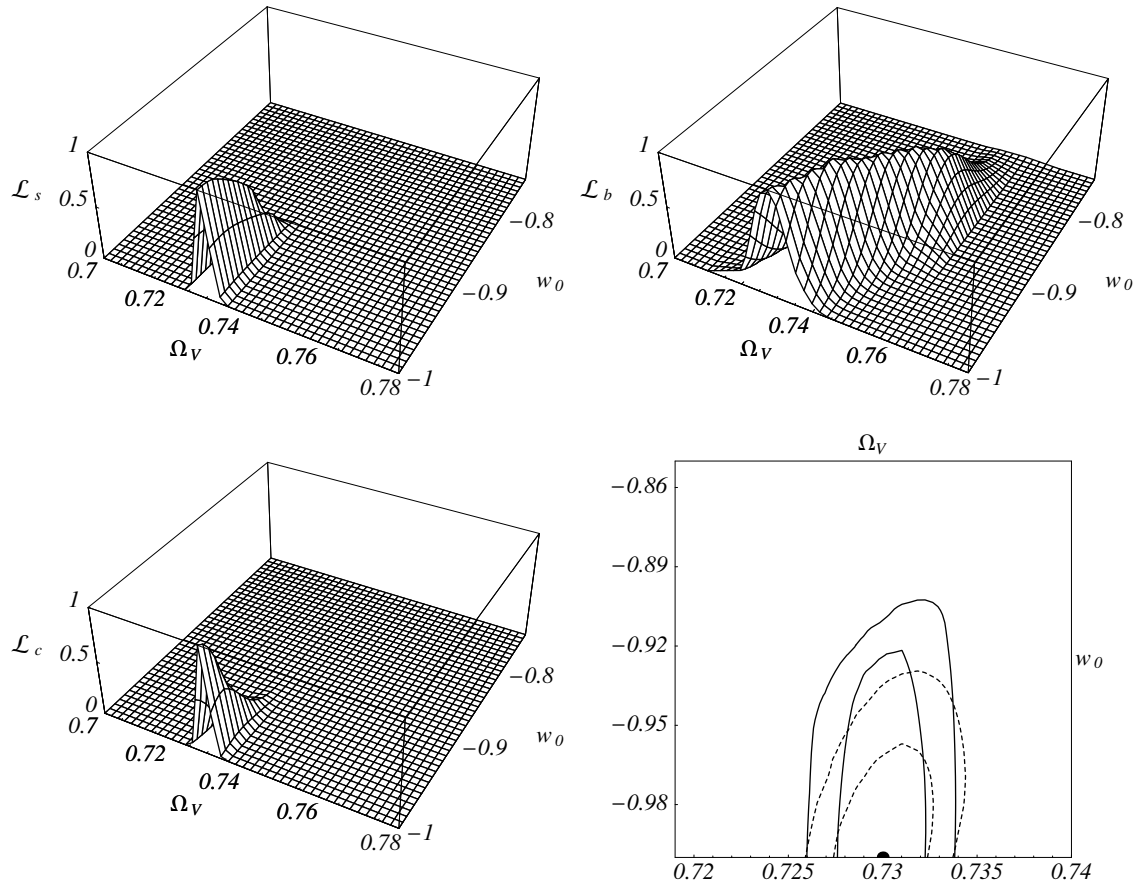

Figure 6.9: As in Fig. 6.7 but with marginalization over w_∞.

abundance at the time in which the lensing injects its power. On the other hand, as we stressed above, the gain is still relevant and visible in the bottom panels of Fig. 6.9, as the three parameters analysis makes the power spectrum projection degeneracy fully effective.

In Fig. 6.10 we give a qualitative picture of the different likelihood shapes for spectrum and bispectrum, in the three parameters analysis, where one has been marginalized. The solid and dashed lines represent the power spectrum and bispectrum likelihoods, respectively; they are normalized to their maximum values and the five contours for each observable are equally spaced between 0 and 1 to highlight their shape. In all cases the two likelihoods are misaligned and that is evident in particular when we marginalize on w_0, so that the power spectrum and the bispectrum add different informations to the joint

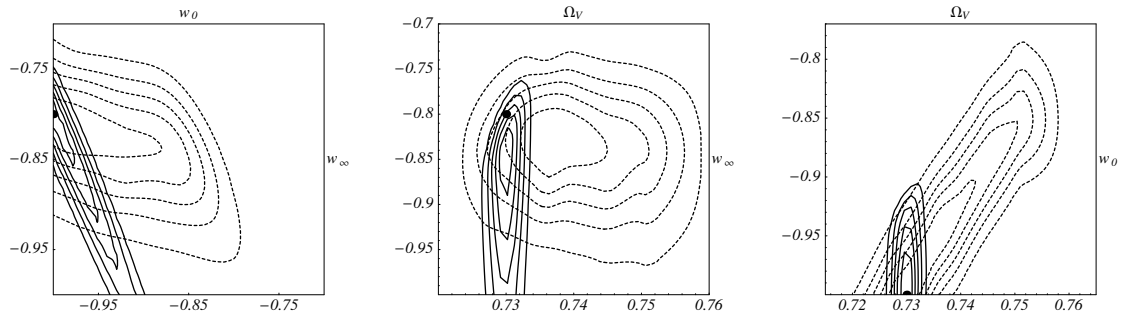

Figure 6.10: Contour levels for the three parameters analysis, where one has been marginalized; the solid and dashed lines represent the power spectrum and bispectrum likelihoods, respectively; they are normalized to their maximum values and the five contours for each observable are equally spaced between 0 and 1 showing qualitatively the different basins of degeneracy. From left to right: marginalization over Ω_V, w_0 and w_∞.

1σ c.l.	Ω_V	w_0	w_∞
Power spectrum	$0.728 \leq \Omega_V \leq 0.732$	$w_0 \leq -0.95$	$-0.94 \leq w_\infty \leq -0.81$
Bispectrum	$0.731 \leq \Omega_V \leq 0.750$	$w_0 \leq -0.89$	$-0.89 \leq w_\infty \leq -0.78$
Combined	$0.729 \leq \Omega_V \leq 0.732$	$w_0 \leq -0.97$	$-0.87 \leq w_\infty \leq -0.80$
2σ c.l.	Ω_V	w_0	w_∞
Power spectrum	$0.727 \leq \Omega_V \leq 0.734$	$w_0 \leq -0.92$	$w_\infty \leq -0.79$
Bispectrum	$0.724 \leq \Omega_V \leq 0.759$	$w_0 \leq -0.79$	$-0.96 \leq w_\infty \leq -0.74$
Combined	$0.727 \leq \Omega_V \leq 0.734$	$w_0 \leq -0.94$	$-0.93 \leq w_\infty \leq -0.77$

Table 6.2: Confidence level at 1σ and 2σ of the three parameters likelihood study, marginalized over two of them.

likelihood.

Finally, to quantify how the bispectrum analysis improves the estimation of the dark energy parameters, we report in Tab. 6.2 the constraints (both at 1σ and 2σ) on our parameters, obtained when the power spectrum, bispectrum and the combined analysis are applied to our fiducial model. This table refers to the three parameter likelihoods, marginalized over the remaining two of them. As discussed, the confidence levels are always narrower when the bispectrum analysis is added to the power spectrum one. Roughly, the precision on the measures of w_0 and w_∞ is percent and ten percent, respectively.

We close here this chapter, leaving the summary and other remarks to the concluding one.

Chapter 7

Problems, future perspectives and concluding remarks

In this thesis we studied the three point CMB statistics induced by weak lensing of the primordial anisotropies by forming cosmological structures. We studied the lensing power injection in the angular domain, focusing on the epoch in which it is relevant, in connection with the dynamics of cosmic acceleration and the nature of the dark energy. We wish to make here a summary of our work, outlining the issues which needs further investigation and the future developments. But before that, we also comment about the challenges that the CMB experimental science may encounter in trying to extract the lensing signal from the CMB anisotropy pattern, instrumentally but also in competition with other processes which may pollute the lensing signal itself. This is done in Sec. 7.1. In Sec. 7.2 we make the critical summary outlined above and the concluding remarks.

7.1 The challenge of measuring the CMB bispectrum from lensing

The weak lensing signal on the CMB bispectrum is a second order effect in cosmology, as it is caused by cosmological perturbations lensing primordial ones. Therefore, it is necessary pay a special attention to the different processes which may lead to a non-

Gaussian distortion of the CMB anisotropies, as well as to all the possible sources of errors. Indeed a deviation from Gaussianity can be produced by several effects, both of astrophysical and instrumental origin. Primordial non-Gaussianity (Gangui & Martin 2000; Komatsu & Spergel 2001), SZ effect (Cooray, Hu & Tegmark 2000), point sources, diffuse foreground emission, and all those effects that produce a non-Gaussian signal directly in the a_{lm} belong to the first class. All the possible sources of non-Gaussianity that are induced by some systematics such as sky cuts, and non-Gaussian features in the instrumental noise, beam asymmetries, etc., are examples of the second class.

In this section we first want to attempt a first comparison of the bispectrum signal from lensing with respect to the expectations relative to the other possible processes inducing a non-Gaussian distortion on the CMB. We consider here only the primordial non-Gaussianity from inflation, the coupling between weak lensing and SZ effect, and the bispectrum arising from extragalactic radio and infrared sources. We want to stress that we shall give only an order of magnitude of the estimation of those effect and a rough comparison with the bispectrum signal discussed in this work; most of those processes are very poorly known indeed, and presently under investigation, so that our analysis is completely preliminary and subject to changes. In this section we describe the bispectrum in terms of the reduced one $b_{l_1 l_2 l_3} = B^{m_1 m_2 m_3}_{l_1 l_2 l_3} / G^{m_1 m_2 m_3}_{l_1 l_2 l_3}$, where $G^{m_1 m_2 m_3}_{l_1 l_2 l_3}$ is the Gaunt integral (4.17). A primordial non-Gaussianity should be encapsulated in the gravitational potential perturbations Ψ, generated during inflation (see Bartolo *et al.* 2004 for reviews). Assuming the simplest case, the non-linear coupling parameter f_{NL} is simply a constant factor and is defined as

$$\Psi(\vec{x}) = \Psi_L(\vec{x}) + f_{NL} \Delta\Psi^2_L(\vec{x}) \ , \tag{7.1}$$

in real space, where $\Delta\Psi^2_L(\vec{x}) = \Psi^2_L(\vec{x}) - \left\langle \Psi^2_L(\vec{x}) \right\rangle$, in which L means linear, and the average is over the statistical ensemble. Applying the Fourier transform to Eq. (7.1) we get a decomposition in a linear and non-linear part $\Psi\left(\vec{k}\right) = \Psi_L\left(\vec{k}\right) + \Psi_{NL}\left(\vec{k}\right)$ leading to $a_{lm} = a^L_{lm} + a^{NL}_{lm}$ for the CMB anisotropy coefficients after expanding into spherical harmonics. The primordial equilateral bispectrum is approximately given by $b^P_l \sim 10^{-17} f_{NL} \times l^{-4}$ (Gangui & Martin 2000; Komatsu & Spergel 2001). Notice that its amplitude depends on the magnitude of the non-linear coupling f_{NL}. The present constraints from WMAP on the

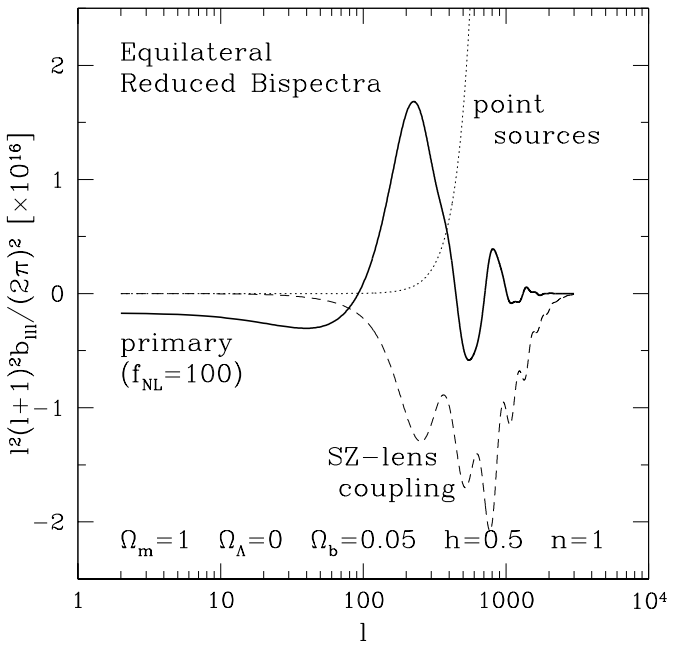

Figure 7.1: Equilateral reduced bispectrum for primordial non-Gaussianity, SZ-lens coupling and extragalactic points sources. From Komatsu & Spergel (2001).

non-linear coupling are $-58 < f_{NL} < 134$ at 95 % confidence (Komatsu *et al.* 2003).

A low redshift effect that can yield power in the CMB anisotropy bispectrum is the SZ effect, already described in Ch. 3; it occurs when CMB photons travel through a cluster of galaxies. Since approximately 10% of the total mass of rich clusters of galaxies is in the form of hot $\left(10^8\right)$ K ionized plasma, Compton scattering of CMB photons by electrons in this intra-cluster plasma can result in an optical depth as high as 0.02, inducing a distortion of the CMB spectrum at the mK level. There are multiple components of the SZ effect which result from distinct velocity components of the scattering electrons. The thermal component is due to the thermal (random) velocities of them. The kinematic component is due to the bulk velocity of the intra-cluster gas with respect to the CMB. In the Rayleigh-Jeans regime (at low frequencies) the change of the spectrum due to the Compton scattering can be seen as induced by a lower temperature of the radiation. In the Wien part of the spectrum (at high frequencies) one can interpret the change with a higher radiation temperature. Since the SZ effect couples with the weak lensing, just as the

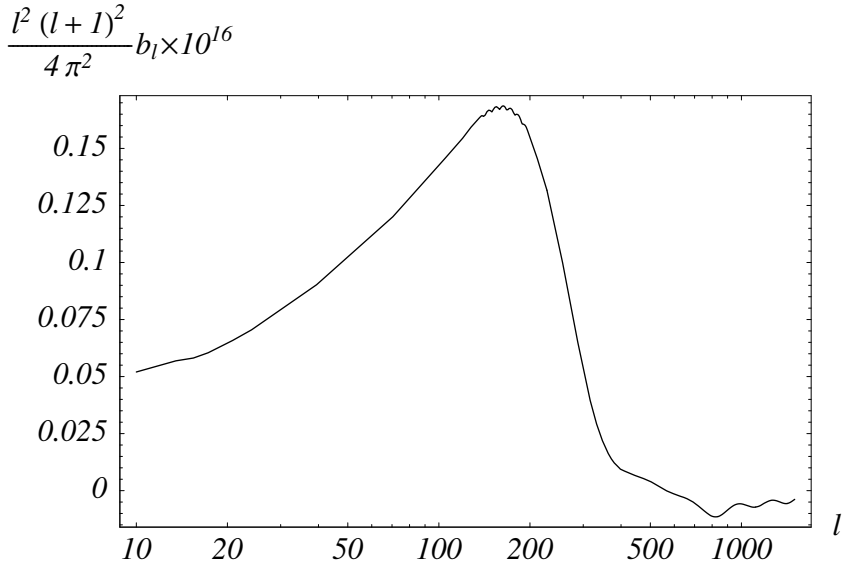

Figure 7.2: Equilateral reduced bispectrum for ISW-lensing coupling in units of 10^{-16}. The cosmology is set to our fiducial ΛCDM model used in Ch. 4; the model is different from that assumed in Fig. 7.1 (flat CDM) in that case the ISW effect is vanishing, reducing the SZ power with respect to what shown in Fig. 7.1.

ISW, its analysis is similar to that shown in Ch. 4 (for a detailed derivation see Goldberg & Spergel 1999). The magnitude of the reduced equilateral bispectrum for the SZ-lensing coupling is about $b_l^{SZ-lens} \sim 10^{-19} j_\nu \overline{T}_{\rho 0} p_g \times l^3$ (Komatsu & Spergel 2001) being j_ν the spectral function of the SZ effect, always of the order one, (equal to -2 in the Rayleigh regime), $\overline{T}_{\rho 0}$ the present density weighted mean temperature of the gas in units of 1 KeV and $p_g \sim 6$ the linear gas pressure bias (Refregier *et al.* 2000).

The CMB bispectrum from extragalactic sources is easy to estimate, as long as they are assumed to have a Poissonian distribution. Since the Poisson distribution has a white noise power spectrum, the reduced bispectrum is constant with an amplitude of roughly 10^{-28} (Komatsu & Spergel 2001).

Just to give an idea of these signals, in Fig. 7.1 we show a plot by Komatsu and Spergel (2001) representing the equilateral reduced bispectra from primordial non-Gaussianity, SZ-lensing coupling and point sources. At high multipoles the contribution of the point sources dominates over the others while at low multipoles (large angular scales) the primordial bispectrum is dominant. Comparing Figs. 7.1 and 7.2 we may notice that the

reduced equilateral bispectrum studied in our work has an amplitude generally lower than the other bispectra listed here, although with a markedly different shape. At low multipoles, up to 50, the point sources and the SZ produce signals close to zero whereas the primordial signal is negative. The ISW-lensing coupling contribution at those low multipoles is positive while at higher multipoles becomes negative, see Fig. 7.2. Comparing Fig. 7.1 and Fig. 7.2 we must also keep in mind that the cosmological models are different: in the former plot the model is a pure CDM model while in the latter is a ΛCDM model. On the other hand this very rough analysis can be useful to perform a first comparison of the different bispectrum sources. The analysis at low multipoles, where the point sources and the SZ effect contributions are vanishing, may be a tracer of the the primordial and ISW-lensing coupling bispectra; the amplitudes are roughly comparable for the f_{NL} value chosen, but we want to stress that the latter might be smaller as long as the early Universe processes keep close to Gaussianity. Finally the characteristic frequency dependence of the SZ might be exploited to attempt some subtraction in a multi-frequency observations.

In addition to the different processes outlined above, the foreground astrophysical signals may distort the CMB pattern and need to be controlled. A study of the foreground non-Gaussian signal in comparison to the CMB one from weak lensing will be certainly possible as the CMB observations are providing an excellent improvement on our knowledge of the foreground emission. An indications that the extra-Galactic foregrounds may not be dramatic as a contaminant of the lensing signal has been reported by Hirata *et al.* (2004); that is supported by the fact that some control of foregrounds may be achieved exploiting their different scaling in frequency with respect to the CMB in multi-band observations (Komatsu *et al.* 2003).

As we stressed above, the expectations outlined here are based on very preliminary knowledge of the listed physical processes, and should be taken as a first guess, and nothing more. The indication is that the ISW-lensing contribution may dominate on large angular scales, while on the degree and subdegree angular scales the other processes might yield relevant, being even dominating.

Finally, as we stressed in the beginning of this section, the signals of astrophysical nature are not the only sources of contamination to the weak lensing contribution. In fact,

it is also necessary to have tightly under control the systematics that can produce a spurious bispectrum signal. Among the most important, we can recall the incomplete sky coverage, beam asymmetry and non-Gaussian noise distribution. An analysis of these issues has never been attempted, and what we write here is even more preliminary than the forecast of the contamination from non-lensing processes outlined above. To make an example on how the systematics might impact on the CMB bispectrum observable, we report here the ensemble average of estimator of the bispectrum on the incomplete sky, the pseudo-bispectrum $B^{bias}_{l_1 l_2 l_3}$; it is expected to be (Bartolo *et al.* 2004; see also Peebles 1980 for further details on the observables on the incomplete sky)

$$\left\langle B^{bias}_{l_1 l_2 l_3} \right\rangle = B^{true}_{l_1 l_2 l_3} \frac{f_{sky}}{4\pi} \ , \tag{7.2}$$

where f_{sky} is the angular area covered by the observation. Thus the fraction of the observed sky is the bias factor for the bispectrum. The remaining effects are unknown, and should be evaluated in future analysis.

7.2 Summary, future perspectives and concluding remarks

The evidence for cosmic acceleration may be due to a new cosmological component acting as a gravitationally repulsive force on cosmological scales, the dark energy. As this component may be in the form of a fundamental energy density in vacuum, it is crucial to exploit the existing cosmological observables and build up new ones in order to probe the cosmological expansion during the onset of cosmic acceleration. In this thesis we studied the non-Gaussian signal induced on CMB anisotropies by weak lensing and structure formation and its dependence on the redshift behavior of the cosmological expansion rate determined by different dark energy models. Our approach is based on the harmonic expression of the three point CMB anisotropy statistics, described in terms of the CMB bispectrum.

In Ch. 4 we studied and analyzed general properties of the bispectrum from lensing. We have shown that the signal is injected at non-zero redshift, centered around the epoch of structure formation, overlapping with the onset of cosmic acceleration, cutting out the present. As a result, the CMB bispectrum is quite sensitive to the cosmic expansion rate

at that redshift, i.e. on the dark energy equation of state at that time, *independently* on its present value. The bispectrum signal depends on a triplet of angular multipoles, connecting the primordial signal with the lensing kernel by products involving different multipoles, and determines a reprojection of the acoustic peaks on scales markedly different from their well known location in the CMB power spectrum. The bispectrum coefficients, seen as a function of the three multipoles in arbitrary configuration, depict a complex structure of peaks and valleys in a three-dimensional space, bounded by geometrical constraints encoded in the Wigner 3J symbols. A recurring feature is the presence of a sign inversion in the bispectrum coefficients, on angular scales of a few hundreds, cutting almost in the middle the whole signal distribution; the latter feature represents the transition between linear and non-linear power domination in the lensing kernel, and appears visually as a "canyon" in the distribution of the absolute value of the bispectrum coefficients (Verde & Spergel 2002; Giovi, Baccigalupi & Perrotta 2003). A crucial part of the bispectrum evaluation is in the computation of the Wigner 3J symbols. A part of the work of this thesis was devoted to build a numerical code able to compute the 3J symbols at very high multipole; we have tested the code up to $l = 1000$, but we expect it to be reliable also at higher values.

The expected impact of the bispectrum data on the cosmological parameter estimation is shown in Ch. 6. This has been done analyzing the bispectrum signal to noise ratio and setting up a maximum likelihood analysis simulating a Planck-like experiment, varying the dark energy abundance Ω_V, its present and high redshift equation of state w_0 and w_∞ and keeping all the other cosmological parameters fixed to our fiducial model. Although rich, the phenomenology of the single bispectrum coefficient is unfortunately not observable in detail, as the effect represents a second order cosmological perturbation, and the single coefficient is largely dominated by cosmic variance, by a factor of about 100. The only way to exploit practically the bispectrum coefficients is to compress the information by summing over the different multipole triplets. By doing that, we verified that most of the signal is contained in the triplets with "scalene" configurations, merely because they represent the large majority of the whole number of coefficients. In agreement with previous analyses (Hu 2000), we shown how a cosmic variance limited experiment should be able to detect the bispectrum signal by summing at least up to a maximum multipole of a few hundreds.

The bispectrum data increases the overall sensitivity of the CMB on the dark energy high redshift dynamics, represented by w_∞, in comparison with the usual analysis made on the basis of the CMB total intensity power spectrum only; the latter is sensitive to the redshift average of the dark energy equation of state, through a projection effect: different combinations of w_0 and w_∞ leading to the same redshift average cannot be distinguished. Despite of the lower signal to noise ratio, the bispectrum likelihood contours present a substantial misalignment with respect to those of the power spectrum, being more sensitive to the changes in w_∞; consistently with the expectation that the lensing should probe directly the expansion rate at the epoch when the process is effective, independently on the present. The bispectrum actually breaks the projection degeneracy, allowing a measure of both w_0 and w_∞, at least in our three parameters likelihood analysis, where those and the dark energy abundance are the only varying parameters; the level of accuracy is at percent and ten percent, respectively. These results may increase the interest and efforts toward the detection of the weak lensing signal by the forthcoming CMB probes, as that may be relevant to gain insight into the dark energy dynamics at the onset of cosmic acceleration, when most models similar to a Cosmological Constant at present predict very different behaviors.

We close the thesis pointing out the issues which deserve further investigations, and some future directions. First, and obviously, our work is based on a few parameters only, directly related to the dark energy. A multi-parameter study would possibly reveal dangerous degeneracies in the bispectrum dependence on the underlying cosmology. Since the bispectrum power is injected at intermediate redshifts, we expect that this observable will be sensitive to those parameters that affect the cosmic history at that epoch. Second, besides the ISW-lensing correlation studied here, there can be other sources of bispectrum of astrophysical nature such as primordial non-Gaussianity, diffuse Galactic foregrounds, extra-Galactic point sources, Sunyaev-Zel'Dovich effect and so on, that should be carefully evaluated and taken into account for a realistic exploitation of the bispectrum data. In Sec. 7.1 we only presented a preliminary analysis and a deeper one is required. Third, in our work we used a semianalytical approach to model the bispectrum power from non-linear perturbations, a correct modeling of the non-linear matter power spectrum as a function of the wavenumber k and the redshift z in dark energy cosmologies has not been made

yet. That could be also done exploiting real data from future observations of Lyman-α forest (see e.g. Viel, Haehnelt & Springel 2004 and references therein) or with weak lensing measures (see e.g. Bacon *et al.* 2004 and references therein). Ultimately our results rely on two model independent features, namely the geometric modifications onto the cosmic expansion induced by different dark energy dynamics, and the fact that the lensing power is non-vanishing at the onset of acceleration and structure formation only, being zero earlier and at the present. Therefore we expect that our findings may be refined by addressing the issues mentioned above, but not substantially changed.

The curtain falls on the thesis hoping that, in some near future, the CMB bispectrum get eventually detected, and exploited to enlighten the dark mystery in which our Universe is enveloped.

Appendix A

Properties of Wigner's 3J symbols

In this appendix we shall collect and summarize the properties and the special values of the Wigner's 3J symbols (Wigner 1959; Messiah 1962; Abramowitz & Stegun 1972):[1]

$$\begin{pmatrix} l_1 & l_2 & l_3 \\ m_1 & m_2 & m_3 \end{pmatrix} . \tag{A.1}$$

Reality. The Wigner's 3J symbols are all real.

Selection rules. The Wigner's 3J symbols are null if the following conditions are not satisfied

- $m_1 + m_2 + m_3 = 0$,
- $|l_1 - l_2| \leq l_3 \leq l_1 + l_2$,

the second condition is the triangular inequalities and must be verified for all l_1, l_2 and l_3.

Symmetries. The Wigner's 3J symbols are:

- invariant in a circular permutation of the three columns;
- multiplied by $(-1)^{l_1+l_2+l_3}$ in a permutation of two columns;
- multiplied by $(-1)^{l_1+l_2+l_3}$ when we simultaneously change the signs of all m's.

[1] See also http://mathworld.wolfram.com/Wigner3j-Symbol.html

Orthogonality relations.

$$\sum_{m_1=-l_1}^{+l_1}\sum_{m_2=-l_2}^{+l_2}\begin{pmatrix} l_1 & l_2 & l_3 \\ m_1 & m_2 & m_3 \end{pmatrix}\begin{pmatrix} l_1 & l_2 & l_3' \\ m_1 & m_2 & m_3' \end{pmatrix} = \frac{\delta_{l_3 l_3'}\delta_{m_3 m_3'}}{2l_3+1}\ , \tag{A.2}$$

$$\sum_{l_3=|l_1-l_2|}^{l_1+l2}\sum_{m_3=-l_3}^{+l_3}(2l_3+1)\begin{pmatrix} l_1 & l_2 & l_3 \\ m_1 & m_2 & m_3 \end{pmatrix}\begin{pmatrix} l_1 & l_2 & l_3 \\ m_1' & m_2' & m_3 \end{pmatrix} = \delta_{m_1 m_1'}\delta_{m_2 m_2'} \tag{A.3}$$

δ_{ij} is the Kronecker's delta.

Composition relation for the spherical harmonics (Gaunt's integral).

$$G_{l_1 l_2 l_3}^{m_1 m_2 m_3} = \int d^2\hat{n} Y_{l_1 m_1}(\hat{n}) Y_{l_2 m_2}(\hat{n}) Y_{l_3 m_3}(\hat{n}) =$$

$$= \sqrt{\frac{(2l_1+1)(2l_2+1)(2l_3+1)}{4\pi}}\begin{pmatrix} l_1 & l_2 & l_3 \\ 0 & 0 & 0 \end{pmatrix}\begin{pmatrix} l_1 & l_2 & l_3 \\ m_1 & m_2 & m_3 \end{pmatrix}\ . \tag{A.4}$$

Special values. For some special values of l and m the Wigner's 3J possess a closed formula.

- l_3 is maximum and m_3 minimum:

$$\begin{pmatrix} l_1 & l_2 & l_1+l_2 \\ m_1 & m_2 & -l_1-l_2 \end{pmatrix} = \frac{(-1)^{2l_1}}{\sqrt{2l_1+2l_2+1}}\ . \tag{A.5}$$

- One l is zero:

$$\begin{pmatrix} l & l & 0 \\ m & -m & 0 \end{pmatrix} = \frac{(-1)^{l-m}}{\sqrt{2l+1}}\ . \tag{A.6}$$

- $m_1 = m_2 = m_3 = 0$ and $L = l_1 + l_2 + l_3 =$ even:

$$\begin{pmatrix} l_1 & l_2 & l_3 \\ 0 & 0 & 0 \end{pmatrix} = (-1)^{L/2}\frac{(L/2)!}{\sqrt{(L+1)!}}\prod_{i=1}^{3}\frac{\sqrt{(L-2l_i)!}}{(L/2-l_i)!}\ . \tag{A.7}$$

  If $L =$ odd the 3J symbols are zero. This closed formula has been widely used in this work; since the computation of factorial may be hard at high multipoles, we can use the Gosper approximation of the factorial:

$$n! \simeq \sqrt{\left(2n+\frac{1}{3}\right)\pi}\left(\frac{n}{e}\right)^n\ . \tag{A.8}$$

In this way we can rewrite Eq. (A.7) in a computational simpler form

$$\begin{pmatrix} l_1 & l_2 & l_3 \\ 0 & 0 & 0 \end{pmatrix} \simeq \left(-\frac{L}{L+1}\right)^{L/2} \frac{1}{(6L+7)^{1/4}} \left(\frac{3e}{\pi}\frac{3L+1}{L+1}\right)^{1/2} \prod_{i=1}^{3} \frac{(6L-12l_i+1)^{1/4}}{(3L-6l_i+1)^{1/2}} \,. \tag{A.9}$$

The Racah formula. An explicit relation between the triplets (l_1, l_2, l_3) and (m_1, m_2, m_3) and the Wigner's 3J symbols exists and is named the Racah formula; unfortunately it does not have any practical application because of its complexity. It is

$$\begin{aligned} \begin{pmatrix} l_1 & l_2 & l_3 \\ m_1 & m_2 & m_3 \end{pmatrix} &= (-1)^{l_1-l_2-m_3} \sqrt{\frac{(l_1+l_2-l_3)!(l_2+l_3-l_1)!(l_3+l_1-l_2)!}{(l_1+l_2+l_3+1)!}} \cdot \\ &\cdot \sqrt{(l_1+m_1)!(l_1-m_1)!(l_2+m_2)!(l_2-m_2)!(l_3+m_3)!(l_3-m_3)!} \cdot \\ &\cdot \sum_t \frac{(-1)^t}{t!(l_3-l_2+t+m_1)!(l_3-l_1+t-m_2)!(l_1+l_2-l_3-t)!(l_1-t-m_1)!(l_2-t+m_2)!} \,. \end{aligned} \tag{A.10}$$

$\sum_t$ extends over all integer values of t for which the factorial has a meaning, i.e. the arguments of the factorial are positive or zero.

Appendix B

The angle averaged bispectrum

Assuming statistical isotropy, which means that our sky is isotropic and has no preferred directions, we can average the bispectrum over m_i, representing the azimuthal orientation in the sky, with appropriate weights. In order to do that we must find a solution with rotational invariance of the three point correlation function in the sky,

$$\langle Rf(\hat{n}_1)Rf(\hat{n}_2)Rf(\hat{n}_3)\rangle = \langle f(\hat{n}_1)f(\hat{n}_2)f(\hat{n}_3)\rangle \ ; \tag{B.1}$$

where f represent a given function on the sphere, $f(\hat{n}) = \sum_{lm} a_{lm} Y_{lm}(\hat{n})$, while $R = R(\alpha, \beta, \gamma)$ is the rotation matrix and α, β and γ are the Euler angles. The rotation matrix with element $R^l_{m\,m'}$, describing a finite rotation from an initial state with (l, m) to a final state (l, m'), allow as to write the rotation of the spherical harmonics as

$$RY_{lm}(\hat{n}) = \sum_{m'=-l}^{l} R^l_{m\,m'} Y_{lm'}(\hat{n}) \ . \tag{B.2}$$

Putting together these the above two equations we obtain the statistical isotropy condition for the three point correlation function

$$\langle a_{l_1 m_1} a_{l_2 m_2} a_{l_3 m_3}\rangle = \sum_{m'_1 m'_2 m'_3} \left\langle a_{l_1 m'_1} a_{l_2 m'_2} a_{l_3 m'_3} \right\rangle R^{l_1}_{m_1 m'_1} R^{l_2}_{m_2 m'_2} R^{l_3}_{m_3 m'_3} \ . \tag{B.3}$$

Each pair of rotation matrices may be coupled into a single rotation via the addition of the angular momentum:

$$R^{l_1}_{m_1 m_1'} R^{l_2}_{m_2 m_2'} = \sum_{l_3} (2l_3+1) \sum_{m_3 m_3'} \left(R^{l_3}_{m_3 m_3'}\right)^* \begin{pmatrix} l_1 & l_2 & l_3 \\ m_1 & m_2 & m_3 \end{pmatrix} \begin{pmatrix} l_1 & l_2 & l_3 \\ m_1' & m_2' & m_3' \end{pmatrix} ; \tag{B.4}$$

applying this properties to Eq. (B.3) to reduce $R^{l_1}_{m_1 m_1'} R^{l_2}_{m_2 m_2'}$ to $R^{L}_{MM'}$ we obtain

$$\begin{aligned}
\langle a_{l_1 m_1} a_{l_2 m_2} a_{l_3 m_3} \rangle &= \sum_{m_1' m_2' m_3'} \left\langle a_{l_1 m_1'} a_{l_2 m_2'} a_{l_3 m_3'} \right\rangle R^{l_1}_{m_1 m_1'} R^{l_2}_{m_2 m_2'} R^{l_3}_{m_3 m_3'} = \\
&= \langle B_{l_1 l_2 l_3} \rangle \sum_{m_1' m_2' m_3'} \begin{pmatrix} l_1 & l_2 & l_3 \\ m_1' & m_2' & m_3' \end{pmatrix} \times \\
&\times \sum_{LMM'} (2L+1) \left(R^{L}_{MM'}\right)^* R^{l_3}_{m_3 m_3'} \begin{pmatrix} l_1 & l_2 & L \\ m_1' & m_2' & M \end{pmatrix} \begin{pmatrix} l_1 & l_2 & L \\ m_1 & m_2 & M \end{pmatrix} = \\
&= \langle B_{l_1 l_2 l_3} \rangle \sum_{m_3'} \sum_{LMM'} \begin{pmatrix} l_1 & l_2 & L \\ m_1 & m_2 & M \end{pmatrix} \left(R^{L}_{MM'}\right)^* R^{l_3}_{m_3 m_3'} \delta^{L}_{l_3} \delta^{M'}_{m_3'} = \\
&= \langle B_{l_1 l_2 l_3} \rangle \begin{pmatrix} l_1 & l_2 & l_3 \\ m_1 & m_2 & m_3 \end{pmatrix} ,
\end{aligned} \tag{B.5}$$

where we used the orthonormality relations both for the Wigner 3J symbols (see App. A) and for the rotation matrices. Comparing the last row of previous equation with Eq. (B.3), we see that the weights we are looking for are just the Wigner 3J symbols.

Bibliography

[1] Abramowitz M. & Stegun I.A., *"Handbook of mathematical functions with formulas, graphs, and mathematical tables"*, Dover Ed., New York (1972).

[2] Afshordi N., Loh Y.S. & Strauss M.A., *"Cross-correlation of the cosmic microwave background with the 2MASS galaxy survey: Signatures of dark energy, hot gas, and point sources"*, Phys. Rev. D **69**, 083524 (2004).

[3] Aldering G., Knop R. & Nugent P., *"The rise times of high- and low-redshift Type IA supernovæ are Consistent"*, Astronom. J. **119**, 2110 (2000).

[4] Aldering G. *et al.* , *"Overview of the SuperNova/Acceleration Probe (SNAP)"*, SPIE **4835**, 146, astro-ph/0209550 preprint (2002).

[5] Allen S.W., Schmidt R.W., Fabian A.C. & Ebeling H., *"Cosmological constraints from the local X-ray luminosity function of the most X-ray luminous galaxy cluster"*, Mon. Not. R. Astron. Soc. **342**, 287 (2003).

[6] Amendola L., *"Coupled quintessence"*, Phys. Rev. D **62**, 043511 (2000).

[7] Amendola L., *"Linear and nonlinear perturbations in dark energy models"*, Phys. Rev. D **69**, 103524 (2004).

[8] Alpher R.A. & Herman R.C., *"Theory of the origin and relative abundance distribution of the elements"*, Rev. Mod. Phys. **22**, 153 (1950).

[9] Baccigalupi C., *"Cosmic microwave background: polarization and temperature anisotropies from symmetric structures"*, Phys. Rev. D **59**, 123004 (1999).

[10] Baccigalupi C., Balbi A., Matarrese S., Perrotta F. & Vittorio N., *"Constraints on flat cosmologies with tracking quintessence from cosmic microwave background observations"*, Phys. Rev. D **65**, 063520 (2002).

[11] Bacon D.J., Refregier A. & Ellis R., *"Detection of weak gravitational lensing by large-scale structure"*, Mon. Not. R. Astron. Soc. **318**, 625 (2000).

[12] Bacon D.J. *et al.* , *"Evolution of the dark matter distribution with 3-D weak lensing"*, submitted to Mon. Not. R. Astron. Soc., astro-ph/0403384 preprint (2004).

[13] Balbi A. *et al.* , *"Probing dark energy with the CMB: projected constraints from WMAP and Planck"*, Astrophys. J. Lett. **588**, L5 (2003).

[14] Bartelmann M. & Schneider P., *"Weak gravitational lensing"*, Phys. Rep. **340**, 291 (2001).

[15] Bartelmann M., Perrotta F. & Baccigalupi C., *"Halo concentrations and weak-lensing number counts in dark energy cosmologies"*, Astron. Astrophys. **396**, 21 (2002).

[16] Bartelmann M., Meneghetti M., Perrotta F., Baccigalupi C. & Moscardini L., *"Arc statistics in cosmological models with dark energy"*, Astron. Astrophys. **409**, 499 (2003).

[17] Bartolo N., Komatsu E., Matarrese S. & Riotto A., *"Non-Gaussianity from inflation: theory and observations"*, Phys. Rep. **402**, 103 (2004).

[18] Bennett C.L. *et al.* , *"Cosmic temperature fluctuations from two years of COBE differential microwave radiometers observations"*, Astrophys. J. **436**, 423 (1994).

[19] Bennett C.L. *et al.* , *"First-year Wilkinson Microwave Anisotropy Probe (WMAP) observations: preliminary maps and basic results"*, Astrophys. J. Suppl. Series **148**, 1 (2003).

[20] Bernardeau F., *"Dark matter, dark energy, gravitational lensing and the formation of structure in the Universe"*, Rep. Prog. Phys. **66**, 691 (2003).

[21] Binetruy P., *"Models of dynamical supersymmetry breaking and quintessence"*, Phys. Rev. D **60**, 063502 (1999).

[22] Birkinshaw M., *"The Sunyaev-Zel'dovich effect"*, Phys. Rep. **310**, 97 (1999).

[23] Brax P. & Martin J., *"Quintessence and supergravity"*, Phys. Lett. B **468**, 40 (1999).

[24] Brax P. & Martin J., *"Robustness of quintessence"*, Phys. Rev. D **61**, 103502 (2000).

[25] Brax P., Martin J. & Riazuelo A., *"Exhaustive study of cosmic microwave background anisotropies in quintessential scenarios"*, Phys. Rev. D **62**, 103505 (2000).

[26] Burd A.B. & Barrow D., *"Inflationary models with exponential potentials"*, Nucl. Phys. B **302**, 668 (1988).

[27] Caldwell R.R., Dave R. & Steinhardt P. *"Cosmological imprint of an energy component with general equation of state"*, Phys. Rev. Lett. **80**, 1582 (1998).

[28] Chaboyer B., Demarque P., Kernan P.J. & Krauss L.M., *"The age of globular clusters in light of Hipparcos: resolving the age problem?"*, Astrophys. J. **494**, 96 (1998).

[29] Chae K.H. *et al.* , *"Constraints on cosmological parameters from the analysis of the Cosmic Lens All Sky Survey radio-selected gravitational lens statistics"*, Phys. Rev. Lett. **89**, 151301, (2002).

[30] Chevallier M. & Polarski D., *"Accelerating universes with scaling dark matter"*, Int. J. Mod. Phys. D **10**, 213 (2001).

[31] Cole S. *et al.* , *"The 2dF Galaxy Redshift Survey: power-spectrum analysis of the final dataset and cosmological implications"*, Mon. Not. R. Astron. Soc., in press, astro-ph/0501174 preprint (2005).

[32] Cooray A., Hu W. & Tegmark M., *"Large-scale Sunyaev-Zeldovich effect: measuring statistical properties with multifrequency maps"*, Astrophys. J. **540**, 1 (2000).

[33] Copeland E.J., Liddle A.R. & Wands D., *"Exponential potentials and cosmological scaling solutions"*, Phys. Rev. D **57**, 4686 (1998).

[34] Copeland E.J., Nunes N.J. & Rosati F., *"Quintessence model in supergravity"*, Phys. Rev. D **62**, 123503 (2000).

[35] Corasaniti P.S. & Copeland E.J., *"Model independent approach to the dark energy equation of state"*, Phys. Rev. D **67**, 063521 (2003).

[36] Croft R.A.C. *et al.* , *"Toward a precise measurement of matter clustering: Ly-α forest data at redshifts 2-4"*, Astrophys. J. **581**, 20 (2002).

[37] de Bernardis P. *et al.* , *"A flat universe from high-resolution maps of the cosmic microwave background radiation"*, Nature **404**, 955 (2000).

[38] Dicke R.H., Peebles P.J.E., Roll P.G. & Wilkinson D.T. *"Cosmic Black-Body Radiation"*, Astrophys. J. **142**, 414 (1965).

[39] Dickinson C. *et al.* , *"High-sensitivity measurements of the cosmic microwave background power spectrum with the extended Very Small Array"*, Mon. Not. R. Astron. Soc. **353**, 732 (2004).

[40] Dodelson S. *et al.* , *"The 3D power spectrum from angular clustering of galaxies in early SDSS data"*, Astrophys. J. **572**, 140 (2002).

[41] Dodelson S., *"Modern cosmology"*, Calif. Academic Press, San Diego, (2003).

[42] Doroshkevich A.G., Zel'Dovich Ya.B. & Syunyaev R.A., *"Fluctuations of the microwave background radiation in the adiabatic and entropic theories of galaxy formation"*, Sov. Astron. **22**, 523 (1978).

[43] Efstathiou G. *et al.* , *"Evidence for a non-zero Λ and a low matter density from a combined analysis of the 2dF Galaxy Redshift Survey and cosmic microwave background anisotropies"*, Mon. Not. R. Astron. Soc. **330**, L29 (2002).

[44] Efstathiou G., *"Principal-component analysis of the cosmic microwave background anisotropies: revealing the tensor degeneracy"*, Mon. Not. R. Astron. Soc. **332**, 193 (2002).

[45] Esposito-Farese G. & Polarski D., *"Scalar-tensor gravity in an accelerating universe"*, Phys. Rev. D **63**, 063504 (2001).

[46] Ferreira P.G. & Joyce M., *"Structure formation with a self-tuning scalar field"*, Phys. Rev. Lett. **79**, 4740 (1997).

[47] Freedman W.L. *et al.* , *"Final results from the Hubble Space Telescope Key Project to measure the Hubble constant"*, Astrophys. J. **553**, 47 (2001).

[48] Gamow G., *"On Relativistic Cosmogony"*, Rev. Mod. Phys. **21**, 367 (1949).

[49] Gangui A. & Martin J., *"Cosmic microwave background bispectrum and slow-roll inflation"*, Mon. Not. R. Astron. Soc. **313**, 323 (2000).

[50] Gangui A. & Martin J., *"Best unbiased estimators for the three-point correlators of the cosmic microwave background radiation"*, Phys. Rev. D **62**, 103004 (2000a).

[51] Giovi F., Baccigalupi C. & Perrotta F., *"Constraining the dark energy dynamics with the cosmic microwave background bispectrum"*, Phys. Rev. D **68**, 123002 (2003)

[52] Giovi F., Baccigalupi C. & Perrotta F., *"Cosmic microwave background constraints on dark energy dynamics: analysis beyond the power spectrum"*, Phys. Rev. D **71**, 103009 (2005).

[53] Gnedin N.Y. & Hamilton A.J.S., *"Matter power spectrum from the Lyman α forest: myth or reality?"*, Mon. Not. R. Astron. Soc. **334**, 107 (2002).

[54] Goldberg D.M. & Spergel D.N., *"Microwave background bispectrum. II. A probe of the low redshift Universe"*, Phys. Rev. D **59**, 103002 (1999).

[55] Goldstein *et al.* , *"Estimates of cosmological parameters using the CMB angular power spectrum of ACBAR"*, Astrophys. J. **599**, 773 (2003).

[56] Green M.B., Schwarz J.H. & Witten E., *"Superstring theory"*, Cambridge University Press, Cambridge (1987).

[57] Halliwell J.J., *"Scalar fields in cosmology with an exponential potential"*, Phys. Lett. B **185**, 341 (1987).

[58] Heavens A.F., *"Estimating non-Gaussianity in the microwave background"*, Mon. Not. R. Astron. Soc. **299**, 805 (1998).

[59] Hillebrandt W. & Niemeyer J.C., *"Type IA supernova explosion models"*, Ann. Rev. Astron. Astrophys. **38**, 191 (2000).

[60] Hinshaw G. *et al.* , *"First-year Wilkinson Microwave Anisotropy Probe (WMAP) observations: the angular power spectrum"* Astrophys. J. Suppl. **148**, 135 (2003).

[61] Hirata C.M., Padmanabhan N., Seljak U., Schlegel D. & Brinkmann J., *"Cross-correlation of CMB with large-scale structure: weak gravitational lensing"*, Phys. Rev. D **70**, 103501 (2004).

[62] Hoeflich P., Wheeler J.C. & Thielemann F.K., *"Type IA supernovæ: influence of the initial composition on the nucleosynthesis, light curves, and spectra and consequences for the determination of* Ω_M *and* Λ*"*, Astrophys. J. **495**, 617 (1998).

[63] Hu W. & Sugiyama N., *"Toward understanding CMB anisotropies and their implications"*, Phys. Rev. D **51**, 2599 (1995).

[64] Hu W. & Sugiyama N., *"Anisotropies in the cosmic microwave background: an analytic approach"*, Astrophys. J. **444**,489 (1995a).

[65] Hu W. & White M., *"CMB anisotropies: total angular momentum method"*, Phys. Rev. D **56**, 596 (1997).

[66] Hu W. & White M., *"The damping tail of cosmic microwave background anisotropies"*, Astrophys. J. **479**, 568 (1997a).

[67] Hu W., *"Weak Lensing of the CMB: a harmonic approach"*, Phys. Rev. D **62**, 043007 (2000).

[68] Hu W., *"Dark energy and matter evolution from lensing tomography"*, Phys. Rev. D **66**, 083515 (2002).

[69] Huterer D., *"Weak lensing and dark energy"*, Phys. Rev. D **65**, 063001 (2002).

[70] Hwang J.C., *"Perturbations of the Robertson-Walker space - multicomponent sources and generalized gravity"*, Astrophys. J. **375**, 443 (1991).

[71] Jones W.C. *et al.* , *"A measurement of the angular power spectrum of the CMB temperature anisotropy from the 2003 flight of BOOMERanG"*, submitted to Astrophys. J., astro-ph/0507494 preprint (2005).

[72] Kaiser N. & Stebbins A., *"Microwave anisotropy due to cosmic strings"*, Nature **310**, 391 (1984).

[73] Kaiser N., *"Weak gravitational lensing of distant galaxies"*, Astrophys. J. **388**, 272 (1992).

[74] Kaiser N., *"Weak lensing and cosmology"*, Astrophys. J. **498**, 26 (1998).

[75] Knop R.A. *et al.* , *"New Constraints on Ω_M, Ω_Λ, and w from an Independent Set of Eleven High-Redshift Supernovae Observed with HST"*, Astrophys. J. **598**, 102 (2003).

[76] Kodama H. & Sasaki M., *"Cosmological perturbation theory"*, Prog. Theor. Phys. **78**, 1 (1984).

[77] Kogut A. *et al.* , *"First-year Wilkinson Microwave Anisotropy Probe (WMAP) observations: temperature-polarization correlation"*, Astrophys. J. Suppl. Ser. **148**, 161 (2003).

[78] Komatsu E. & Spergel D.N., *"Acoustic signatures in the primary microwave background bispectrum"*, Phys. Rev. D **63**, 063002 (2001).

[79] Komatsu E.*et al.* , *"First-year Wilkinson Microwave Anisotropy Probe (WMAP) observations: tests of gaussianity"*, Astrophys. J. Suppl. Ser. **148**, 119 (2003).

[80] Kovac J.M., *et al.* , *"Detection of polarization in the cosmic microwave background using DASI"*, Nature **420**, 772 (2002).

[81] Kuo C.L. *et al.* , *"High-Resolution observations of the Cosmic Microwave Background power spectrum with ACBAR"*, Astrophys. J. **600**, 32 (2004).

[82] Leibundgut B., *"Cosmological implications from observations of Type Ia supernovæ"*, Ann. Rev. Astron. Astrophys. **39**, 67 (2001).

[83] Liddle A.R. & Scherrer R.J., *"Classification of scalar field potential with cosmological scaling solutions"*, Phys. Rev. D **59**, 023509 (1998).

[84] Liddle, A.R. & Lyth D.H., *"Cosmological inflation and large-scale structure"*, Cambridge University Press, Cambridge (2000).

[85] Linde A.V., *"Chaotic inflation"*, Phys. Lett. B **129**, 177 (1983).

[86] Linder E.V., *"Exploring the expansion history of the Universe"* Phys. Rev. Lett. **90**, 091301 (2003).

[87] Lucchin F. & Matarrese S., *"Power-law inflation"*, Phys. Rev. D **32**, 1216 (1985).

[88] Luo X., *"The angular bispectrum of the cosmic microwave background"*, Astrophys. J. **427**, L71 (1994).

[89] Ma C.P. & Bertschinger E., *"Cosmological perturbation theory in the synchronous and conformal newtonian gauges"*, Astrophys. J. **455**, 7 (1995).

[90] Ma C.P., *"Analytical approximation to the nonlinear power spectrum of gravitational clustering"*, Astrophys. J. Lett. **508**, L5, (1998).

[91] Ma C.P., Caldwell R.R., Bode P. & Wang L., *"The Mass Power Spectrum in Quintessence Cosmological Models"*, Astrophys. J. Lett **521**, L1 (1999).

[92] Mac Tavish C.J. *et al.* , *"Cosmological parameters from the 2003 flight of BOOMERanG"*, submitted to Astrophys. J., astro-ph/0507503 preprint (2005).

[93] Maoli R. *et al.* , *"Cosmic shear analysis in 50 uncorrelated VLT fields. Implications for Ω_0, σ_8"*, Astron. Astrophys. **368**, 766 (2001).

[94] Matarrese S., Baccigalupi C. & Perrotta F., *"Approaching Λ without fine-tuning"*, Phys. Rev. D **70**, 061301(R), (2004).

[95] Martinez-Gonzalez E., Sanz J.L. & Silk J., *"Anisotropies in the microwave sky due to nonlinear structures"*, Astrophys. J. **355**, L5 (1990).

[96] Messiah A., *"Quantum Mechanics vol. 2"*, North-Holland Ed., Amsterdam (1962).

[97] Mukhanov V., Feldmann H. & Brandenberger R., *"Theory of cosmological perturbations"*, Phys. Rep. **215**, 203 (1992).

[98] Padmanabhan T., *" Cosmological Constant - the weight of the vacuum"*, Phys. Rep. **380**, 235 (2003).

[99] Pearson T.J. *et al.* , *"The anisotropy of the microwave background to $l = 3500$: mosaic observations with the cosmic background imager"*, Astrophys. J. **591**, 556 (2003).

[100] Peebles P.J.E. & Yu J.T., *"Primeval adiabatic perturbation in an expanding universe"*, Astrophys. J. **162**, 815 (1970).

[101] Peebles P.J.E., *"The large-scale structure of the Universe"*, Princeton University Press, Princeton, (1980).

[102] Peebles P.J.E. & Ratra B., *"The Cosmological Constant and dark energy"*, Rev. Mod. Phys. **75**, 599 (2003).

[103] Peiris *et al.* , *"First-year Wilkinson Microwave Anisotropy Probe (WMAP) observations: implications for inflation"*, Astrophys. J. Suppl. Series **148**, 213 (2003).

[104] Penzias A.A. & Wilson R.W., *"A measurement of excess antenna temperature at 4080 Mc/s."*, Astrophys. J. **142**, 419 (1965).

[105] Percival W.J. *et al.* , *"The 2DF Galaxy Redshift Survey: the power spectrum and the matter content of the Universe"*, Mon. Not. R. Astron. Soc. **327**, 1297 (2001).

[106] Percival W.J. *et al.* , *"Parameter constraints for flat cosmologies from cosmic microwave background and 2dFGRS power spectra"*, Mon. Not. R. Astron. Soc. **337**, 1068 (2002).

[107] Perlmutter S. *et al.* , *"Measurements of* Ω *and* Λ *from 42 High-Redshift Supernovæ"* Astrophys. J. **517**, 565 (1999).

[108] Perlmutter S., *"Dark energy: recent observations and future prospects"*, Nucl. Phys. B Proc. Suppl. **124**, 13 (2003).

[109] Perrotta F. & Baccigalupi C., *"Early time perturbations behavior in scalar field cosmologies"*, Phys. Rev. D **59**, 123508 (1999).

[110] Perrotta F., Baccigalupi C. & Matarrese S., *"Extended quintessence"*, Phys. Rev. D **61**, 023507 (2000).

[111] Perrotta F., Baccigalupi C. & Matarrese S., *"Tracking extended quintessence"*, Phys. Rev. D **62**, 123510 (2000a).

[112] Perrotta F. & Baccigalupi C., *"On the dark energy clustering properties"*, Phys. Rev. D **65**, 123505 (2002).

[113] Ratra B. & Peebles P.J.E., *"Cosmological consequences of a rolling homogeneous scalar field"*, Phys. Rev. D **37**, 3406 (1988).

[114] Readhead A.C.S. *et al.* , *"Extended mosaic observations with the Cosmic Background Imager"*, Astrophys. J. **609**, 498 (2004).

[115] Rees M. & Sciama D.M., *"Larger scale density inhomogeneities in the Universe"*, Nature **217**, 511 (1968).

[116] Refregier A. *et al.* , *"Power spectrum of the Sunyaev-Zel'dovich effect"*, Phys. Rev. D **61**, 123001 (2000).

[117] Refregier A. *et al.* , *"Weak Lensing from space III: cosmological parameters"*, Astronom. J. **127**, 3102 (2004).

[118] Riess A.G. *et al.* , *"Observational evidence from supernovæ for an accelerating universe and a Cosmological Constant"*, Astronom. J. **116**, 1009 (1998).

[119] Riess A.G. *et al.* , *"Tests of the accelerating Universe with near-infrared observations of a high-redshift Type IA supernova"*, Astrophys. J. **536**, 62 (2000).

[120] Riess A.G. *et al.* , *"Type Ia Supernova discoveries at $z > 1$ from the Hubble Space Telescope: evidence for past deceleration and constraints on dark energy evolution"*, Astrophys. J. **607**, 665 (2004).

[121] Sachs R.K. & Wolfe A.M., *"Perturbations of a cosmological model and angular variations of the microwave background"*, Astrophys. J. **147**, 73 (1967).

[122] Sakurai J.J., *"Modern quantum mechanics"*, Addison-Wesley Ed., Reading (1994).

[123] Sanchez A.G. *et al.* , *"Cosmological parameters from CMB measurements and the final 2dFGRS power spectrum"*, submitted to Mon. Not. R. Astron. Soc., astro-ph/0507583 preprint (2005).

[124] Schneider P., Ehlers J. & Falco E.E., *"Gravitational lenses"*, Springer-Verlag Ed., New York, (1992).

[125] Schulten K. & Gordon R.G., *"Exact recursive evaluation of 3j- and 6j- coefficients for quantum-mechanical coupling of angular momenta"*, J. Math. Phys. **16**, 196 (1975).

[126] Seljak U., *"Large-scale structure effects on the gravitational lens image positions and time delay"*, Astrophys. J. **436**, 509 (1994).

[127] Seljak U., *"Rees-Sciama effect in a cold dark matter universe"*, Astrophys. J. **460**, 549 (1996).

[128] Seljak U., *"Gravitational lensing effect on cosmic microwave background anisotropies: a power spectrum approach"*, Astrophys. J. **463**, 1 (1996a).

[129] Seljak U. & Zaldarriaga M., *"A line-of-sight integration approach to cosmic microwave background anisotropies"*, Astrophys. J. **469**, 437 (1996).

[130] Sievers J.L. *et al.* , *"Cosmological parameters from cosmic microwave background imager observations and comparisons with BOOMERanG, DASI and MAXIMA"*, Astrophys. J. **591**, 599 (2003).

[131] Silberman L., Dekel A., Eldar A. & Zehavi I., *"Cosmological density and power spectrum from peculiar velocities: non linear corrections and PCA"*, Astrophys. J. **557**, 102 (2001).

[132] Silk J., *"Cosmic black-body radiation and galaxy formation"*, Astrophys. J. **151**, 459 (1968).

[133] Spergel D.N. & Goldberg D.M., *"Microwave background bispectrum. I. Basic formalism"*, Phys. Rev. D **59**, 103001 (1999).

[134] Spergel D.N. *et al.* , *"First-year Wilkinson Microwave Anisotropy Probe (WMAP) observations: determination of cosmological parameters"*, Astrophys. J. Suppl. Series **148**, 175 (2003).

[135] Steinhardt P.J., Wang L. & Zlatev I., *"Cosmological tracking solutions"*, Phys. Rev. D **59**, 123504 (1999).

[136] Stompor R. *et al.* , *"Cosmological implications of the MAXIMA-I high resolution cosmic microwave background anisotropy measurement"*, Astrophys. J. **561**, L7 (2001).

[137] Sugiyama N., *"Cosmic background anisotropies in cold dark matter cosmology"*, Astrophys. J. Suppl. Ser. **100**, 281 (1995).

[138] Sunyaev R.A. & Zel'dovich Ya.B., *"The observations of relic radiation as a test of the nature of X-Ray radiation from the clusters of galaxies"*, Comm. Astrophys. Space Phys. **4**, 73 (1972).

[139] Takada M. & Jain B., *"Cosmological parameters from lensing power spectrum and bispectrum tomography"*, Mon. Not. R. Astron. Soc. **348**, 897 (2004).

[140] Tegmark M. *et al.* , *"Cosmological parameters from SDSS and WMAP"*, Phys. Rev. D **69**, 103501, (2004).

[141] Tegmark M. *et al.* , *"The three-dimensional power spectrum of galaxies from the Sloan Digital Sky Survey"*, Astrophys. J. **606**, 702 (2004a).

[142] Van Waerbeke L. *et al.* , *"Detection of correlated galaxy ellipticities from CFHT data: first evidence for gravitational lensing by large-scale structures"*, Astron. Astrophys. **358**, 30 (2000).

[143] Van Waerbeke L. *et al.* , *"Cosmic shear statistics and cosmology"*, Astron. Astrophys. **374**, 757 (2001).

[144] Verde L. & Spergel D.N., *"Dark energy and cosmic microwave background bispectrum"*, Phys. Rev. D **65**, 043007 (2002).

[145] Viel M., Haehnelt G. & Springel V., *"Inferring the dark matter power spectrum from the Lyman α forest in high-resolution QSO absorption spectra"*, Mont. Not. R. Astron. Soc. **354**, 684 (2004).

[146] Weinberg S., *"Gravitation and cosmology"*, Wiley Ed., New York (1972).

[147] Weinberg N.N. & Kamionkowski M., *"Constraining dark energy from the abundance of weak gravitational lenses"*, Mont. Not. R. Astron. Soc. **341**, 251 (2003).

[148] Wess J. & Bagger J., *"Supersymmetry and supergravity"*, Princeton University Press Ed., Princeton (1992).

[149] Wetterich C., *"Cosmologies with variable Newton's constant"*, Nucl. Phys. B **302**, 645 (1988).

[150] Wetterich C., *"Cosmology and the fate of dilatation symmetry"*, Nucl. Phys. B **302**, 668 (1988a).

[151] Wigner E.P., *"Group theory and its application to the quantum mechanics of atomic spectra, expanded and improved ed."*, Academic Press, New York (1959).

[152] Wilson G., Kaiser N. & Luppino G.A., *"Mass and light in the Universe"*, Astrophys. J. **556**, 601 (2001).

[153] Wittmann D.M., Tyson J.A., Kirkman D., Dell'Antonio I. & Bernstein G., *"Detection of weak gravitational lensing distortions of distant galaxies by cosmic dark matter at large scales"*, Nature **405**, 143 (2000).

[154] White M. & Hu W., *"The Sachs-Wolfe effect"*, Astron. & Astrophys. **321**, 8 (1997).

[155] Zlatev I., Wang L. & Steinhardt P.J., *"Quintessence, cosmic coincidence, and the Cosmological Constant"*, Phys. Rev. Lett. **82**, 896 (1999).